CONFINEMENT AND TRACKING OF BROWNIAN PARTICLES IN A BESSEL BEAM STANDING WAVE

BY

CHAD B. MCKELL

A Thesis Submitted to the Graduate Faculty of

WAKE FOREST UNIVERSITY GRADUATE SCHOOL OF ARTS AND SCIENCES

in Partial Fulfillment of the Requirements

for the Degree of

MASTER OF SCIENCE

Physics

December 2015

Winston-Salem, North Carolina

Approved By:

Keith D. Bonin, Ph.D., Advisor

George Holzwarth, Ph.D., Chair

Richard T. Williams, Ph.D.

To my parents, Allen and Wendy McKell

Acknowledgments

I would like to express my appreciation to Keith Bonin for the countless hours of helpful discussion and technical guidance that he provided during the course of our research. He produced the initial idea for the project, supervised the experiments, and directed the final analysis. I would also like to thank Bob Morris for his assistance in the design and manufacture of essential experimental components; George Holzwarth and Richard Williams for reviewing this thesis report and offering their professional critique; and Research Corporation and Wake Forest University for funding our research. Finally, I want to express my gratitude to my family and friends for their patience and encouragement, particularly my wife, Katherine.

Table of Contents

List of Figures

List of Tables

Abstract

Optical trapping is a useful tool for manipulating microscopic particles and probing the physical interactions of matter. However, previous optical trapping techniques introduced complications for analyzing Brownian particle diffusion in viscous media because they either restricted the particles' motion or trapped the particles too close to a surface. To our knowledge, this thesis presents the first realization of two-dimensional, transverse tracking of Brownian microparticles in multiple, surface-isolated traps. To accomplish this, we used an axicon-generated, zeroth-order Bessel beam standing wave whose parameters were adjusted to allow tight axial confinement and loose transverse confinement of microscopic-sized particles in the central maximum of the Bessel beam. We chose a Bessel beam because its unique non-diffracting and self-healing properties provided distinct advantanges over a Gaussian beam. In particular, a Bessel beam standing wave was shown to produce optical potential wells that are more abundant, uniform, and stable than those of a Gaussian standing wave.

For our diffusion analysis, we collected tracking data of individually trapped fluorescent microspheres submerged in water and then quantified their motion using mean-square displacement algorithms. In our experiments, we tested spheres with diameters 100, 200, and 300 nm. Since the particles moved inside the confined area of an optical potential well, we used the generic equation for confined diffusion to characterize the motional dynamics of the particles. To calculate the diffusion coefficients of each particle, we fit the mean-square displacement points to the expression for confined diffusion. As expected, our results using the expression for confined diffusion to model the particles' motion proved to be more accurate than the values obtained using Einstein's unconfined diffusion equation. In the future, we propose to analyze the data by adopting a more rigorous Bayesian statistical technique so as to better account for the optical potential of the Bessel beam standing wave. Our research has potential applications in microrheology and microfluidics research; specifically, our Bessel beam standing wave trap may be further utilized to approximate the viscosity of semi-dilute polymer solutions and to measure fluid drag forces near surfaces.

Chapter 1: Introduction

1.1 Background

Light is a remarkable curiosity. It always moves with constant speed in vacuum and consists of mysterious elementary particles called photons. Photons of sunlight originate from a cluster of powerful fusion reactions deep within the Sun's plasma interior.[1] Once they escape the surface of the Sun, the photons travel at a spectacular rate, arriving at Earth's orbit in a stunning 8.3 minutes. For those photons that enter our atmosphere, some will be absorbed by air molecules and scattered throughout the sky, painting the heavens in beautiful shades of blue. Others will pass through, providing energy and illumination to the ecosystems below. Still others, if the conditions are right, will reflect off tiny water droplets in the moist air, producing brilliant muliticolored bands of electromagnetic radiation.

For centuries, the interaction of light with matter has both powered our planet and intrigued our inquisitive minds. In 1619, Johannes Kepler hypothesized that pressure from sunlight was responsible for the tails of dust and gas left behind in the wake of comets [1]. James Maxwell later deduced in 1871 that all electromagnetic radiation exerts a pressure $P_{\text{rad}} = \frac{\langle I \rangle}{c}$ on surfaces it interacts with, where $\langle I \rangle$ is the time-averaged irradiance and c is the speed of light [2]. Using a torsion balance radiometer, Nichols and Hull succeeded in measuring radiation pressure experimentally, verifying Maxwell's prediction to within one percent [3, 4]. However, before the invention of the laser in 1960 [5–7], light radiation pressure only played a significant role in outerspace, where light intensities are substantial.

With the development of high irradiance lasers, radiation pressure became in-

[1] The nucluear fusion reactions in the Sun's core produce high energy gamma rays that are later converted to lower energy photons before they reach the surface of the Sun.

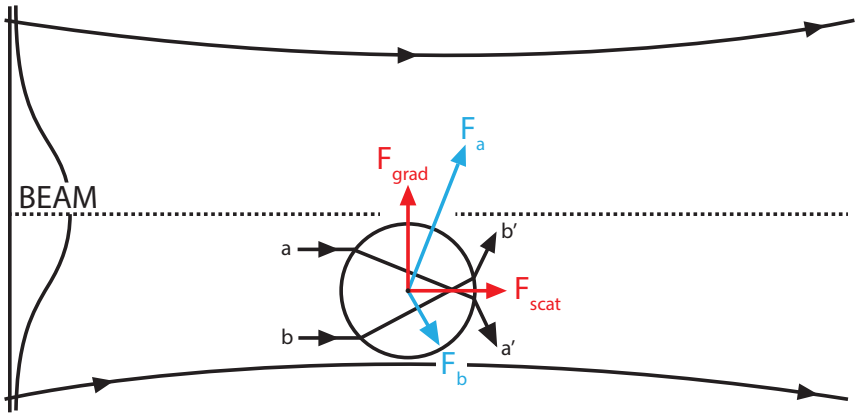

Figure 1.1: Ray optics diagram depicting the origin of $\mathbf{F}_{\text{scat}}$ and $\mathbf{F}_{\text{grad}}$ for a high-index microsphere displaced from the Gaussian beam propagation axis (dashed line).

strumental in the optical manipulation of microparticles. In 1970, Arther Ashkin demonstrated experimentally that the forces of radiation pressure from laser light could be used to accelerate and trap dielectric micron-sized particles [8]. When positioned off-axis in a moderately-focused Gaussian beam, a high-refractive index microparticle immersed in a low-refractive index fluid experiences both an axial scattering force $\mathbf{F}_{\text{scat}}$ oriented along the path of the incident light and a net transverse gradient force $\mathbf{F}_{\text{grad}}$ directed toward the high-irradiance region of the beam, as shown in Fig. 1.1. A simple ray optics analysis of the perturbed particle shows how these two forces arise. Consider a typical pair of light rays a and b striking the particle at symmetric points about its center and exiting the other end as rays a' and b'. In accordance with conservation of momentum, the refraction of the rays through the particle produces forces $\mathbf{F}_a$ and $\mathbf{F}_b$ in the direction of the momentum change. Since the irradiance of ray a is greater than the irradiance of ray b (due to the beam's lateral irradiance gradient), force $\mathbf{F}_a$ must be greater than $\mathbf{F}_b$. Finally, taking the vector sum of $\mathbf{F}_a$ and $\mathbf{F}_b$, plus the forces arising from all other pairs of symmetric rays passing through the particle, we get resultant vectors $\mathbf{F}_{\text{scat}}$ and $\mathbf{F}_{\text{grad}}$. The axial scattering force accelerates the particle along the path of the beam while the transverse gradient force confines it

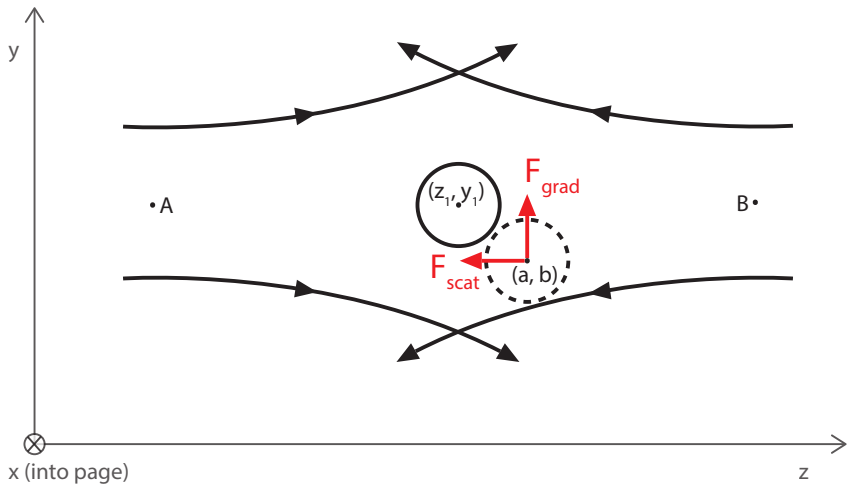

Figure 1.2: Geometry of the original two-beam trap. Two opposing Gaussian beams focused at points A and B intersect along the $z = z_1$ plane. A particle located at the point (z_1, y_1) is in force equilibrium. When the particle is pushed to the point (a, b), forces $\mathbf{F}_{\text{scat}}$ and $\mathbf{F}_{\text{grad}}$ pull the particle back to the equilibrium position. Note: The positive x axis is into the page.

within the trapping circumference of the beam.

Since the initial observations of particle manipulation using light radiation pressure, several unique optical trapping models have emerged [9]. The first three-dimensional trapping configuration was the two-beam trap [8]. It consisted of two counter-propagating Gaussian beams[2] focused at points A and B, as shown in Fig. 1.2. For a particle submerged in water and located at the equilibrium point (z_1, y_1), a net axial scattering force $\mathbf{F}_{\text{scat}}$ opposes any axial displacement, and a net transverse gradient force $\mathbf{F}_{\text{grad}}$ opposes any radial displacement. That is, should the particle be pushed to the point (a, b) by molecular vibrations in the water, the optical forces will restore the particle back to the equilibrium position. Moreover, if one of the beams is blocked, the particle will be pushed foward by the other beam. If the beam is then unblocked, the particle will return to the equilibrium position. This fascinating discovery confirmed

[2]The original two-beam trap implemented the TEM_{00}-mode beam of an argon ion laser. Subsequent two-beam traps used similar geometries with more sophisticated laser technology (see Refs. 17–18).

both the presence of the scattering and gradient forces of radiation pressure as well as the existence of particle guiding and stable three-dimensional trapping.

The single-beam gradient force trap, first demonstrated in 1986 by Ashkin et al. [10], is a convenient and popular tool for manipulating microscopic particles. Commonly called optical tweezers, it can hold and manipulate objects with a high level of precision and flexibility. The tweezers trap consists of a single Gaussian beam focused by an objective lens down to a tight beam waist, as shown in Fig. 1.3. We use a simple geometrical optics formulation to analyze the forces at play on a high-refractive index microsphere submerged in water and positioned approximately one sphere radius below the lens focal point. A pair of symmetric light rays a and b refract through the particle and emerge out the other end as rays a' and b'. As a consequence of the refraction and momentum transfer of the light, forces $\mathbf{F}_a$ and $\mathbf{F}_b$ arise in the direction of the momentum change. Summing vectors $\mathbf{F}_a$ and $\mathbf{F}_b$, plus the forces generated from all other symmetric rays refracting through the sphere, we get the resultant vector $\mathbf{F}_{\mathrm{X}}$,

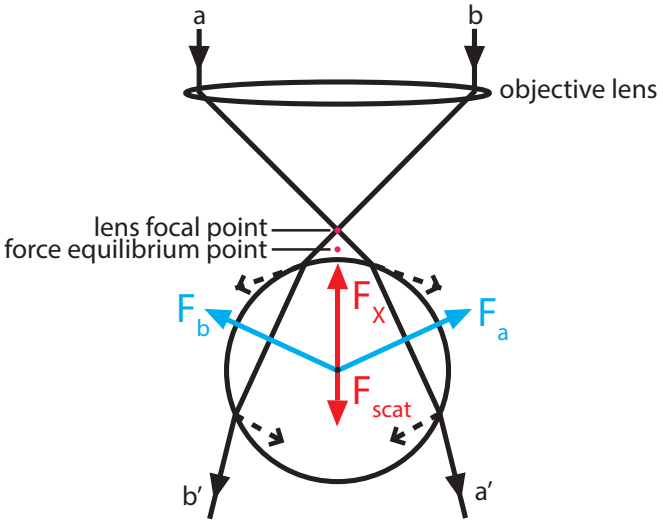

Figure 1.3: Sketch of the single-beam gradient force trap. The interaction of tightly focused laser light with a high-index microsphere gives rise to trapping forces $\mathbf{F}_{\mathrm{X}}$ and $\mathbf{F}_{\mathrm{scat}}$. The forces are in equilibrium just below the focal point of the lens.

an axial gradient force that points upstream[3] toward the beam focus. The scattered rays (depicted with dashed lines) give rise to $\mathbf{F}_{\text{scat}}$, an axial scattering force that is oriented downstream. The two forces are balanced at a stable equilibrium position located just below the beam focus.

The tweezers trap provides a simple, yet elegant, means for stable three-dimensional trapping of large regime particles, including macromolecules, aerosols, colloids, and biological specimens. Moreover, the single-beam gradient force trap was also the first model used in the cooling and trapping of atoms [11], a feat which earned Steven Chu, Claude Cohen-Tannoudji, and William Phillips the Nobel Prize in Physics in 1997. In addition to the tweezers trap and the original two-beam trap, other useful designs for trapping individual particles in single, three-dimensional potential wells have been developed, including the levitation trap [12–16] and the dual fiber trap [17–18].

The standing wave optical trap is an attractive method for manipulating several particles simultaneously in a laser beam lattice. The first Gaussian beam standing wave optical trap designed for Mie[4] regime particles was demonstrated in 1999 by Zemánek et al. [20]. Like optical tweezers, it is a single-beam trap that focuses a beam of laser light to a diffraction-limited spot using a microscope objective. For the setup used by Zemánek et al., an incident Gaussian beam of wavelength λ was focused by a microscope objective and then reflected off a microscope slide that had been coated with an arrangement of reflective dielectric layers whose surfaces were perpendicular to the propagation axis, as shown in Fig. 1.4. Additionally, the beam passed through a liquid medium of refractive index n carrying a collection of 100 nm diameter polystyrene spheres. The superposition of the incident and reflected beams

[3]The upstream axial gradient force $\mathbf{F}_{\text{X}}$ demonstrates the existence of negative radiation pressure. Note: The axial gradient force $\mathbf{F}_{\text{X}}$ is not to be confused with the transverse gradient force $\mathbf{F}_{\text{grad}}$ described earlier.

[4]The first Gaussian beam standing wave optical trap was originally designed for Rayleigh particles in 1998 by Zemánek et al. [19].

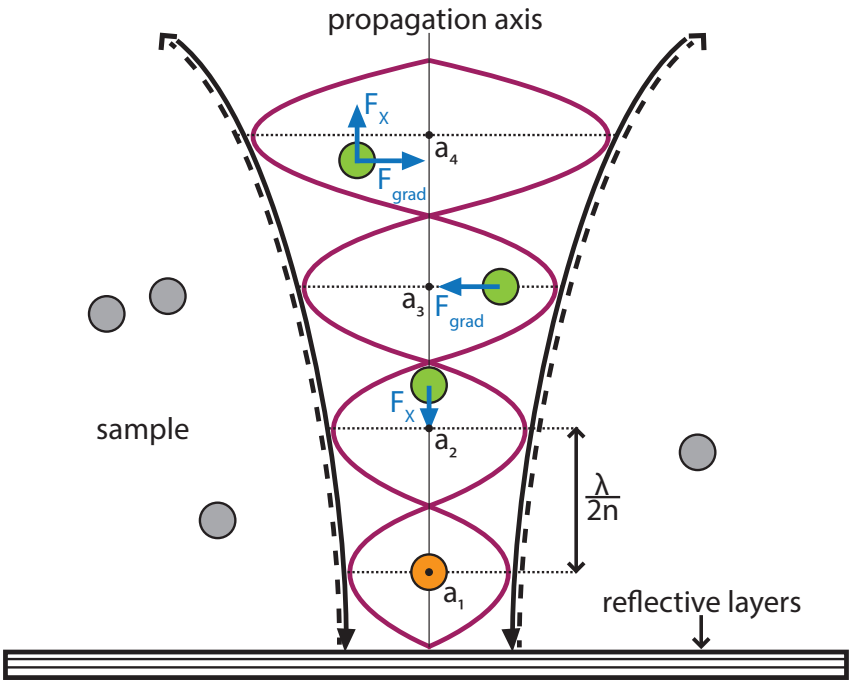

Figure 1.4: Depiction of the Gaussian beam standing wave trap devised by Zemánek et al. A Gaussian beam passed through a sample of polystyrene microspheres and then reflected off an arrangement of reflective dielectric layers situated perpendicular to the propagation axis. The superposition of the incident beam (solid, black curves) and the reflected beam (dashed, black curves) produced an optical standing wave above the reflective layers. The axial gradient forces $\mathbf{F}_{\mathrm{X}}$ and the transverse gradient forces $\mathbf{F}_{\mathrm{grad}}$ guided submerged particles to optical potential wells located near the intersections of the antinodal planes and the propagation axis. In this representative illustration, the free particles (grey) experience no sizeable optical forces; the particles (green) located near the intersections a_2, a_3, and a_4 experience an unbalanced net optical force; and the single particle (orange) positioned at a_1 is in force equilibrium. The equilibrium points are separated axially by $\lambda/2n$, where λ is the beam wavelength and n is the index of refraction of the sample liquid. Note: In reality, the trapped particles are more spaced apart due to particle-induced beam deterioration (see Fig. 1.6).

produced a standing wave optical trap that was capable of confining several particles in separate, three-dimensional potential wells. Assuming the counter-propagating beams were well-aligned, the particles in this setup primarily experienced an axial gradient force $\mathbf{F}_{\mathrm{X}}$ caused by the axial irradiance gradient $\nabla_{\parallel} I$ between the nodes and antinodes of the standing wave and a transverse gradient force $\mathbf{F}_{\mathrm{grad}}$ caused by the lateral irradiance gradient $\nabla_{\perp} I$ of the Gaussian beam. Since the Poynting vector of

the incoming beam nearly canceled that of the reflected beam, the axial scattering force on the particles was negligible. Thus, any particles interacting with the standing wave optical trap would tend to come to rest at the equilibrium positions a_i located near the intersections of the antinodal planes and the propagation axis, and separated axially by $\lambda/2n$. Multiple particles could then be manipulated simultaneously at these points.

Several studies have analyzed the forces at play in standing wave optical traps [21–23]. In particular, Mu et al. demonstrated that the axial gradient force experienced by microspheres trapped in an optical grating was size-dependent [22]. In their setup, when two coherent Gaussian laser beams were focused by an objective lens and intersected in the focal plane, a standing wave interference pattern was generated in this plane, as shown in Fig. 1.5. When polystyrene microspheres were then introduced in the focal plane, an axial gradient force $\mathbf{F}_{\mathrm{X}}$, resulting from the axial irradiance gradient $\nabla_{\parallel} I$ of the standing wave interference pattern along the xy-plane, pulled the spheres toward the antinodes of the beam. Moreover, a transverse scattering force $\mathbf{F}_{\mathrm{scat}}$ oriented along the z-axis pressed the beads against the sample surface. Together these forces tightly confined the particles in multiple, one-dimensional trapping rows. Specifically, the particles were confined by optical forces in the x and z direction, but were free to move one-dimensionally in the y direction.

Using the hydrodynamic-drag method to measure the optical forces on spheres of various bead diameters, Mu et al. demonstrated that the axial gradient force $\mathbf{F}_{\mathrm{X}}$ reached a maximum value near

$$\frac{d}{D} \;=\; 1.40\,, \tag{1.1}$$

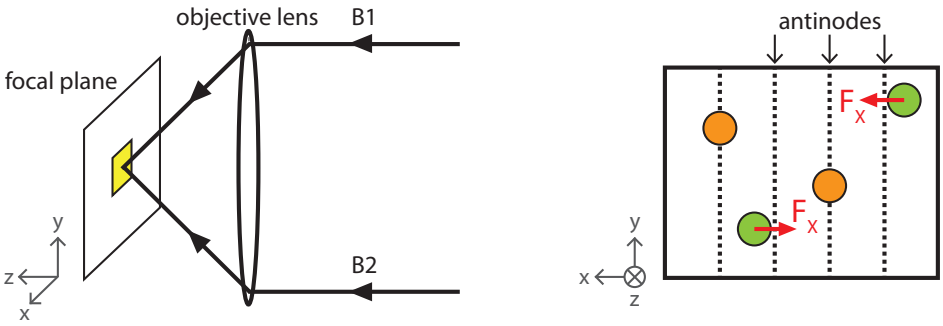

Figure 1.5: Representation of the Gaussian standing wave optical trap devised by Mu et al. Left: When identical Gaussian beams B1 and B2 intersected in the focal plane of an objective lens, an optical standing wave was produced in a two-dimensional trapping area (yellow region) within the focal plane. Right: Schematic of the forces at play in the trapping area. Axial gradient forces $\mathbf{F}_{\mathrm{X}}$ guided the particles toward the antinodes of the standing wave while the transverse scattering force $\mathbf{F}_{\mathrm{scat}}$ (not shown) pushed the particles against the sample surface.

where d is the spatial lattice period[5] and D is the bead diameter. Moreover, the axial gradient force was shown to vanish near

$$\frac{d}{D} \;=\; 0.70\,. \tag{1.2}$$

Aside from their inherent value for optimizing the axial gradient forces in standing wave optical traps, these results also provide a simple mathematical foundation for mesoscopic particle sorting. That is, by selecting a lattice period that minimizes the optical forces acting on particles of a specific diameter while maximizing it for another set of diameters, one can systematically separate different-sized particles submerged in a moving fluid. In addition to the methods devised by Zemánek and Mu, other approaches for achieving simultaneous particle manipulation have been demonstrated, including multiple-beam interference systems [24], laser scanning [25], computer-generated holograms [26], motional standing waves [27], vibrating interfer-

[5]The spatial lattice period of the standing wave is given by $d = \frac{\lambda}{2n}$, where λ is the laser wavelength and n is the index of refraction of the solution.

ence fringes [28], and the Talbot effect [29].

Optical trapping is a continually expanding field. In addition to the trapping models discussed above, several other arrangements have been devised to solve various theoretical questions and experimental challenges. In the next section, we examine the limitations of current optical trapping technology as a tool for tracking particle motion and discuss a novel experimental approach for addressing these shortcomings.

1.2 Motivation

The principal objective of our experiments was to produce an optical trap for measuring transverse particle diffusion. As discussed, extensive progress has been made with three-dimensional optical trapping. However, in order to properly monitor diffusion, the trapped particle must be at least partially free to walk within the trap's potential well. Moreover, to make the analysis less complicated, the particle must also be situated a considerable distance away from any surfaces[6]. To our knowledge, no study has previously demonstrated the use of surface-isolated optical traps for tracking the two-dimensional, lateral motion of microparticles.

The standing wave optical trap provides the ideal arrangement for analyzing the transverse motional dynamics of submerged microparticles. Unlike optical tweezers or two-beam traps, standing wave optical traps are capable of confining several microscopic particles one-dimensionally in multiple, surface-isolated locations. This trapping structure allows the particles to move freely in two-dimensional regions oriented perpendicular to the propagation axis of the beam and eliminates the need to account for surface effects when analyzing the particles' motion. Moreover, it creates

[6]For a discussion of the physical requirement needed to ignore surface effects in optical trapping, see Section 2.4 of this report.

an ideal environment for imaging the particles because the trapping pockets reside well within the optical depth of focus for a typical objective lens. Zemánek demonstrated in [20] that when two counter-propagating beams produce a vertical standing wave in a sample of spherical microparticles, the submerged beads migrate toward the surface-isolated antinodes as they interact with the varying axial irradiance gradient of the standing wave. From this premise, if the beam waist ω is sufficiently wide[7] compared to the particle diameter D, the trapping planes located at each antinode of the standing wave will contain two-dimensional spatial corrals that are optimal for tracking the Brownian motion of trapped particles. However, the multiplicity, uniformity, and stability of these trapping corrals depend on what type of laser beam is implemented.

A Bessel beam is an excellent choice for surface-isolated particle tracking in standing waves[8]. In the previous section, we discussed optical traps made with Gaussian laser beams. While convenient for many applications, Gaussian beams are difficult to employ for surface-isolated particle tracking in standing waves because they have both a high diffraction rate and a low resistance to beam distortion. A Bessel beam, on the other hand, is a much better choice for surface-isolated tracking in standing waves because its cross-sectional area does not spread significantly during propagation [31–33] and it quickly regenerates itself after passing through a particle or other type of obstruction [34–37]. That is, since a Bessel beam has a longer propagation distance and a lower susceptibility to beam modulation compared to a Gaussian beam of a similar beam diameter, the regions of standing wave existence are longer, more uniform, and more stable for a Bessel beam interacting with particles than for a Gaussian beam. A visual

[7] In our experiments, we found that a particle-to-beam waist ratio (D/ω) of approximately 0.02-0.06 was ideal for stable one-dimensional trapping. The authors in [20] did not report a ratio below 0.20 because they were trapping the particles three-dimensionally. For more details on our particular experimental setup, see Chapter 3 of this report.

[8] In addition to Bessel beams, other families of diffractionless beams, such as Mathieu beams [30], may be used for simultaneous trapping in standing waves.

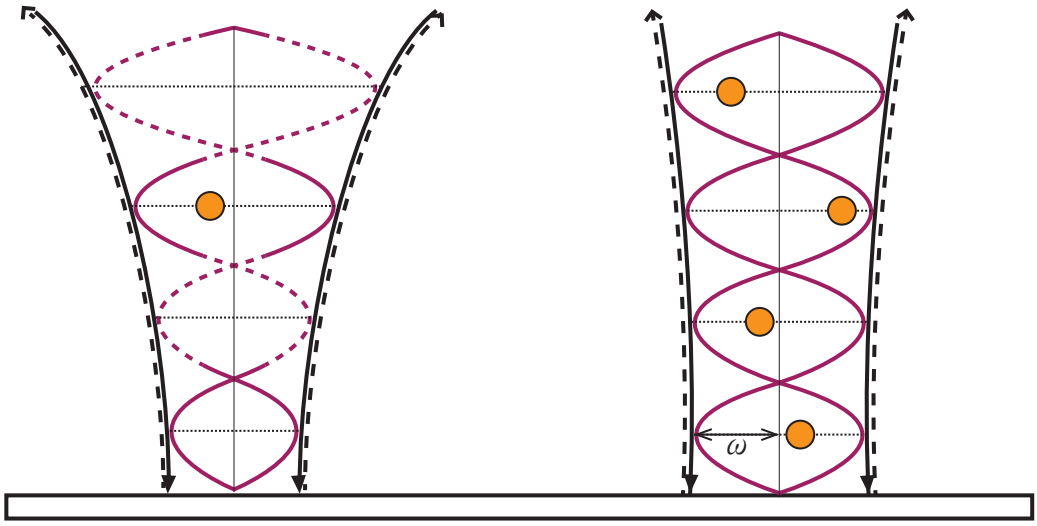

Figure 1.6: Illustration of a Gaussian standing wave trap (left) and a Bessel beam standing wave trap (right). The dashed curves (red) of the Gaussian standing wave represent regions where the beam is distorted. Given a particle-to-beam waist ratio $D/\omega \ll 1$, standing wave optical traps can be used to measure two-dimensional, transverse particle diffusion in multiple, surface-isolated locations. Since Gaussian beams have a higher diffraction rate and a lower resistance to particle-induced beam distortion than Bessel beams, the Bessel beam standing wave trap contains potential wells that are more abundant, uniform, and stable by comparison. Note: The lengths of the deformation regions in the Gaussian standing wave were chosen for convenience in illustrating the general relationship between the two types of beams. Given parameters similar to those used in our experiments, the deformation lengths of both the Gaussian and Bessel beam standing waves would cover several antinodes; however, the deformation lengths of Gaussian beams were shown by Aiello et al. [49] to be roughly twice as long as those of Bessel beams. See Section 2.1.

comparison of a Gaussian standing wave trap and a Bessel beam standing wave trap is shown in Fig. 1.6. To summarize, tracking transverse particle diffusion is optimal in a Bessel beam standing wave trap because the potential wells are two-dimensional, surface-isolated, abundant in number, similar in size, and resistant to particle-induced deterioration.

To our knowledge, the first Bessel beam standing wave trap for microparticles was constructed in 2004 by Čižmár et al. [23]. In this setup, a Gaussian beam operating at a wavelength of 532 nm entered an axicon[9] and emerged from the other end as a Bessel

[9]For more information on constructing a Bessel beam with an axicon, see Section 2.1.

beam with core radius $\omega_B \sim 1\,\mu$m. Similar to the Gaussian beam in [20], the Bessel beam then passed through a sample of submerged microparticles and reflected off of a dielectric mirror normal to its surface. The reflected beam then superimposed on the incident beam, producing a Bessel beam standing wave in the sample. With this optical setup, Čižmár et al. reported simultaneous, three-dimensional confinement of multiple polystyrene Mie particles with diameters in the range of 0.3–2 μm. However, because the particles were tightly trapped in a Bessel beam with a small beam waist, the lateral diffusion of the spheres could not be analyzed. In addition to simultaneous, three-dimensional trapping, Bessel beam standing waves have also been used as optical conveyor belts for submicron particle delivery [38] and as a tool to create holographic periodic structures in photorefractive materials [39].

An analysis of transverse particle dynamics in a single Bessel beam levitation trap[10] was published by Milne et al. in 2007 [40]. Silica microspheres of various sizes were submerged in deuterium oxide and then placed individually inside the rings and central maximum of a 1070 nm Bessel beam using optical tweezers. The trapped particles generally resided close to the sample surface. The characteristic ring width of the Bessel beam was $\Delta\rho = 3.1\,\mu$m, and the mean diameters of the spheres ranged from 2.3–6.8 μm. The particle trajectories were analyzed using particle-tracking software and then compared to theoretical predictions[11] of size-dependent particle motion. As expected, spheres with diameters smaller than $\Delta\rho$ were trapped along the local irradiance maxima of the Bessel beam ring pattern. When the power of the Bessel beam was sufficiently low, these smaller particles hopped from one ring to another,

[10] In [40], particle levitation was only possible in the central maximum of the Bessel beam. The radiation pressure in the surrounding rings was not adequate to lift the particles away from the sample surface.

[11] Theorectical models of the radial force, the transverse radial irradiance, and the radial potential energy associated with spheres of various sizes were developed by Milne et al. using Mie scattering theory and geometrical ray optics. The locations of stable force equilibrium points as a function of sphere radius were also determined.

moving preferentially toward the beam core. Spheres with diameters larger than $\Delta\rho$ either straddled two rings or experienced no periodic field structure. Other spheres in this regime also experienced central maximum equilibrium positions that were spatially offset from the center of the beam core.

While the Bessel beam levitation trap described in [40] has potential applications for static optical sorting, the setup is less than ideal for tracking transverse particle diffusion because the close proximity of the particles to the sample surface would complicate the diffusion analysis. That said, even if the spheres were relocated away from the surface, or placed simultaneously into a vertical array of trapped particles as shown in [41], the Bessel beam levitation trap would present further complications for transverse particle tracking because the vertical motion of each particle would not be well contained. That is, in the absence of strong axial gradient forces, a trapped particle would be more likely to get pushed out of the focal plane of the imaging objective by Brownian forces in the fluid, thus complicating the tracking process. Further work to ensure the stability of the vertical positions of the tracked particles would be required in order to avoid this cumbersome reality.

Previous work on Bessel beam standing waves and particle tracking provides the theoretical framework and motivation to construct a unique optical setup for tracking the Brownian motion of microparticles. We believe this report presents the first realization of two-dimensional, transverse tracking of Mie regime microparticles in multiple, surface-isolated traps. In addition to this advancement in the field of optics, our Bessel beam standing wave trap may also have applications in the fields of microrheology and microfluidics. Specifically, our setup may be used to measure particle diffusion coefficients in semi-dilute polymer solutions, thereby revealing characteristics about the solution's viscosity. Furthermore, it may also be possible to use our trap to study the effects of drag near surfaces, a key element of understanding the physics of

flow inside microfluidic channels.

1.3 Overview

In this thesis report, we discuss the theoretical foundations of our experiments, the methods we used to construct the Bessel beam standing wave trap, the results we obtained, and the future directions of our research. Specifically, in Chapter 2, we explain the fundamental principles and equations governing Bessel beams, the forces involved in our Bessel beam standing wave trap, the optimal conditions for particle confinement and tracking, and the basics of Brownian diffusion theory. In Chapter 3, we provide a detailed account of our Bessel beam trapping setup, including the optical parameters we used to confine and track the particles, and an analysis of the Bessel laser beam at different points along its path. In Chapter 4, we present evidence of multi-level particle confinement in our trap, provide the details of our tracking data and diffusion analysis, and then compare our experimental results for the diffusion coefficients with the theoretical predictions. Finally, in Chapter 5, we conclude with a summary of our findings and a discussion of the potential applications of our work in fluid research and beam characterization.

Chapter 2: Theory

2.1 Bessel Beams

Since their initial conception by Durnin [31], Bessel beams have been examined extensively [42–50]. Two features of Bessel beams that have attracted wide interest are their non-diffracting and self-reconstructive properties. Diffraction affects all classical wave fields and is even foundational to quantum-mechanical uncertainty relations. Prior to the mathematical description of the Bessel beam, it was theorized that all beam-like fields must inevitably undergo diffractive spreading as they travel through free space. Apart from plane waves, no other diffraction-free, electromagnetic solutions were shown to satisfy Maxwell's free space scalar wave equation,

$$\left(\nabla^2 - \frac{1}{c^2}\frac{\partial^2}{\partial t^2}\right) E(\mathbf{r}, t) \;=\; 0, \tag{2.1}$$

where c is the speed of light and $E(\mathbf{r}, t)$ represents a scalar electric field as a function of position $\mathbf{r}$ and time t. However, Durnin demonstrated that Eq. (2.1) has a unique class of diffraction-free mode solutions that, unlike plane waves, describe well-defined beams with narrow central beam radii. The electric field amplitude of a linearly polarized, monochromatic Bessel beam wave propagating in the positive z direction is one such solution:

$$E(\mathbf{r}, t) \;=\; \frac{1}{2}[E_0 e^{i\left(\beta z - \omega t\right)} J_\ell(\alpha r) + \text{c.c.}]. \tag{2.2}$$

Here, E_0 is the peak magnitude of the electric field at the beam center, ω is the angular frequency of the wave, α and β are real constants that satisfy $\alpha^2 + \beta^2 = (\omega/c)^2$,

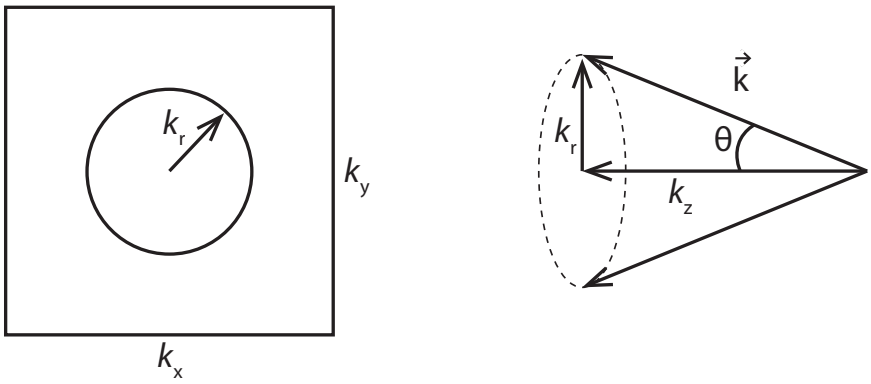

Figure 2.1: Mathematical representation of the angular spectrum of a Bessel light beam. Left: The angular spectrum is defined by a ring with zero thickness in k-space. Right: The Bessel beam wavevectors $k_z\hat{\mathbf{z}}$, $k_r\hat{\mathbf{r}}$, and $\mathbf{k}$ form a conical surface with half angle θ.

$r = \sqrt{x^2 + y^2}$ is the radial displacement from the propagation axis, J_ℓ is the ℓ^{th}-order cylinder Bessel function of the first kind, and c.c. stands for complex conjugate. Since the irradiance $I(\mathbf{r})$, which is proportional to $|E(\mathbf{r})|^2$, is independent of the positive z-axis, the field is propagation invariant. For an ideal Bessel beam traveling through a liquid medium of refractive index n, Eq. (2.2) can be rewritten as [44]

$$E(\mathbf{r}, t) \;=\; \frac{1}{2}[E_0 e^{i\left(k_z z - \omega t\right)} J_\ell(k_r r) + \text{c.c.}], \tag{2.3}$$

where $k_z = |\mathbf{k}| \cos\theta$, $k_r = |\mathbf{k}| \sin\theta$, $|\mathbf{k}| = \frac{2\pi n}{\lambda}$, and θ is the angle between $\mathbf{k}$ and $k_z\hat{\mathbf{z}}$. The angular spectrum of the Bessel beam is represented mathematically as a ring with zero thickness in k-space, where wavevectors $k_z\hat{\mathbf{z}}$, $k_r\hat{\mathbf{r}}$, and $\mathbf{k}$ form a cone with half angle θ, as depicted in Fig. 2.1.

An exact replication of the ideal Bessel beam, which contains infinite energy and is of infinite transverse extent, is not possible in practice. However, over a finite range, a close approximation to the ideal Bessel beam, known as a quasi-Bessel beam [45–46], can be produced using devices such as a circular aperture, a Fabry-Perot cavity,

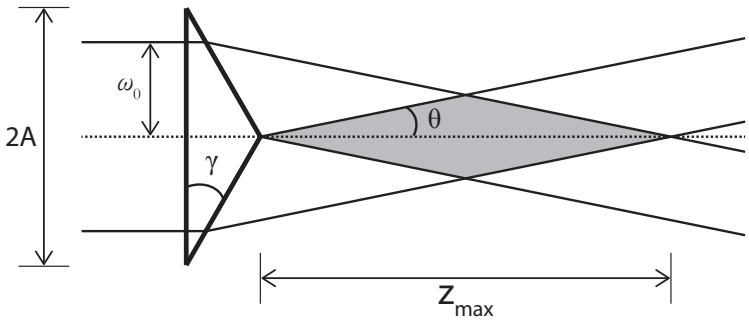

Figure 2.2: Diagram of an axicon-generated Bessel beam. A Gaussian beam with beam waist ω_0 illuminates an axicon with base diameter $2A$ and opening angle γ. The outgoing beam forms a conical surface with half angle θ, approximating an ideal Bessel beam within the range $z_{\max}$.

computer-generated holograms, or an axicon [42, 47]. As illustrated in Fig. 2.2, an axicon is a conical glass lens, defined by base radius A and opening angle γ, that refracts light from a Gaussian beam such that the outgoing beam forms a conical surface of wave vectors in k-space, similar to the mathematical description above. To good approximation in the small angle limit, the half angle θ of the cone is given by the relation [46]

$$\sin(\theta) \;=\; \frac{n_{\rm ax}}{n_0}\cos\!\left(\frac{\pi}{2}-\gamma\right)-\gamma \;\simeq\; \left(\frac{n_{\rm ax}}{n_0}-1\right)\gamma \;\simeq\; \theta, \tag{2.4}$$

where $n_{\rm ax}$ is the refractive index of the axicon and n_0 is the refractive index of the medium surrounding the axicon.

The outgoing Bessel beam is a close estimate of the ideal Bessel beam within a limited range known as the propagation distance, or $z_{\max}$. For an axicon illuminated by a Gaussian beam with beam waist radius ω_0, the propagation distance is given by [48]

$$z_{\max} \;\approx\; \frac{\omega_0}{\sin(\theta)} \;\simeq\; \frac{\omega_0}{\left(\frac{n_{\rm ax}}{n_0}-1\right)\gamma}. \tag{2.5}$$

Alternatively, the propagation distance can be written in wave vector terms via

$$z_{\max} \approx \frac{k\omega_0}{k_r}. \tag{2.6}$$

Moreover, for an ℓ^{th}-order Bessel beam, the peak on-axis irradiance position z_{p} of the Bessel beam occurs at

$$z_{\text{p}} = \frac{\sqrt{2\ell+1}}{2} z_{\max}. \tag{2.7}$$

Past the axicon, the Bessel beam field can be modeled using the stationary phase approximation to the Fresnel integral. As discussed in [48], this approximation produces the following expression for the field irradiance $I^{\ell}(r,z)$ of an ℓ^{th}-order, axicon-generated Bessel beam:

$$I^{\ell}(r,z) = \frac{\pi 2^{\ell+1}}{\ell!}(k_r\omega_0)\left(\frac{P_0}{\pi\omega_0^2/2}\right)\left(\frac{z}{z_{\max}}\right)^{2\ell+1} e^{\left(-2z^2/z_{\max}^2\right)} J_{\ell}^2(k_r r), \tag{2.8}$$

where P_0 is the power of the Gaussian beam incident on the axicon. It has been shown that diffraction from the axicon edges causes undesireable modulation of the on-axis beam irradiance [45]. However, these diffraction effects can be neglected when $\omega_0 < \frac{A}{2}$ [46]. In our experiments, we used an axicon with base radius $A = 12.7\,\text{mm}$ and an incident Gaussian beam with beam waist $\omega_0 = 1.0\,\text{mm}$. Therefore, in our case, we had $\omega_0 \simeq \frac{A}{13}$, so diffraction effects from the axicon edges were negligible. Moreover, axial modulation of the optical irradiance may also arise from the diffraction of light around the curved tip of the axicon. Assuming the radius of curvature of our axicon

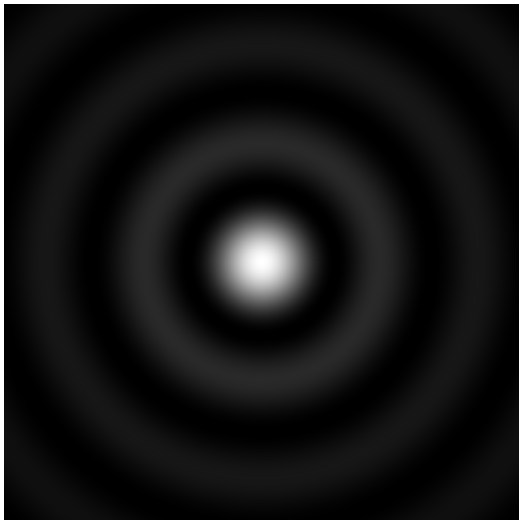

Figure 2.3: Computer-rendered image of the field irradiance $I^{\ell}(r,z)$ of an axicon-generated Bessel beam. The cross-section of the Bessel beam field irradiance consists of a series of concentric circles with a central maximum at the hub. The radius of the central maximum is given by $\omega_{\mathrm{B}} = \frac{2.405}{k_r}$.

tip was similar in size to the one analyzed in [46], we expect some small irradiance modulation in our experiments[1].

The cross-section of the Bessel beam field irradiance $I^{\ell}(r,z)$ contains a series of concentric rings with a central spot at the core, as shown in Fig. 2.3. The central spot and each ring surrounding it contain the same amount of total optical power. However, the peak or maximum irradiance is present in the central spot. For this reason, the central spot is often called the central maximum. The radius ω_{B} of the Bessel beam central maximum is measured from the middle of the central maximum to the first irradiance minimum and is determined by [47]

$$\omega_{\mathrm{B}} \quad = \quad \frac{2.405}{k_r}. \tag{2.9}$$

Note that ω_{B} is independent of the Gaussian beam waist ω_0 incident on the axicon.

[1]For further discussion of the diffraction effects caused by the oblate tip of our axicon, and how this may explain our experimental data, see Section 3.2.

The characteristic distance over which a monochromatic Gaussian beam propagates in free space without considerable spreading is given by the Rayleigh range,

$$Z_R = \frac{\pi n \omega_0^2}{\lambda}, \tag{2.10}$$

where ω_0 is the beam waist, n is the refractive index of the propagation medium, and λ is the laser wavelength in vacuum. Specifically, this range is the distance over which the cross-sectional area of the Gaussian beam doubles. Since the Rayleigh range defines the region where a Gaussian beam is considered non-diffracting, a comparison of Z_R with $z_{\max}$ in quantitative terms offers perspective on the relative non-diffracting span of Bessel beams versus Gaussian beams. We choose values for the axicon ($\gamma = 1\,^\circ$, $n_{\text{ax}} = 1.508$, $n_0 = 1.0$) and the incident Gaussian beam ($\lambda = 1064\,\text{nm}$, $\omega_0 = 1.0\,\text{mm}$, $n = 1.0$) that match our experimental setup described in Chapter 3. Then, for the Bessel beam central maximum radius ω_{B} and the propagation distance $z_{\max}$, we get

$$\omega_{\text{B}} = \frac{2.405}{|\mathbf{k}|\sin\theta} \simeq \frac{2.405}{(2\pi n/\lambda)(\frac{n_{\text{ax}}}{n_0} - 1)\gamma} \simeq 45.9\,\mu\text{m}, \tag{2.11}$$

$$z_{\max} \simeq \frac{\omega_0}{(\frac{n_{\text{ax}}}{n_0} - 1)\gamma} \simeq 113\,\text{mm}. \tag{2.12}$$

In our experiments, we inserted a refracting telescope with angular magnification[2] $M = 10$ after the axicon. We oriented the telescope so that the beam was demagnified. Then, following the telescope, the Bessel beam moved from air ($n_{\text{a}} = 1.0$) to water

[2]The angular magnification M is given by $M = \frac{f_o}{f_e}$, where f_o is the focal length of the objective and f_e is the focal length of the eyepiece.

($n_{\mathrm{w}} = 1.33$) as it entered the sample chamber. Therefore, inside the sample, the central maximum radius and propagation distance become[3]

$$\omega'_{\mathrm{B}} \simeq \frac{\omega_{\mathrm{B}}}{M}\left(\frac{n_{\mathrm{a}}}{n_{\mathrm{w}}}\right) \simeq 3.45\,\mu\mathrm{m}, \tag{2.13}$$

$$z'_{\max} \simeq \frac{z_{\max}}{M^2} \simeq 1.13\,\mathrm{mm}. \tag{2.14}$$

By contrast, the Rayleigh range of a Gaussian beam in water with identical beam waist $\omega_0 = 3.45\,\mu$m and wavelength $\lambda = 1064\,$nm is

$$Z_R = \frac{\pi n_{\mathrm{w}} \omega_0^2}{\lambda} \simeq 46.7\,\mu\mathrm{m}. \tag{2.15}$$

Hence, the non-diffracting distance of the axicon-generated Bessel beam is about 24 times larger than the non-diffracting region of the Gaussian beam. As discussed in the previous chapter, the non-diffracting advantage of Bessel beams, as demonstrated here, is the production of standing wave potential wells that are more numerous and more uniform than those of Gaussian beams. For this reason, a Bessel beam standing wave is a favorable choice for tracking Brownian diffusion.

The self-reconstructive property of Bessel beams is also advantageous for tracking particle motion. The rings of the Bessel beam replenish the central maximum whenever the beam passes through an obstruction. An obstruction of radius r_{ob} placed in the center of a quasi-Bessel beam casts a shadow of length l_{s} given by [37]

[3]Using lens formulas, we discovered that the longitudinal magnification of our refracting telescope was approximately $\frac{1}{M^2}$. Our result closely agrees with Siegman's exact demagnifying factor of $\frac{1}{M^2}$ for a Newtonian telescope (see p. 846 of [51]).

$$l_{\mathrm{s}} \approx \frac{r_{\mathrm{ob}}k}{k_r} = \frac{r_{\mathrm{ob}}z_{\max}}{\omega_0}. \tag{2.16}$$

After this deformation length, the restored beam continues without diffraction for the remainder of its propagation distance. Given values that match our experimental setup[4] ($\omega_0' = 0.1\,\mathrm{mm}$, $z'_{\max} = 1.13\,\mathrm{mm}$), the deformation length produced by a single particle of radius $r_{\mathrm{ob}} = 150\,\mathrm{nm}$ in our Bessel beam standing wave is

$$l_{\mathrm{s}} \simeq \frac{r_{\mathrm{ob}}z'_{\max}}{\omega_0'} \simeq 1.68\,\mu\mathrm{m}. \tag{2.17}$$

Since the trapping planes in the standing wave are separated by $0.4\,\mu$m, the beam reconstructs itself after 5 antinodes. That is, if a particle is trapped at, say, $8\,\mu$m from the origin of the standing wave, or at the 20^{th} antinode, the beam will reform $2\,\mu$m downstream at $10.0\,\mu$m from the origin, or at the 25^{rd} antinode.

According to Aiello et al. [49], the distance required for a Guassian beam to reconstruct 95% of its original shape is roughly twice the distance of that required for an ideal Bessel beam to do the same. Moreover, the Bessel beam reconstructs all of its shape after passing through the obstruction. A Gaussian beam, on the other hand, never quite reaches unity for a non-zero radius r_{ob}. These properties are demonstrated in the following relations:

$$\lim_{z/Z_R\to\infty} \overline{\mathrm{w}}_G(z) = \frac{1}{1 + (r_{\mathrm{ob}}^2/w_0^2)}, \tag{2.18}$$

$$\lim_{z/Z_R\to\infty} \overline{\mathrm{w}}_B(z) = 1. \tag{2.19}$$

[4]Since we are using a telescope that demagnifies the size of the beam, we must divide ω_0 by M, where $M = 10$ is the angular magnification of the telescope. Therefore, we have $\omega_0' = \frac{\omega_0}{10} = 0.1\,\mathrm{mm}$.

Here $\overline{w}_G(z)$ is a measure of the Gaussian beam's ratio of reconstruction, while $\overline{w}_B(z)$ is a measure for that of the Bessel beam. As explained in the previous chapter, beam self-reformation is beneficial in standing wave traps because more particles can be confined simultaneously and the trapping planes are more stable. Thus, in this sense, a Bessel beam is more suitable for tracking particles than a Gaussian beam.

We take advantage of the unique non-diffracting and self-healing properties of Bessel beams to form a convenient standing wave trap for tracking the transverse diffusion of Brownian particles. In the next section, we take a look at the forces at play in our trap.

2.2 Forces in a Bessel Beam Standing Wave

The Bessel beam standing wave trap contains a ladder of individual trapping corrals that are ideal for measuring transverse particle diffusion. Similar to [23], when an axicon-generated Bessel beam is normally incident on a reflective surface, an optical standing wave is generated above the surface, as depicted in Fig. 2.4. If a sample of dielectric microspheres is then introduced in the vicinity of the beam, optical forces arising from light radiation pressure will pull the particles toward the antinodes of the standing wave, trapping them in two-dimensional optical pockets.

Once inside these pockets, the beads move somewhat freely in the horizontal plane of the beam's central maximum but are tightly trapped in the vertical direction. Consider a microsphere positioned upstream from the m^{th} antinode[5] of a zeroth-order Bessel beam[6] standing wave and offset from the propagation axis, as shown in Fig. 2.5.

[5]Here, m is any whole number.

[6]In this disscussion, we consider a beam approximated by the zeroth-order cylinder Bessel function of the first kind, J_0.

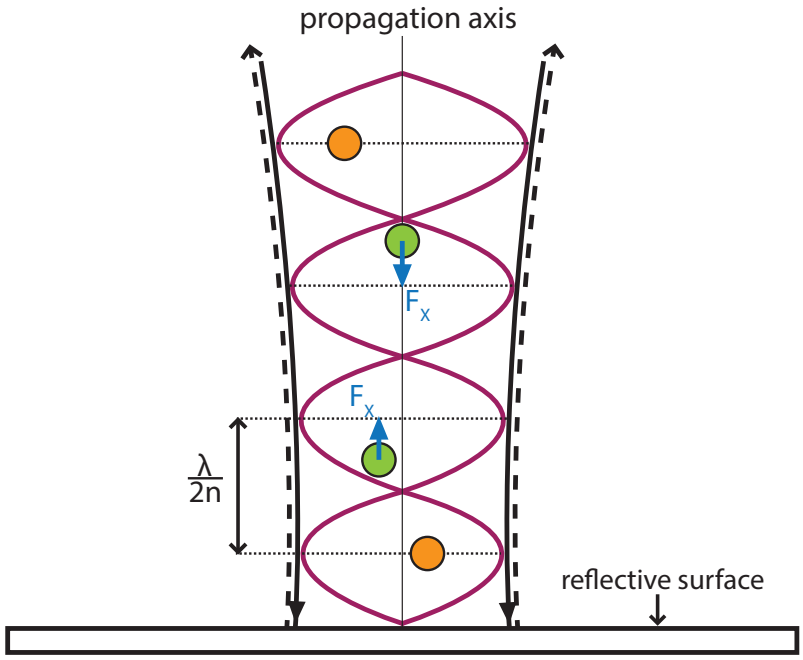

Figure 2.4: Schematic of the Bessel beam standing wave trap. The central maximum of a Bessel beam is normally incident on a reflective surface. The superposition of the incident beam (solid line) and the reflected beam (dashed line) produces an optical standing wave above the surface. Axial gradiant forces $\mathbf{F}_{\mathrm{X}}$ guide displaced particles (green) to trapping planes located close to the antinodes of the standing wave. Inside the central maximum, the axial gradient forces $\mathbf{F}_{\mathrm{X}}$ are much greater than the transverse gradient forces $\mathbf{F}_{\mathrm{grad}}$ or the axial scattering forces $\mathbf{F}_{\mathrm{scat}}$ (both not shown). This scenario allows the particles near the antinodes (orange) to move somewhat freely along the horizontal trapping planes (dotted lines) while remaining tightly trapped in the vertical direction. Note: In our experiments, the trapped particles are more spaced apart due to particle-induced beam deterioration. See Section 2.1.

Similar to the analysis of the displaced bead in Fig. 1.1, an axial scattering force[7] $\mathbf{F}_{\mathrm{scat}}$ and a transverse gradient force $\mathbf{F}_{\mathrm{grad}}$ result from the transfer of momentum by light rays striking and passing through the sphere, with $\mathbf{F}_{\mathrm{scat}}$ pointing downstream and $\mathbf{F}_{\mathrm{grad}}$ pointing in the direction of increasing lateral irradiance (i.e. toward the propagation axis). In addition to $\mathbf{F}_{\mathrm{scat}}$ and $\mathbf{F}_{\mathrm{grad}}$, a relatively much larger axial gradient force $\mathbf{F}_{\mathrm{X}}$ arises from the axial irradiance gradient $\nabla_{\parallel} I^{\ell}_{\mathrm{sw}}(z)$ of the standing wave and

[7]For a partially reflective surface (as is the case in our experimental setup), the incident beam slightly overpowers the reflected beam, producing a small net scattering force in the positive z direction.

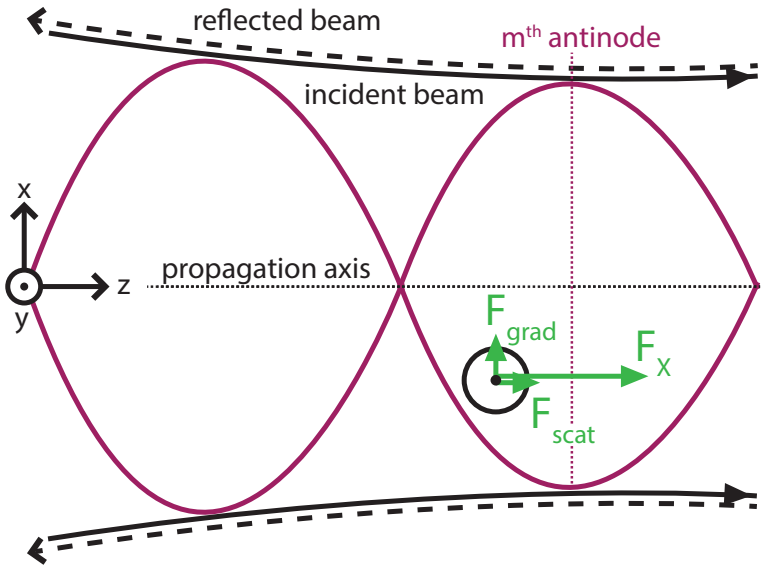

Figure 2.5: Diagram of the forces acting on a microsphere located upstream from the m^{th} antinode of the Bessel beam standing wave and offset from the central maximum propagation axis. At this position, the magnitude of $\mathbf{F}_{\mathrm{X}}$ is much larger in comparison to the magnitudes of $\mathbf{F}_{\mathrm{grad}}$ or $\mathbf{F}_{\mathrm{scat}}$.

points in the direction of increasing axial irradiance (i.e. toward the m^{th} antinode). Assuming the particle has low mass, low volume, and low absorption, we can neglect the gravitational, buoyant, and absorptive forces, respectively. In addition, we ignore surface effects and Brownian forces for the moment[8].

Next, we deduce the dominant forces acting on a bead positioned downstream from the m^{th} antinode, as shown in Fig. 2.6. As before, the scattering force $\mathbf{F}_{\mathrm{scat}}$ points downstream and the transverse gradient force $\mathbf{F}_{\mathrm{grad}}$ points in the direction of increasing radial irradiance. However, in this scenario, $\mathbf{F}_{\mathrm{X}}$ points in the negative z direction since the route of increasing axial irradiance is now oriented upstream.

Adding force vectors $\mathbf{F}_{\mathrm{scat}}$, $\mathbf{F}_{\mathrm{grad}}$, and $\mathbf{F}_{\mathrm{X}}$ for each case, we get resultant vectors $\mathbf{R}_{\mathrm{U}}$ and $\mathbf{R}_{\mathrm{D}}$, where $\mathbf{R}_{\mathrm{U}}$ is the resultant force on the particle positioned upstream, and

[8]See Sections 2.4 and 2.5 for discussions on surface effects and Brownian forces, respectively.

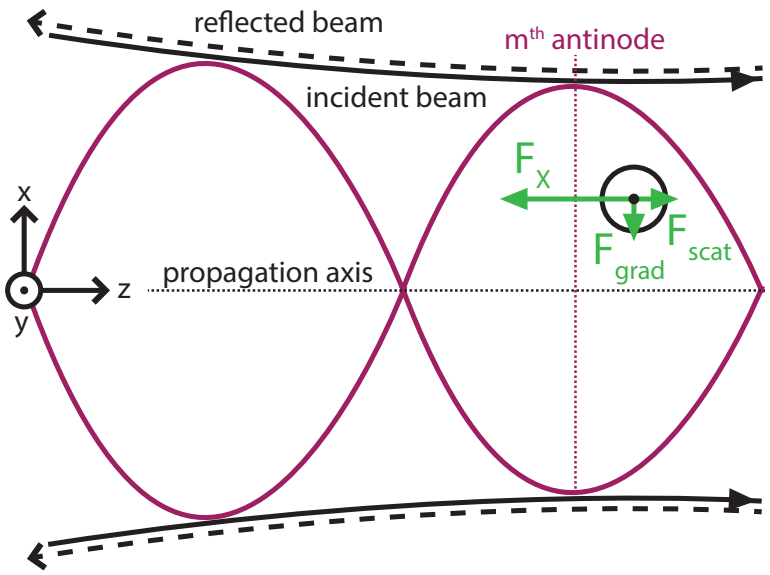

Figure 2.6: Diagram of the forces acting on a microsphere positioned downstream from the m^{th} antinode of the Bessel beam standing wave and offset from the central maximum propagation axis.

$\mathbf{R}_{\text{D}}$ is the resultant force on the particle located downstream (see Fig. 2.7). These resultant forces restore the particle to an equilibrium trapping plane located slightly downstream from the m^{th} antinode. As the particle walks along this plane, the axial gradient force $\mathbf{F}_{\text{X}}$ and the axial scattering force $\mathbf{F}_{\text{scat}}$ are balanced, as shown in Fig. 2.8. The magnitude of the transverse gradient force $\mathbf{F}_{\text{grad}}$ is non-zero at every point other than the propagation axis. Given these conditions, the particle moves according to confined Brownian diffusion[9] inside the two-dimensional corral of the trapping plane.

In our experiments, we studied two particle sizes ($D = 200\,\text{nm}$, $D = 300\,\text{nm}$) that fit squarely in the Mie regime ($D \sim \lambda/\pi$) and one particle size ($D = 100\,\text{nm}$) that hovered near the edge between the Mie regime and the Rayleigh regime ($D < \lambda/10\pi$), where the wavelength λ was 1064 nm for all cases. No analytical solutions currently exist for optical forces in the Mie regime, only numerical solutions. To illustrate the

[9]See Section 2.5 for a discussion of optically-confined Brownian diffusion.

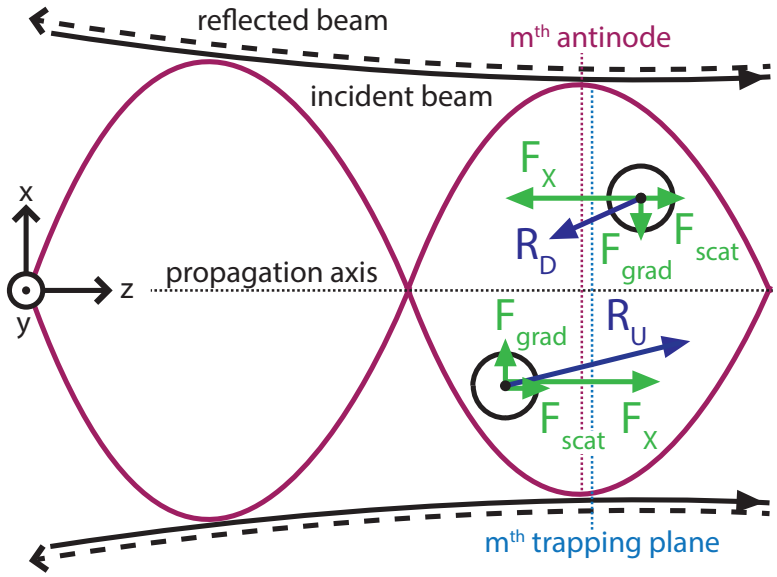

Figure 2.7: Diagram of the resultant forces acting on two displaced microspheres. Forces $\mathbf{R}_{\mathrm{U}}$ and $\mathbf{R}_{\mathrm{D}}$ guide the particles to the m^{th} trapping plane, a force equilibrium plane located slightly downstream from the m^{th} antinode.

relative magnitude of the forces at various positions in the trap, we present graphical representations of the gradient forces using plots of the beam irradiance. By comparing the magnitudes of these forces, we discover that each of the different-sized particles in the Bessel beam standing wave optical trap was more tightly confined in the axial direction than it was in the transverse direction. Additionally, in Section 3.2, we use Rayleigh scattering formulas to calculate rough approximations of the total axial and transverse optical forces acting on the 100 nm diameter particle for a given trapping power.

The magnitude of the axial gradient force $\mathbf{F}_{\mathrm{X}}$ is proportional to the axial irradiance gradient $\nabla_{\parallel} I^{\ell}_{\mathrm{sw}}(z)$ for fixed values of x and y. Meanwhile, the magnitude of the transverse gradient force $\mathbf{F}_{\mathrm{grad}}$ along a specific trapping plane is proportional to the transverse irradiance gradient $\nabla_{\perp} I^{\ell}_{\mathrm{sw}}(x, y)$. To visualize both of these forces, we

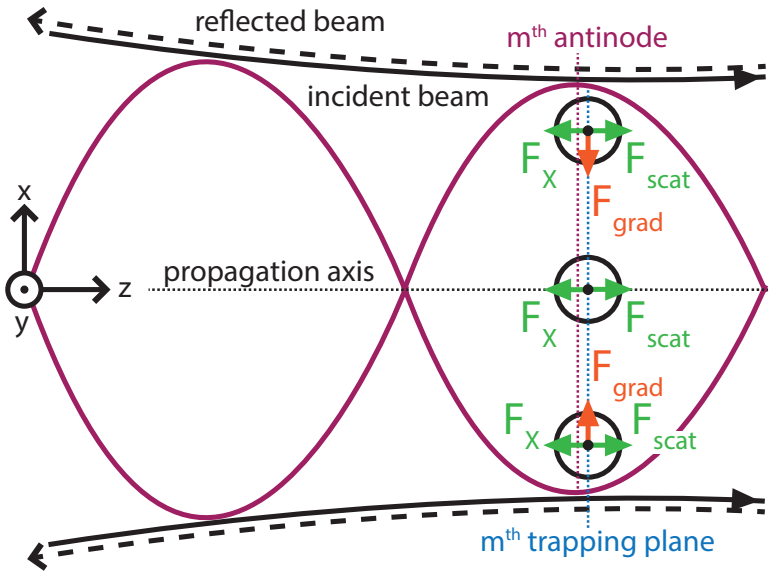

Figure 2.8: Diagram of the forces acting on a microsphere located at three different points along the m^{th} trapping plane. The axial forces $\mathbf{F}_{\text{X}}$ and $\mathbf{F}_{\text{scat}}$ are balanced at each point along the trapping plane. The magnitude of $\mathbf{F}_{\text{grad}}$ is non-zero and unbalanced whenever the particle is displaced from the propagation axis, allowing the particle to move according to confined Brownian diffusion along the trapping plane. Note: To simplify our derivation of $I^{\ell}_{\text{sw}}(x,z)$, we ignore $\mathbf{F}_{\text{scat}}$. This puts the m^{th} trapping plane exactly along the m^{th} antinode.

graph expressions for the field irradiance $I^{\ell}_{\text{sw}}(x, y=0, z)$ in the xz plane and the field irradiance $I^{\ell}_{\text{sw}}(x, y, z=z+h_m)$ in the xy plane of a zeroth-order[10] Bessel beam standing wave, where the spacing between the contour lines in the graphs indicates the relative strengths of $\mathbf{F}_{\text{grad}}$ and $\mathbf{F}_{\text{X}}$.

For simplicity, we assume the irradiance of the incoming beam is equal to the irradiance of the reflected beam, so that the net axial scattering force $\mathbf{F}_{\text{scat}}$ is zero at all points in the standing wave. Under this condition, the m^{th} trapping plane is positioned exactly along the m^{th} antinode. The total field irradiance $I^{\ell}_{\text{sw}}(r, z)$ of the Bessel beam standing wave is proportional to the magnitude squared of the total

[10]For a zeroth-order Bessel beam, $\ell = 0$.

electric field $\mathbf{E}^{\ell}_{\rm sw}(\mathbf{r},t)$ of the standing wave, where $\mathbf{E}_{\rm sw}(\mathbf{r},t)$ is the vector sum of the incoming electric field $\mathbf{E}_{\rm inc}(\mathbf{r},t)$ and the reflected electric field $\mathbf{E}_{\rm ref}(\mathbf{r},t)$. To derive a formula for the total field irradiance $I^{\ell}_{\rm sw}(r,z)$, we used[11] the following expression for the total electric field $\mathbf{E}^{\ell}_{\rm sw}(\mathbf{r},t)$ of the standing wave:

$$\begin{aligned}\mathbf{E}_{\rm sw}(\mathbf{r},t) &= \mathbf{E}_{\rm inc}(\mathbf{r},t) + \mathbf{E}_{\rm ref}(\mathbf{r},t) \\ &= \frac{\hat{x}}{2}[E(r,z)e^{i(kz-\omega t)} + \text{c.c.}] + \frac{\hat{x}}{2}[E(r,[2z'_{\rm p}-z])e^{i(k[2z'_{\rm p}-z]-\omega t)} + \text{c.c.}],\end{aligned} \tag{2.20}$$

where $E(r,z)$ and $E(r,[2z'_{\rm p}-z])$ are the electric field amplitudes of the wave, $\hat{x}$ is the direction of polarization, $r=\sqrt{x^2+y^2}$ is the radial displacement from the propagation axis, k is the wave vector, ω is the angular frequency of the wave, $z'_{\rm p}$ is the location of the peak irradiance after the beam passes through the demagnifying telescope, and c.c. represents the complex conjugate. Using the result from Eq. (26) in Anderson [50], we write the electric field amplitudes $E(r,z)$ and $E(r,[2z'_{\rm p}-z])$ as

$$E(r,z) \;=\; E_0\sqrt{\frac{2\pi z k_r^2}{ik}}e^{-\left(\frac{z}{z_{\max}}\right)^2}e^{\frac{ikr^2}{2z}}e^{\frac{-ik_r^2 z}{2k}}J_\ell(k_r r), \tag{2.21}$$

$$E(r,[2z'_{\rm p}-z]) \;=\; E_0\sqrt{\frac{2\pi(2z'_{\rm p}-z) k_r^2}{ik}}e^{-\left(\frac{2z'_{\rm p}-z}{z_{\max}}\right)^2}e^{\frac{ikr^2}{2[2z'_{\rm p}-z]}}e^{\frac{-ik_r^2(2z'_{\rm p}-z)}{2k}}J_\ell(k_r r), \tag{2.22}$$

where J_ℓ is the ℓth-order Bessel function of the first kind. Then, taking the magnitude squared of $\mathbf{E}_{\rm sw}(\mathbf{r},t)$, we get[12] the following general expression for the total field irradiance $I^{\ell}_{\rm sw}(r,z)$ of an $\ell^{\rm th}$-order Bessel beam standing wave:

[11] For a more detailed discussion of our results for the total electric field $\mathbf{E}_{\rm sw}(\mathbf{r},t)$ and the total field irradiance $I^{\ell}_{\rm sw}(r,z)$, see Appendix A.1.

[12] See Appendix A.1.

$$I^{\ell}_{\rm sw}(r,z) \;=\; \frac{\varepsilon_0 c_0}{4} E_0^2 \left(\frac{2\pi k_r^2}{k}\right) J_\ell^2(k_r r) \Bigg[z e^{-2\left(\frac{z}{z_{\rm max}}\right)^2} + (2z'_{\rm p} - z) e^{-2\left(\frac{2z'_{\rm p}-z}{z_{\rm max}}\right)^2} +$$

$$2\sqrt{z(2z'_{\rm p}-z)}\, e^{-\left(\frac{z}{z_{\rm max}}\right)^2} e^{-\left(\frac{2z'_{\rm p}-z}{z_{\rm max}}\right)^2} \cos\left(k(z'_{\rm p} - z)\left[\frac{r^2}{z(2z'_{\rm p}-z)} + \frac{k_r^2}{k^2} - 2\right]\right)\Bigg]. \qquad (2.23)$$

A plot[13] of the normalized field irradiance $I^0_{\rm sw}(x, y{=}0, z)$ of an axicon-generated, zeroth-order Bessel beam standing wave in the xz plane is shown in Fig. 2.9. The values for the axicon ($\gamma = 1^\circ$, $n_{\rm ax} = 1.508$) and the Bessel beam ($\lambda = 1064\,{\rm nm}$, $z'_{\rm max} = 1.13\,{\rm mm}$) were chosen to correspond to our experimental setup described in Chapter 3. We placed the propagation axis of the beam along the z-axis and the reflective surface of the sample chamber at $z = z'_{\rm p}$, where $z'_{\rm p} = \frac{z'_{\rm max}}{2}$ for a zeroth-order Bessel beam[14]. In this scenario, there are ∼1,400 antinodes[15] contained within the range $0 \le z \le z'_{\rm p}$. To better visualize the standing wave, we zoomed in along the z-axis to $(z'_{\rm p} - 2.0\,\mu{\rm m}) \le z \le z'_{\rm p}$. This range of z values contains only 5 antinodes[16]. The circle of the Bessel beam central maximum is defined by center, $\{x, y\} = \{0, 0\}$, and radius[17], $\omega'_{\rm B} = 3.45\,\mu{\rm m}$, where the radius is measured from the z-axis to the first irradiance minimum. In order to include the central maximum and the first ring of the Bessel beam, we zoomed out along the x-axis to –$8.0\,\mu{\rm m} \le x \le 8.0\,\mu{\rm m}$.

A plot of the normalized field irradiance $I^0_{\rm sw}(x, y, z = z'_{\rm p}{+}h_4)$ of an axicon-generated, zeroth-order Bessel beam standing wave in the xy plane is shown in Fig. 2.10, where

[13] In Appendix A.2, we provide the MATLAB code we used to graph the field irradiance $I^0_{\rm sw}(x, y{=}0, z)$ in the xz plane and the field irradiance $I^0_{\rm sw}(x, y, z = z'_{\rm p} + h_4)$ in the xy plane .

[14] See Eq. (2.7).

[15] The number of antinodes within the range $0 \le z \le z'_{\rm p}$ is determined by $\frac{z'_{\rm p} - 0}{d} = \frac{565\,\mu{\rm m}}{0.4\,\mu{\rm m}} \simeq 1{,}400$.

[16] The number of antinodes within the range $(z'_{\rm p} - 2.0\,\mu{\rm m}) \le z \le z'_{\rm p}$ is determined by $\frac{z'_{\rm p} - (z'_{\rm p} - 2.0\,\mu{\rm m})}{d} = \frac{2.0\,\mu{\rm m}}{0.4\,\mu{\rm m}} = 5$.

[17] See Eq. (2.13).

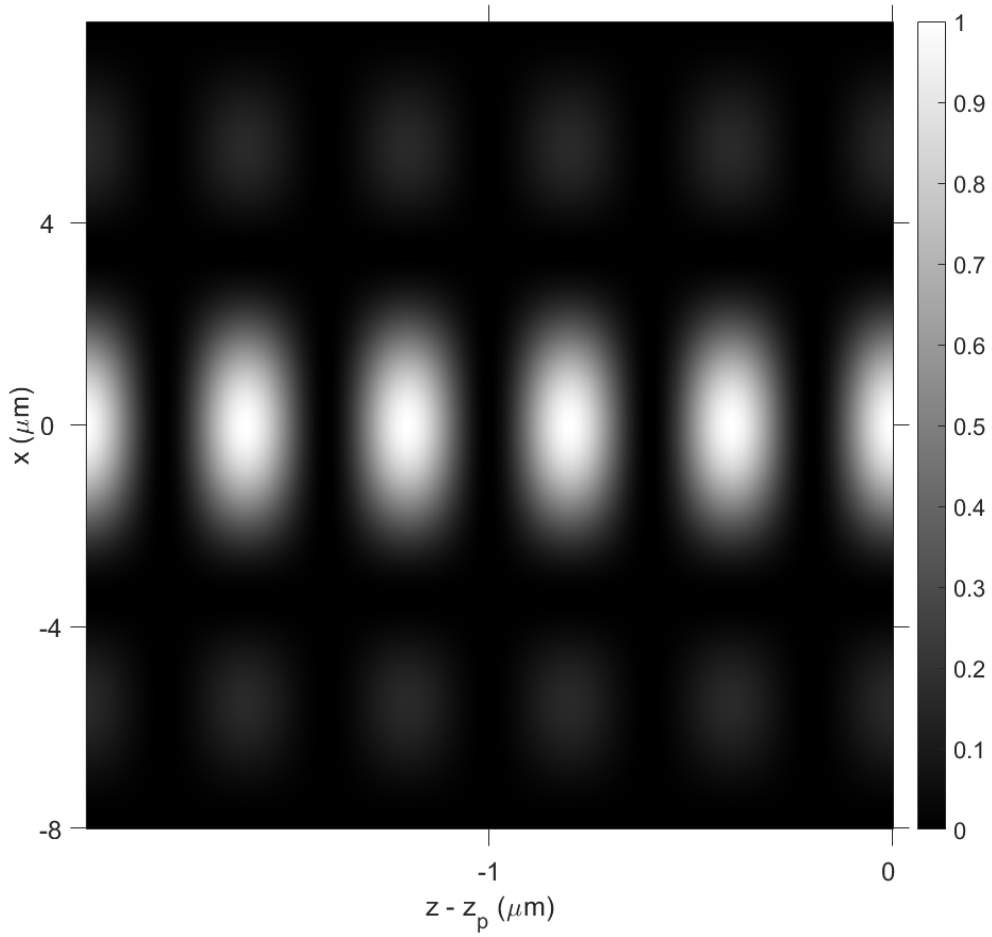

Figure 2.9: Plot of the field irradiance $I^0_{\mathrm{sw}}(x, y{=}0, z)$ of an axicon-generated Bessel beam standing wave in the xz plane. The values for the axicon ($\gamma = 1\,^\circ$, $n_{\mathrm{ax}} = 1.508$) and the Bessel beam ($\lambda = 1064\,\mathrm{nm}$, $z'_{\mathrm{max}} = 1.13\,\mathrm{mm}$) were chosen to match our experimental setup. The circle of the Bessel beam central maximum is defined by center, $\{x, y\} = \{0, 0\}$, and radius, $\omega'_{\mathrm{B}} = 3.45\,\mu\mathrm{m}$. The reflective surface used to produce the standing wave is positioned at $z = z'_{\mathrm{p}}$.

h_4 is the height of the 5$^{\mathrm{th}}$ trapping plane[18] and occurs at $z = (z'_{\mathrm{p}} - 2.0\,\mu\mathrm{m})$. The same values were chosen for the axicon and the Bessel beam that were used in Fig. 2.9. To include the central maximum and the first ring, we zoomed out along the x and y axes to $-8.0\,\mu\mathrm{m} \leq x, y \leq 8.0\mu\mathrm{m}$. As depicted, the field irradiance is azimuthally symmetric about the z-axis.

[18]See Section 2.4.

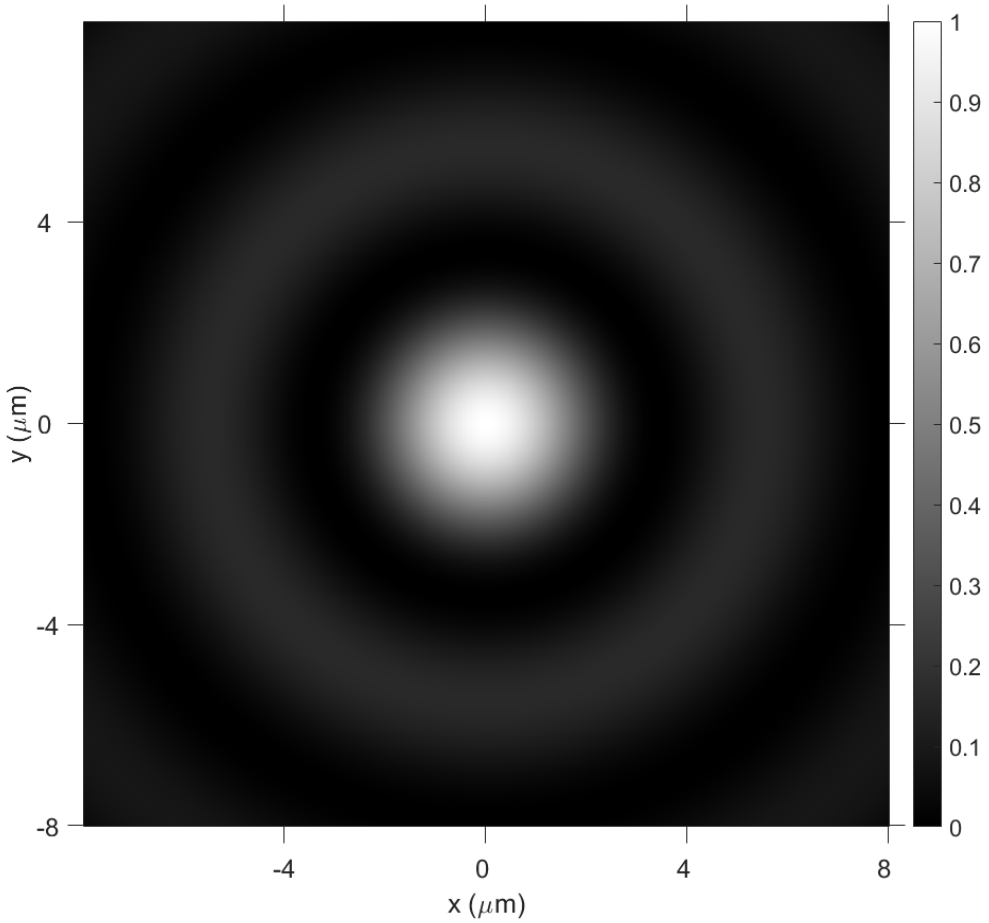

Figure 2.10: Plot of the field irradiance $I^0_{\rm sw}(x, y, z = z'_{\rm p} + h_4)$ of an axicon-generated Bessel beam standing wave in the xy plane . The values for the axicon ($\gamma = 1\,^\circ$, $n_{\rm ax} = 1.508$) and the Bessel beam ($\lambda = 1064\,{\rm nm}$, $z'_{\rm max} = 1.13\,{\rm mm}$) were chosen to match our experimental setup. The circle of the Bessel beam central maximum is defined by center, $\{x, y\} = \{0, 0\}$, and radius, $\omega'_{\rm B} = 3.45\,\mu{\rm m}$. As shown, the field irradiance is azimuthally symmetric about the z-axis (out of the page).

The contour plots of $I^0_{\rm sw}(x, y = 0, z)$ and $I^0_{\rm sw}(x, y, z = z'_{\rm p} + h_4)$ provide graphical representations of the gradient forces acting on a Brownian microparticle moving inside the Bessel beam standing wave (see Figs. 2.11 and 2.12, respectively). For both plots, we used the same values for the axicon and the Bessel beam that were implemented in Figs. 2.9 and 2.10. In Fig. 2.11, to ensure accurate comparison of the axial and transverse forces, we zoomed in along the x-axis to $-2\,\mu{\rm m} \leq x \leq 0\,\mu{\rm m}$. This

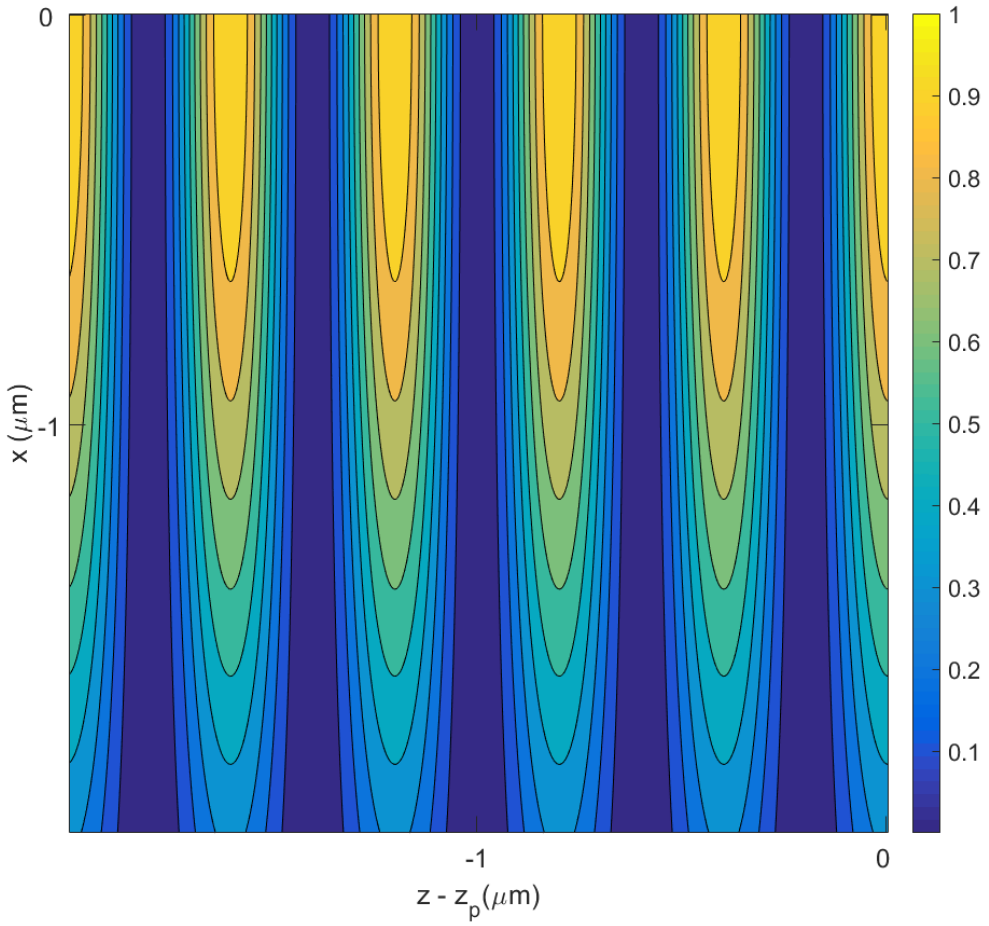

Figure 2.11: Contour plot of the field irradiance $I^0_{\mathrm{sw}}(x, y{=}0, z)$ of an axicon-generated Bessel beam standing wave in the xz plane . The values for the axicon ($\gamma = 1\,^\circ$, $n_{\mathrm{ax}} = 1.508$) and the Bessel beam ($\lambda = 1064\,\mathrm{nm}$, $z'_{\mathrm{max}} = 1.13\,\mathrm{mm}$) were chosen to match our experimental setup. The reflective surface is positioned at $z = z'_{\mathrm{p}}$. The magnitude of $\mathbf{F}_{\mathrm{X}}$ is proportional to the width of the contour lines along the z-axis and the magnitude of $\mathbf{F}_{\mathrm{grad}}$ is proportional to the width of the contour lines along the xy plane. Thus, $\mathbf{F}_{\mathrm{X}} \gg \mathbf{F}_{\mathrm{grad}}$ in the Bessel beam central maximum.

range of x values matches the scale chosen for the z-axis. Since $\mathbf{F}_{\mathrm{X}}$ is proportional to the axial irradiance gradient $\nabla_{\parallel} I^{\ell}_{\mathrm{sw}}(z)$ for given values of x and y, the magnitude of $\mathbf{F}_{\mathrm{X}}$ is proportional to the width of the contour lines in the z direction. Similarly, since $\mathbf{F}_{\mathrm{grad}}$ is proportional to the transverse irradiance gradient $\nabla_{\perp} I^{\ell}_{\mathrm{sw}}(x, y)$ for a fixed value of z, the strength of $\mathbf{F}_{\mathrm{grad}}$ is proportional to the width of the contour lines along a particular xy plane. Comparing the widths of the contour lines along the axial and

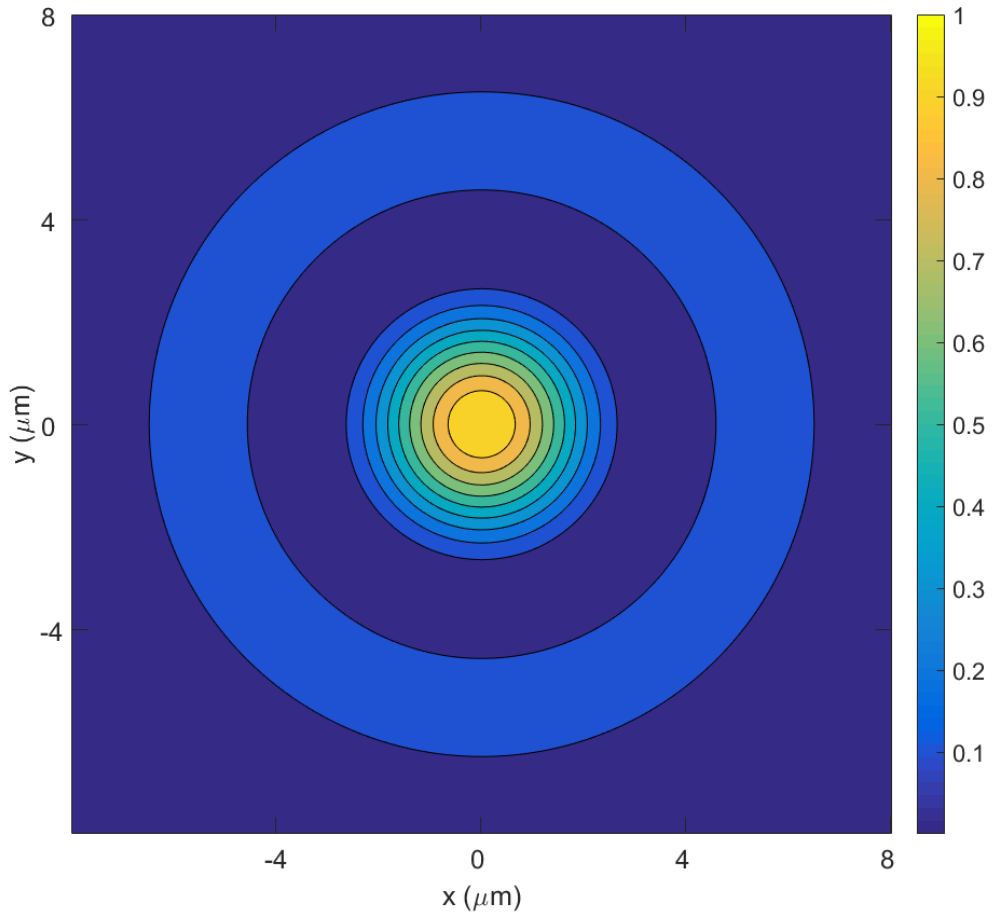

Figure 2.12: Contour plot of the field irradiance $I^0_{\mathrm{sw}}(x, y, z = z'_{\mathrm{p}} + h_4)$ of an axicon-generated Bessel beam standing wave in the xy plane . The values for the axicon ($\gamma = 1\,^\circ$, $n_{\mathrm{ax}} = 1.508$) and the Bessel beam ($\lambda = 1064\,\mathrm{nm}$, $z'_{\mathrm{max}} = 1.13\,\mathrm{mm}$) were chosen to match our experimental setup. The magnitude of $\mathbf{F}_{\mathrm{grad}}$ is proportional to the width of the contour lines along the xy plane. Thus, $\mathbf{F}_{\mathrm{grad}}$ is axially symmetric.

transverse axes in Fig. 2.11, we conclude that the magnitude of the axial gradient force $\mathbf{F}_{\mathrm{X}}$ is much greater than the magnitude of the transverse gradient force $\mathbf{F}_{\mathrm{grad}}$ in the regions between the nodes and antinodes of the Bessel beam standing wave. We also observe in Fig. 2.12 that $\mathbf{F}_{\mathrm{grad}}$ is axially symmetric. Thus, the particles in our Bessel beam standing wave trap are tightly bound in the z direction but partially free to move along the xy plane of the central maximum.

In conclusion, the particles experience three dominant optical forces: (1) an axial

scattering force $\mathbf{F}_{\text{scat}}$ produced by the net downward momentum of scattered light, (2) a transverse gradient force $\mathbf{F}_{\text{grad}}$ caused by the varying radial irradiance in the Bessel beam central maximum, and (3) an axial gradient force $\mathbf{F}_{\text{X}}$ generated by the oscillating axial irradiance of the standing wave. Together these forces give rise to the optical trapping lattice of the beam.

2.3 Force Optimization

The optimal scenario for tracking particle motion in the Bessel beam standing wave trap requires that we maximize the axial gradient force $\mathbf{F}_{\text{X}}$, minimize the axial scattering force $\mathbf{F}_{\text{scat}}$, and adjust the transverse gradient force $\mathbf{F}_{\text{grad}}$ so that the particle is free to drift along the optical trapping plane without escaping the beam.

We maximize the axial gradient force $\mathbf{F}_{\text{X}}$ by selecting particle diameters that most accurately satisfy Eq. (1.1). For particles submerged in water ($n = 1.33$) and trapped using an infrared laser ($\lambda = 1064\,\text{nm}$), we obtain a lattice period of $d = 400\,\text{nm}$. Plugging this into Eq. (1.1), we find that

$$D_{\text{max}} \;=\; \frac{400\,\text{nm}}{1.40} \;=\; 286\,\text{nm} \tag{2.24}$$

is the optimal particle diameter for maximizing the axial gradient force. Moreover, using Eq. (1.2), we find that the magnitude of $\mathbf{F}_{\text{X}}$ goes to zero for particles with diameter

$$D_{\text{min}} \;=\; \frac{400\,\text{nm}}{0.70} \;=\; 571\,\text{nm}. \tag{2.25}$$

The size of the axial scattering force $\mathbf{F}_{\text{scat}}$ depends on how much of the incident radiation is canceled out by the reflected radiation. In our experiments, we minimize

$\mathbf{F}_{\text{scat}}$ by shining the incident beam on a surface coated with a reflective film. The value of the reflection coefficient R of the film is determined by

$$\mathrm{R} \;=\; \frac{P_{\text{ref}}}{P_{\text{inc}}}, \tag{2.26}$$

where P_{ref} is the power of the beam reflected off the coated surface, and P_{inc} is the power of the incident beam. Although a reflection coefficient of R = 1.0 represents the ideal scenario for minimizing $\mathbf{F}_{\text{scat}}$, we are restricted by the condition that some laser light must be transmitted in order to image the beam. Thus, a reflection coefficient in the range $0.85 \leq \mathrm{R} \leq 1.0$ satisfies both requirements.

In theory, the maximum value of $\mathbf{F}_{\text{grad}}$ along the m^{th} trapping plane of the Bessel beam standing wave occurs at the first zero of $\frac{\partial^2}{\partial r^2} J_0^2(k_r r)$, where $J_0^2(k_r r)$ is the square of the zeroth-order Bessel function and is proportional to the transverse irradiance gradient $\nabla I^0_{\text{sw}}(x, y, z = z'_{\text{p}} + h_m)$. Then, by extension, we consider the distance from the center of the Bessel beam to $\frac{a_1}{k_r}$, where a_1 is the first zero of $\frac{\partial^2}{\partial r^2} J_0^2(r)$, to be the maximum trapping radius T.R. of the confined particles because the value of $\mathbf{F}_{\text{grad}}$ at this point will tend to exceed the value of the Brownian forces pushing the particle out of the trap. That is, the smaller the value of T.R., the more tightly the particle will be confined along each two-dimensional trapping plane of the Bessel beam standing wave. The value of T.R. is given by

$$\text{T.R.} \;=\; \frac{1.804}{k_r} \;=\; \omega_{\text{B}}\left(\frac{1.804}{2.405}\right), \tag{2.27}$$

where ω_{B} is the radius of the Bessel beam central maximum as defined by Eq. (2.9). For particle diameters between 100–300 nm, a value of T.R. around 2–3 μm would give the particles ample room to diffuse while still remaining confined inside the trap.

2.4 Surface-isolated Trapping

Using the classical wave model of light, we can determine the vertical heights h_m of each antinode in terms of the wavelength λ of the light. As depicted in Fig. 2.13, the first antinode occurs at $\frac{1}{4}\lambda_n$ above the reflective surface, where λ_n is the wavelength of light measured in a sample solution of refractive index n and is given by

$$\lambda_n \;=\; \frac{\lambda}{n}. \tag{2.28}$$

The second antinode is one-half of a wavelength above the first antinode at $\frac{3}{4}\lambda_n$, and the third antinode is one-half of a wavelength up from the second at $\frac{5}{4}\lambda_n$, and so on. We generalize h_m in the following way:

$$h_m \;=\; \frac{\lambda_n}{4}\,(2m+1), \tag{2.29}$$

where m =0, 1, 2, ... Since m starts at zero, the height of the first antinode is h_0, the height of the second is h_1, and so on. For a sample of thickness H, the vertical height is bounded by the condition $h_m \leq H$. For a microsphere with diameter $D = 300\,\text{nm}$ trapped in a beam with wavelength $\lambda = 1064\,\text{nm}$, the diameter can be expressed in terms of the wavelength via

$$D \;=\; \frac{300}{1064}\lambda \;\simeq\; 0.282\lambda. \tag{2.30}$$

Then Eq. (2.29) can be written as

$$h_m \;=\; \left(\frac{1064}{300}\right)\frac{D}{4n}\,(2m+1) \;\simeq\; \frac{0.887D}{n}\,(2m+1). \tag{2.31}$$

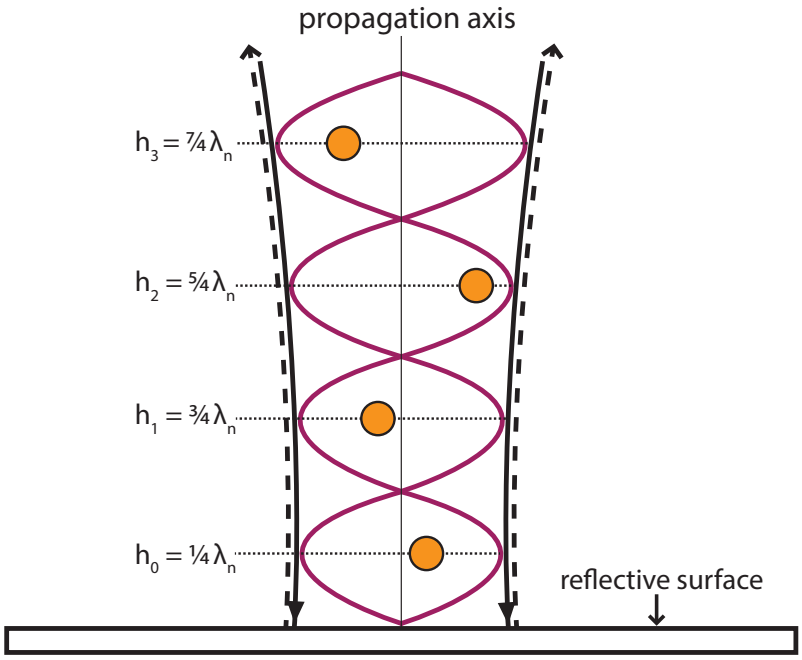

Figure 2.13: Depiction of the Bessel beam standing wave trap with antinode heights h_0–h_3 indicated on the left. Inside the two-dimensional spatial corrals located near each antinode (dotted lines), the trapped particles (orange) move according to confined Brownian diffusion. Using values similar to our experimental setup ($\lambda = 1064\,\text{nm}$, $D = 300\,\text{nm}$), we show that surface forces are negligible for heights h_m where $m \geq 4$.

The particle with diameter $D = 300\,\text{nm}$ was the largest[19] microsphere we tested in our experiments; thus, it represents the worst case scenario for surface effects because it experienced the largest surface forces compared to the other particle sizes. In [52], the authors conclude that surface effects can be ignored when the particle is displaced from all surfaces by at least 5 particle diameters. To satisfy this requirement for our optical setup, we let $h_m = 5D$. Then, solving for m for the 300 nm particle, we get[20]

[19]For our trapping experiments, we had a laser wavelength of $\lambda = 1064\,\text{nm}$ and particle diameters of 100, 200, and 300 nm. For the 100 nm particle, $D = 0.094\lambda$, and for the 200 nm particle, $D = 0.188\lambda$.

[20]The formulas for the 100 nm and 200 nm particles are $m = \left\lceil \frac{1.88n-1}{2} \right\rceil$ and $m = \left\lceil \frac{3.76n-1}{2} \right\rceil$, respectively.

$$m \;=\; \left\lceil \frac{5.64n-1}{2} \right\rceil, \tag{2.32}$$

where the notation $\lceil\ \rceil$ represents the ceiling function. At or above the m^{th} antinode, surface forces are negligible. If the microsphere is immersed in water ($n = 1.33$), we get $m = 4$. Thus, for[21]

$$m \;\geq\; 4, \tag{2.33}$$

our Bessel beam standing wave trap can be used to analyze transverse Brownian diffusion without having to account for surface effects.

2.5 Brownian Diffusion

A mathematical model of Brownian diffusion in an optical trap can be derived from Newton's Second Law and general Langevin dynamics [53]. The equation of motion for the finite trajectory of an optically-perturbed Brownian particle of mass M in a uniform viscous medium is

$$M\ddot{\mathbf{r}} \;=\; -\nabla V(\mathbf{r}) - \gamma\dot{\mathbf{r}} + \sqrt{2\gamma k_B T}\Gamma(t), \tag{2.34}$$

where $V(\mathbf{r})$ is the optical confining potential, γ is the fluid drag coefficient, k_B is Boltzmann's constant, T is the temperature of the medium, Γ(t) is the zero-average Gaussian white noise, and $\mathbf{r} = x\hat{x} + y\hat{y} + z\hat{z}$ is the particle's position as a function of time t. This relation is the standard Langevin equation with net external force

[21] Inserting $n = 1.33$ into the expressions from the previous footnote, we get lower limits on m for the two smaller particles. For the 100 nm diameter particle, we get $m \geq 1$ and for the 200 nm diameter particle, we get $m \geq 2$. Therefore, $m \geq 4$ satisfies the requirement from [52] for all particle sizes.

$F_e(\mathbf{r}) = -\nabla V(\mathbf{r})$ added to account for the effect of an optical potential. In our setup, since the inertial term $M\ddot{\mathbf{r}}$ is small compared to the drag term $\gamma\dot{\mathbf{r}}$, we can ignore the inertial term. Then, using Einstein's formula for the theoretical diffusion coefficient of the particle,

$$D_{\text{theo}} \;=\; \frac{k_B T}{\gamma}, \tag{2.35}$$

we get a simplified form of Eq. (2.34) known as the overdamped Langevin equation [54]:

$$\dot{\mathbf{r}} \;=\; -\frac{\nabla V(\mathbf{r})}{\gamma} + \sqrt{2D_{\text{theo}}}\Gamma(t). \tag{2.36}$$

For a particle moving along the m^{th} trapping plane of our Bessel beam optical trap (see Fig. 2.8), the confining potential $V(\mathbf{r})$ is given by

$$V(\mathbf{r}) \;=\; -n_{\text{back}}\alpha\frac{|\mathbf{E}^0_{\text{sw}}(r,z)|^2}{2} \tag{2.37}$$

where n_{back} is the refractive index of the background viscous medium[22], α is the polarizability of the particle, $r = \sqrt{x^2+y^2}$ is the particle's position from the z-axis, and $|\mathbf{E}^0_{\text{sw}}(r,z)|^2$ is the magnitude squared of the total electric field of an axicon-generated, zeroth-order Bessel beam standing wave and is proportional[23] to the total field irradiance $I^0_{\text{sw}}(r,z)$ of the standing wave. Since we are only tracking transverse Brownian diffusion, we assume that the z contribution to $V(\mathbf{r})$ is a square potential with infinite boundaries on either side of the m^{th} trapping plane. That is,

$$V(\mathbf{r}) \;=\; \begin{cases} 0 & z = z'_{\text{p}} + h_m, \\ \infty & \text{otherwise.} \end{cases}$$

[22]In our experiments, the particles were immersed in water. Therefore, $n_{\text{back}} = 1.33$.

[23]See Eq. (A.4).

where z'_{p} is the location of the peak irradiance of the Bessel beam and h_m is the vertical height of the m^{th} antinode. Then, inside the two-dimensional corral of the m^{th} trapping plane, we have

$$\dot{\mathbf{r}} \;=\; \frac{n_{\mathrm{back}}\alpha\nabla I^0_{\mathrm{sw}}(r, z=z'_{\mathrm{p}}+h_m)}{\varepsilon_0 c_0 \gamma} + \sqrt{2D_{\mathrm{theo}}}\Gamma(t), \tag{2.38}$$

where ε_0 is the electric permittivity of free space and c_0 is the speed of light in vacuum.

To calculate the theoretical diffusion coefficient D_{theo} of the particle, we invoke Stokes's formula and combine it with Einstein's formula (Eq. 2.34). Stokes's formula states that a spherical object of radius R moving with small velocity v through a fluid of dynamic viscosity η experiences a net drag force with magnitude equal to

$$F_{\mathrm{drag}} \;=\; 6\pi\eta R v. \tag{2.39}$$

By definition, the drag coefficient γ is simply the net drag force F_{drag} divided by the object's velocity v. Therefore, we have

$$\gamma \;=\; 6\pi\eta R. \tag{2.40}$$

Combining Eqs. (2.35) and (2.40), we get the Stokes-Einstein-Sutherland equation:

$$D_{\mathrm{theo}} \;=\; \frac{k_B T}{6\pi\eta R}. \tag{2.41}$$

Sutherland is included in the name because Albert Einstein and William Sutherland published Eq. (2.35) independently in 1905. The central result of Einstein's theory of diffusion relates the experimental diffusion coefficient D_{msd} to the mean-square displacement (MSD) $\rho(\tau)$ of a freely diffusing particle over some finite time interval τ by

$$\rho(\tau) \;=\; 2nD_{\mathrm{msd}}\tau, \tag{2.42}$$

where n is the number of spatial dimensions and $\rho(\tau)$ is defined by [55]

$$\rho(\tau) \;=\; \lim_{t\to\infty} \left\langle \left[\mathbf{r}(t+\tau) - \mathbf{r}(t)\right]^2 \right\rangle. \tag{2.43}$$

Thus, for two dimensions, we have

$$\rho(\tau) \;=\; 4D_{\mathrm{msd}}\tau. \tag{2.44}$$

Because Eq. (2.44) assumes particle diffusion absent any external potential, this relation cannot fully describe the transverse motion of particles in our Bessel beam trap. On the other hand, a fit of the first three points of $\rho(\tau)$ to $4D_{\mathrm{msd}}\tau$ does provide us with a reasonable, though underestimated, approximation for the diffusion coefficient D_{msd}. To partially account for the optical potential in our Bessel beam trap, we use the generic expression for confined diffusion given by [56]

$$\rho(\tau) \;=\; \frac{L_{\mathrm{m}}^2}{3}\left(1 - e^{-\frac{\tau}{\tau_{\mathrm{m}}}}\right), \tag{2.45}$$

where L_{m} is the measured microdomain of confinement, assumed to be a square with dimensions $L_{\mathrm{m}} \times L_{\mathrm{m}}$, and τ_{m} is the measured equilibriation time and is related to the diffusion coefficient D'_{m} for confined motion via

$$D'_{\mathrm{m}} \;=\; \frac{L_{\mathrm{m}}^2}{12\tau_{\mathrm{m}}}. \tag{2.46}$$

The value given by Eq. (2.46) is a low estimate of the actual diffusion coefficient of the particle because it does not account for the motion of the particle during the

exposure time T of the detector. In our experimental setup, we used a CCD (charge-coupled device) camera with an average exposure time of $T \simeq \frac{1}{15\,s^{-1}} = 0.067\,\mathrm{s}$. While the camera collects an image during time T, the particle is still moving. To account for this undetected, correlated motion, Destainville et al. [56] derived the following expressions for the corrected microdomain L_{msd} and the corrected equilibriation time τ_{msd}:

$$\tau_{\mathrm{msd}} \;=\; \tau_{\mathrm{m}} - \frac{T}{3}, \tag{2.47}$$

$$L_{\mathrm{msd}} \;=\; \frac{L_{\mathrm{m}}}{\sqrt{2\frac{\tau_{\mathrm{msd}}}{T} - 2\left(\frac{\tau_{\mathrm{msd}}}{T}\right)^2\left(1 - e^{-T/\tau_{\mathrm{msd}}}\right)}}. \tag{2.48}$$

These detector-corrected solutions are model independent, so they apply to any type of confining potential. On the other hand, Eq. (2.47) is only valid when $\frac{\tau_{\mathrm{msd}}}{T} < 10$. For larger values of $\frac{\tau_{\mathrm{msd}}}{T}$, a more complicated expression for τ_{msd} provided in [56] must be invoked. Finally, to obtain the corrected diffusion coefficient D'_{msd} for confined motion, we insert our corrected values τ_{msd} and L_{msd} into Eq. (2.46) to obtain

$$D'_{\mathrm{msd}} \;=\; \frac{L^2_{\mathrm{msd}}}{12\tau_{\mathrm{msd}}}. \tag{2.49}$$

In Chapter 3, we present a novel experimental approach for collecting the transverse tracking data of diffusing Brownian particles in a viscous medium. In Chapter 4, we use this data to calculate $\rho(\tau)$ for finite trajectories of the particles, then fit the resulting points of $\rho(\tau)$ to Eqs. (2.44) and (2.45) to extract experimental values for D_{msd} and D'_{m}. Then, as discussed, we correct for the exposure time of our camera using Eqs. (2.47) and (2.48) to get D'_{msd}. Finally, we compare our experimental results with the theoretical values D_{theo} obtained from Eq. (2.41).

Chapter 3: Methods

3.1 The Bessel Beam Standing Wave Trap

The experimental setup for the Bessel beam standing wave trap is illustrated in Fig. 3.1, and the measurements between the various optical components are specified in Fig. 3.2. For the light source, we used an IPG Photonics fiber laser ($\lambda = 1064\,\text{nm}$, $P = 3$–$15\,\text{W}$) operating in TEM_{00} mode. Light emitted from the source was linearly polarized with a minimal ratio of 50:1 (17dB) and a typical ratio of 100:1 (20dB) in the power of linearly vs. randomly polarized light present in the beam. The power of the Gaussian beam was first reduced to a reasonable level with a 25% reflective mirror. Then, after reflecting off three infrared mirrors (BD2, $\text{R} \simeq 100\%$), the beam illuminated a crown glass axicon (Del Mar Photonics, $\gamma = 1^\circ$, $A = 12.7\,\text{mm}$, $n_{\text{ax}} = 1.508$), transforming the Gaussian beam into a zeroth-order Bessel beam of the first kind with non-diffracting central maximum. The beam waist ω_0 of the Gaussian beam incident on the axicon was measured[1] to be $\sim$1.0 mm. As much as possible, we ensured that the irradiance distribution of the resulting Bessel beam was azimuthally symmetric. In the region between the axicon and the first lens, we found[2] that the theoretical central maximum radius was $\omega_B \simeq 45.9\,\mu\text{m}$ and the theoretical propagation distance was $z_{\text{max}} \simeq 113\,\text{mm}$. Within the range z_{max}, the central spot of the Bessel beam propagates without significant spreading (i.e. is non-diffracting).

We inserted a 10$\times$ demagnifying telescope composed of lenses $f_1 = 250\,\text{mm}$ and $f_2 = 25\,\text{mm}$ after the axicon in order to reduce the radius ω_B of the Bessel beam

[1] The value for the Gaussian beam waist ω_0 we cite here is an average of the measurements we took of the beam waist at $\sim$1430 mm from the fiber laser output. For each measurement, we captured an image of the beam with the Sumix 150M camera and fit the data points of a one-dimensional cross-section of the beam to a one-dimensional Gaussian curve.

[2] See Eqs. (2.11) and (2.12), respectively.

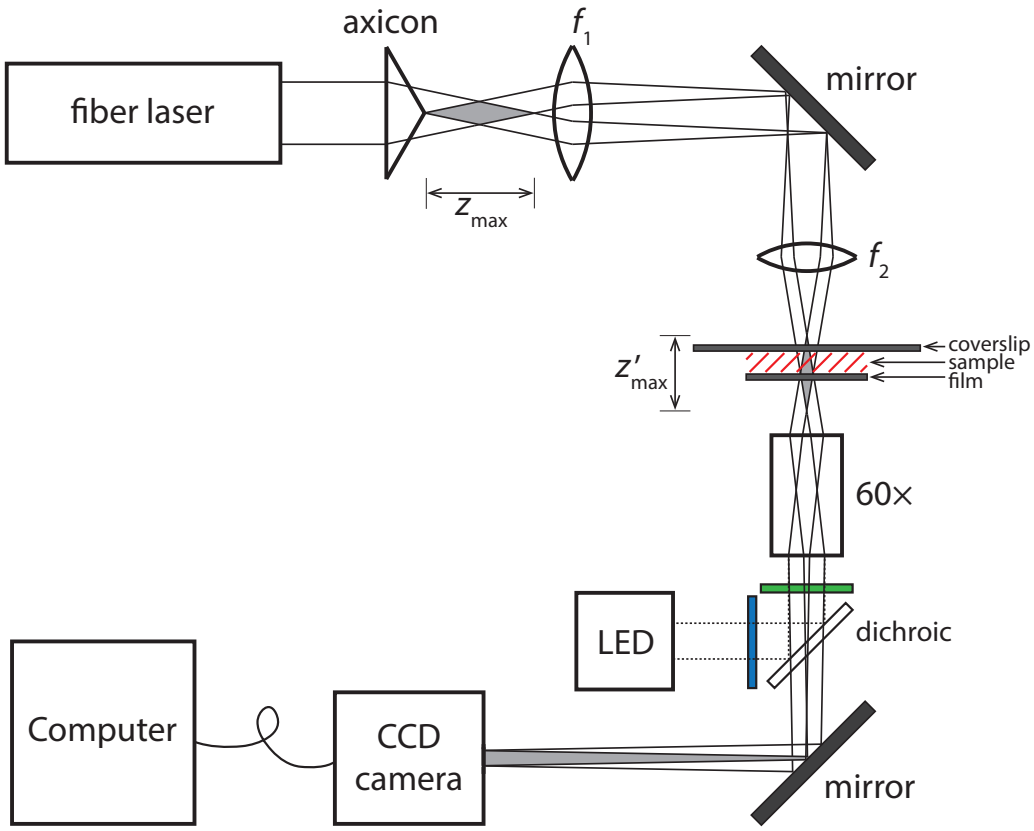

Figure 3.1: Experimental setup of the Bessel beam standing wave trap. A linearly polarized Gaussian beam emitted from a fiber laser ($\lambda = 1064\,\text{nm}$, $P = 3$–$15\,\text{W}$) struck a 25% mirror (not shown) and three ∼100% mirrors (not shown), then illuminated a crown glass axicon ($\gamma = 1^\circ$, $A = 12.7\,\text{mm}$, $n_{\text{ax}} = 1.508$), transforming the incident Gaussian beam ($\omega_0 \simeq 1.0\,\text{mm}$) into a Bessel beam with central maximum radius $\omega_B \simeq 45.9\,\mu\text{m}$ and propagation distance $z_{\text{max}} \simeq 113\,\text{mm}$. A 10× demagnifying telescope composed of lenses $f_1 = 250\,\text{mm}$ and $f_2 = 25\,\text{mm}$ shortened the propagation distance to $z'_{\text{max}} \simeq 1.13\,\text{mm}$. After the telescope, the Bessel beam passed through a sample of fluorescent microspheres immersed in water and struck a reflective film (R $\simeq$ 89%) normal to its surface. The counter-propagating beams produced an optical standing wave above the film. The telescope demagnification and the transfer from air to water reduced the central maximum radius to $\omega'_B \simeq 3.45\,\mu\text{m}$. Blue light ($\lambda = 470\,\text{nm}$) from an LED source passed through an exciter (blue) and reflected off a dichroic (white) oriented at 45° to the propagation axis. Green light emitted by the particles was imaged with a 60× oil immersion objective and a microscope telans lens (not shown). Before reaching the CCD camera, both the emitted green light and the transferred Bessel beam passed through an emitter (green), the dichroic, and two infrared filters (KG1, KG2) (not shown). The camera was connected to a computer where the images were processed with video recording software. Note: The shaded regions of the beam are the areas where the Bessel beam is considered non-diffracting. See Fig. 3.2 for the measured distances between the main optical components.

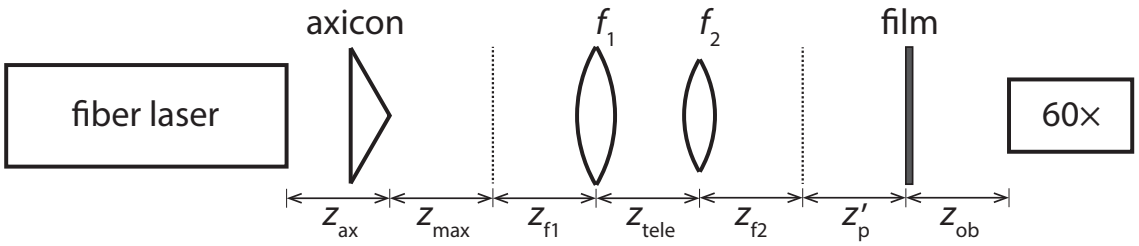

Figure 3.2: Measured distances between the optical elements in our experimental setup of the Bessel beam standing wave trap (see Fig. 3.1): $z_{\rm ax} \approx 1430\,\mathrm{mm}$, $z_{\rm max} = 113\,\mathrm{mm}$, $z_{\rm f1} = 37\,\mathrm{mm}$, $z_{\rm tele} = 290\,\mathrm{mm}$, $z_{\rm f2} = 28\,\mathrm{mm}$, $z'_{\rm p} = 0.113\,\mathrm{mm}$, $z_{\rm ob} = 0.0\,\mathrm{mm}$ + depth of focus of 60× objective. Note: $z'_{\rm p} = z'_{\rm max}/2$.

central maximum by a factor of $\frac{1}{M}$, where $M = 10$ is the angular magnification of the telescope. By reducing the central maximum radius, we effectively increased the magnitudes of the optical forces in the trapping pockets. Moreover, when imaging the beam near the point $z = z_{\rm max}$, the telescope shortened the propagation distance downstream from lens f_2 by a factor of $\frac{1}{M^2}$, such that the theoretical propagation distance $z'_{\rm max}$ after the telescope became[3] $z'_{\rm max} \simeq 1.13\,\mathrm{mm}$. Following the telescope, the Bessel beam passed through a sample of fluorescent microspheres (Applied Biosystems Fluoresbrite® YG[4], monodispersed polystyrene latex) submerged in water ($n = 1.33$). The demagnifying telescope and the air-to-water transfer combined to reduce the central maximum radius to[5] $\omega'_B \simeq 3.45\,\mu\mathrm{m}$.

After passing through the sample, the beam struck a reflective film[6] (total measured reflectivity R = 89% at $\lambda = 1064\,\mathrm{nm}$) normal to its surface. Similar to [23], the superposition of incident and reflected beams produced an optical standing wave in the sample. Since the reflective film only reflected 89% of the incoming radiation,

[3]See Eq. (2.14).

[4]The spheres are yellow-green fluorescent with an excitation maximum of 500 nm and an emission maximum of 560 nm.

[5]See Eq. (2.13).

[6]The reflective film is a thin film of reflective dielectric layers adhered to a microscope cover glass (Thermo Scientific 22 × 22). The layers were manufactured and applied to the glass by Changchun Worldhawk Optoelectronics Co.

the remaining 11% that wasn't canceled out by the reflected radiation generated a non-zero net scattering force $\mathbf{F}_{\text{scat}}$ oriented downstream. As discussed in Section 2.2, the force $\mathbf{F}_{\text{scat}}$ is balanced near each antinode of the standing wave by an upstream axial gradient force $\mathbf{F}_{\text{X}}$ resulting from the axial irradiance gradient $\nabla_{\parallel} I^{\ell}_{\text{sw}}(z)$. In these two-dimensional planes of equilibrium, the microspheres move according to principles of optically-confined Brownian diffusion[7].

To prepare the microspheres for analysis, we diluted the bead sample with double-deionized water until the concentration of beads permitted single particle confinement[8] in each trapping plane. We then injected a small quantity of the sample between a microscope glass coverslip[9] and the reflective film. The sample thickness[10] H was, on average[11], about $100\,\mu$m. The sample was mounted on an Olympus IX71 inverted microscope stage with xy translation and viewed with an infinity corrected $60\times$ oil immersion objective lens (Olympus UPlanSApo, NA=1.35) and a microscope telans lens. We excited the fluorescent beads with 470 nm wavelength light from an LED lamp. The LED light passed through a fluorescence cube with exciter range 460–500 nm and emitter range 515–560 nm. The fluorescence dichroic reflected light below 500 nm ($\text{R} \simeq 99\%$) and transmitted light above 510 nm ($\text{T} \simeq 95\%$). All fluorescence optics were manufactured by Semrock, Inc. Both the emitted light from the spheres and the transferred Bessel beam were imaged with a CCD camera (Point Grey Flea2). To reduce the power of the beam, we inserted two infrared filters (KG2, KG4) between the fluorescence cube and the camera. The signal output of the camera was connected

[7] See Section 2.5.

[8] Single particle trapping typically requires a concentration of about 1–3 particles within the field of view of the camera. In our experiments, we used dilutions ranging from 1:20,000 to 1:300,000 part microsphere to parts water.

[9] Thomas Scientific 24×60.

[10] The distance H was measured from the bottom of the glass coverslip (top boundary) to the top of the reflective film (bottom boundary). The sample was contained within the space between these two boundaries.

[11] Since the sample was not sealed, the fluid volume decreased as the liquid evaporated out the edges.

to a computer where images of the trapped spheres were then processed with digital video recording software (NorPix StreamPix 5.0).

To track the particles, we used the open source software program Video Spot Tracker (VST). With VST, we gathered (x, y) points of the particles' trajectories as a function of time t, where the frame rate of the CCD camera was $\sim$15 fps. We found that the tracking algorithms of the VST program were reliable to use as long as the average displacement of the particles was greater than 40 nm. According to our tracking data, the average displacement of the largest (i.e. slowest) particle we studied was 324 nm. Therefore, we were justified in using VST to collect our data.

3.2 Beam Analysis

For our trapping experiments, we varied the total power P_T of the fiber laser from 3–15 W, which corresponded to 33–175 mW in each trapping plane of the Bessel beam standing wave trap. To deduce the beam power P_{CM} in each trapping plane, we first measured the power P_S in the sample chamber as a function of the total power P_T. To do this, we inserted a power meter (Molectron Max 5200) after lens f_2 and measured the power level for 6 different values of P_T. The linear fit of the 6 data points is shown in Fig. 3.3. Given P_S, we can calculate the central maximum power P_{CM} of the Bessel beam in the sample using

$$P_{CM} \;=\; FP_S, \tag{3.1}$$

where F is the fraction of the total power in the central maximum and, given the number N of rings in the Bessel beam, is determined by [33]

$$F \;\approx\; \frac{1}{1+4N/3}. \tag{3.2}$$

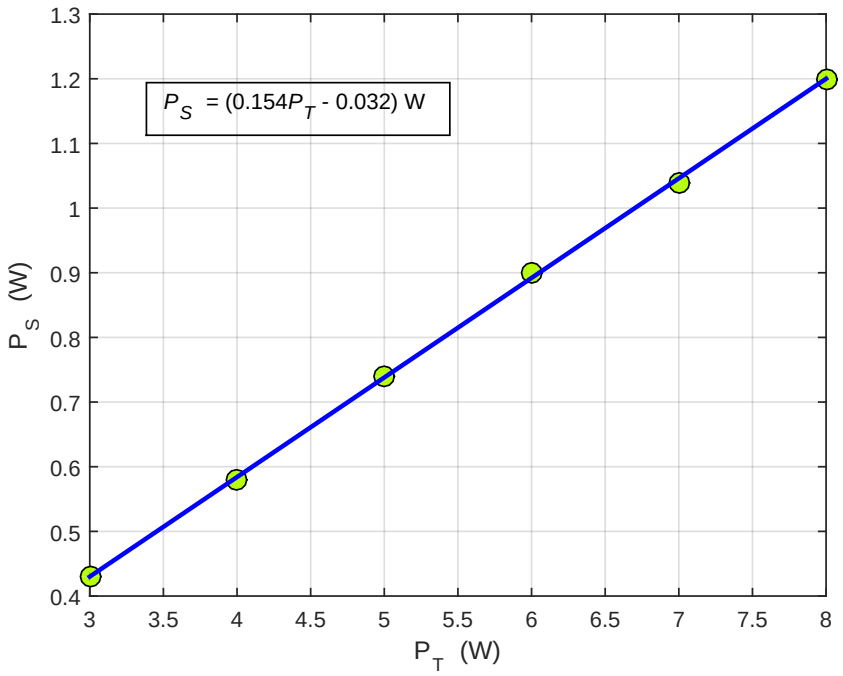

Figure 3.3: Linear fit of the measurements of the beam power P_S in the sample as a function of the total power P_T of the fiber laser.

To estimate the number of rings N in the Bessel beam, we assumed that the aperture size h at the location of the peak irradiance z_{p} was equal to

$$h \;=\; \frac{\omega_0}{2}. \tag{3.3}$$

In k-space, the aperture size becomes

$$h' \;=\; k_r \frac{\omega_0}{2}, \tag{3.4}$$

where h' is used to distinguish the aperture size in dimensionless space ($k_r \times$ real space) from the aperture size h in physical space. Therefore, given $\omega_0 = 1.0\,\mathrm{mm}$, $\lambda = 1064\,\mathrm{nm}$, $n_{\mathrm{ax}} = 1.508$, and $\gamma = 1^\circ$, we get $h' \approx 27.4$. The 9^{th} zero of $J_0(r)$ occurs at $r = 27.49$. Therefore, there are about $N = 9$ rings at the peak irradiance position of our beam.

Using this value for N, we determined that the fraction of power in the central spot was $F = \frac{1}{13}$, which we then used to find P_S and P_{CM}. The power levels P_{CM} that we calculated for each experimental trial are listed in Tables 4.2–4.4 in the following chapter.

For a microsphere with diameter $D = 100\,\text{nm}$ trapped in a Bessel beam standing wave with wavelength $\lambda = 1064\,\text{nm}$, the particle is small enough (i.e. $D \sim \lambda/10\pi$) that we may consider Rayleigh scattering regime formulations to determine rough approximations for the optical forces acting on the particle under various intensities P_{CM}. For example, we found that for a 100 nm diameter particle trapped near the peak irradiance position $z = z'_{\text{p}}$ in the central maximum of the Bessel beam standing wave with $P_{CM} = 118\,\text{mW}$, the total axial force $F_{\parallel}$ and the total transverse force $F_{\perp}$ on the microsphere were approximately

$$F_{\parallel} \;=\; 5.9\,\text{pN}, \tag{3.5}$$

$$F_{\perp} \;=\; 1.18\,\text{pN}. \tag{3.6}$$

In this scenario, we see that $F_{\parallel} \simeq 5F_{\perp}$. Since $F_{\parallel} = |\mathbf{F}_{\text{X}}| + |\mathbf{F}_{\text{scat}}|$ and $F_{\perp} = |\mathbf{F}_{\text{grad}}|$, this result agrees with the qualitative relationship between $|\mathbf{F}_{\text{X}}|$ and $|\mathbf{F}_{\text{grad}}|$ evident in Fig. 2.11, where $|\mathbf{F}_{\text{scat}}|$ was considered to be zero.

Next, we analyzed the laser in our Bessel beam standing wave trap in order to determine experimental values for the peak irradiance position z_{p} and the central maximum radius ω_{B} in two different regions along its path: (1) between the axicon and lens f_1 and (2) after lens f_2. For our experiments, we used the same IPG fiber laser ($\lambda = 1064\,\text{nm}$, $P = 3$–$15\,\text{W}$) and axicon (Del Mar Photonics, $\gamma = 1\,^{\circ}$, $A = 12.7\,\text{mm}$, $n_{\text{ax}} = 1.508$) mentioned in Section 3.1. For the radius ω_0 of the Gaussian beam incident on the axicon, we used our measurement of $\omega_0 \simeq 1.0\,\text{mm}$.

In the first experiment, we placed the axicon ∼1430 mm away from the fiber laser and positioned the imaging chip of the CCD camera (Sumix 150M) 50 mm away from the axicon, which is close to the expected value[12] of $z_{\rm p} = 56.5\,{\rm mm}$ (see Fig. 3.4). Next, we measured the beam irradiance along the z-axis at incremental positions from this starting point: between 50–95 mm, we took 9 measurements every 5 mm, and between 100–170 mm, we took 8 measurements every 10 mm. We then fit our data points to the on-axis field irradiance $I^0(r=0,z)$ of our Bessel beam ($\lambda = 1064\,{\rm nm}$, $P_0 = 3\,{\rm W}$, $\omega_0 = 1.0\,{\rm mm}$, $\gamma = 1\,^\circ$, $z_{\rm max} = 113\,{\rm mm}$), given by[13]

$$I^0(r=0,z) \;=\; \frac{4P_0 k_r \xi(z)}{\omega_0} e^{-2\xi(z)^2} J_0^2(0), \tag{3.7}$$

with $\xi(z)$ defined as $\xi(z) = \frac{z}{z_{\rm max}}$. Here, the power P_0 incident on the axicon is approximately equal to $\frac{P_T}{4}$, since we inserted a 25% reflective mirror after the fiber laser. According to the results of our fit (Fig. 3.5), the experimental peak irradiance position was $z_{\rm p}({\rm exp}) = 70.4\,{\rm mm}$, which agrees fairly well with our theoretical value of $z_{\rm p}({\rm theo}) = 56.5\,{\rm mm}$. The small discrepancy could possibly be accounted for by the measurement errors of $z_{\rm ax}$ and ω_0 after we rearranged the optics on the bench. The beam waist, for example, varied from 0.91 to 1.24 mm. Thus, had we used $\omega_0 = 1.24\,{\rm mm}$ instead of $\omega_0 = 1.0\,{\rm mm}$, our theoretical value for the location of the peak irradiance in Region 1 would be $z_{\rm p} = 70\,{\rm mm}$, which agrees almost exactly with our experimental fitted value. Next, to find an experimental value for $\omega_{\rm B}$, we captured an image of the Bessel beam central maximum irradiance at $z = z_{\rm p}({\rm exp})$ and fit the data points of its two-dimensional cross-section to the lateral field irradiance $I^0(r, z = \frac{z_{\rm max}}{2})$ of our Bessel beam, given by[14]

[12] For our Bessel beam, $z_{\rm p} = \frac{z_{\rm max}}{2} = \frac{113\,{\rm mm}}{2} = 56.5\,{\rm mm}$.

[13] See Eq. (2.8).

[14] See Eq. (2.8).

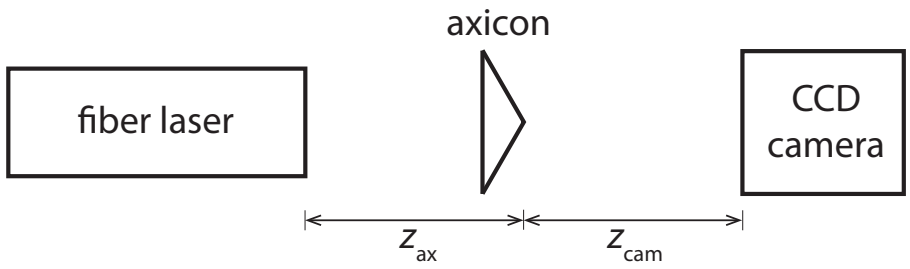

Figure 3.4: Measured distances between the optical components in our experiment to determine the peak irradiance position z_p and the central maximum radius ω_B in the region between the axicon and lens f_1 (not shown): $z_{ax} \approx 1430\,\text{mm}$, $z_{cam} = 50\text{–}170\,\text{mm}$. The specifications for the fiber laser and the axicon are identical to those detailed in Fig. 3.1

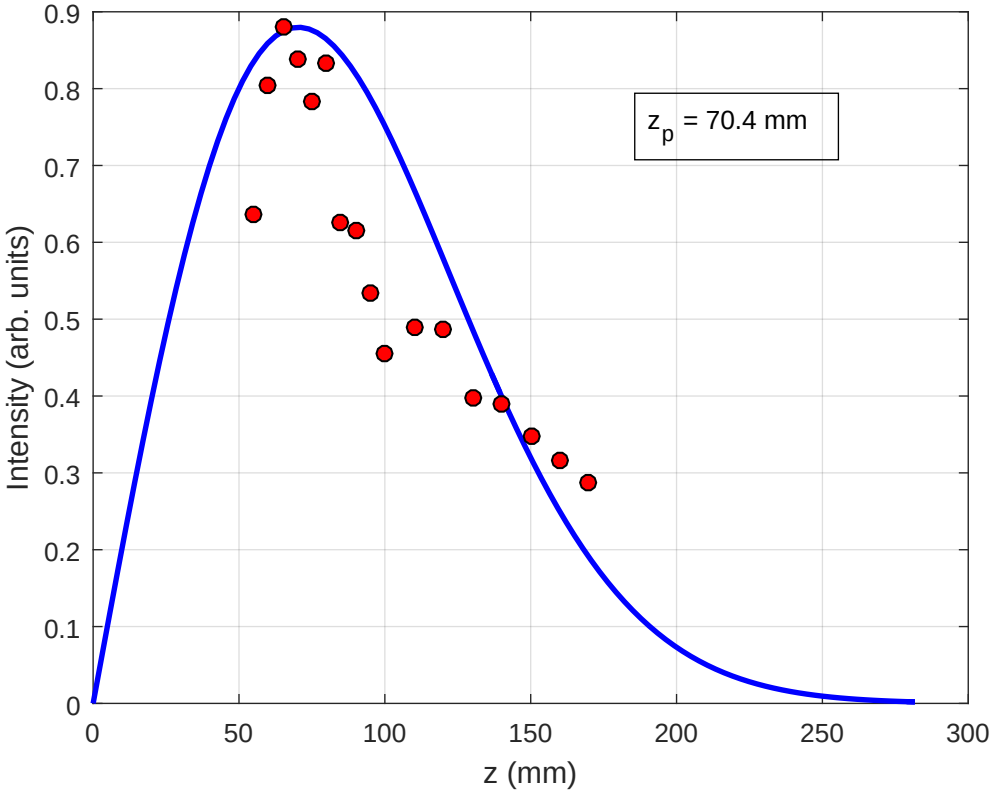

Figure 3.5: Fit of the experimental data points of the on-axis irradiance to the theoretical curve $I^0(r=0,z)$ in the region between the axicon and lens f_1. As shown, the experimental value of the peak irradiance position is $z_p = 70.4\,\text{mm}$.

$$I^0(r, z = \frac{z_{\max}}{2}) \;=\; \frac{2P_0 k_x}{\omega_0} e^{-1/2} J_0^2(k_x x). \tag{3.8}$$

The fit of the data points to Eq. (3.8) produced an experimental value of $\omega_{\mathrm{B}}(\mathrm{exp}) = 34.0\,\mu\mathrm{m}$, which is fairly close to the theoretical value of $\omega_{\mathrm{B}}(\mathrm{theo}) = 45.9\,\mu\mathrm{m}$. Considering the modest error in the experimental location of the peak irradiance above, a minor difference in the central maximum radius is expected.

In our second experiment, we added the $10\times$ demagnifying telescope in order to find values for the peak irradiance position and the central maximum radius between lens f_2 and the sample chamber. The distances between the optical elements in this experiment are indicated in Fig. 3.6. Using two lens imaging, we found that for an object distance of $z_{\mathrm{f1}} = (150 - 113)\,\mathrm{mm} = 37\,\mathrm{mm}$, we get an image distance of $z_{\mathrm{f2}} \approx 28\,\mathrm{mm}$. Then, positioning the focal point of the $20\times$ objective lens at a distance of 28.0 mm from lens f_2, we took 34 measurements of the beam irradiance along the z-axis, going from 28.0 mm to 28.52 mm every 0.02 mm. Similar to the first experiment performed in Region 1, we then fit our data points to the on-axis field irradiance $I^0(r = 0, z)$ of our Bessel beam.

According to the results of our fit (Fig. 3.7), the experimental peak irradiance occurred at $z_{\mathrm{p}}(\mathrm{exp}) = 0.113\,\mathrm{mm}$, which is off by a factor of 5 from the theoretical value of $z_{\mathrm{theo}} = 0.565\,\mathrm{mm}$. Using lens formulas to deduce the actual theoretical location of the peak irradiance, we got $z_{\mathrm{p}}(\mathrm{theo}) = 0.50\,\mathrm{mm}$, which is slightly closer to our experimental value. Morever, since the telescope reduces the value of $z_{\mathrm{p}}(\mathrm{theo})$ by approximately $\frac{1}{M^2}$, the result for $z_{\mathrm{p}}(\mathrm{theo})$ is highly sensitive to the magnification M of the demagnifying telescope. Thus, any amount of measurement error in the distances between the optical components in our experiment could, in principle, alter our expected value for the peak irradiance position significantly. Therefore, in this sense, our experimental result for the location of the peak irradiance isn't entirely

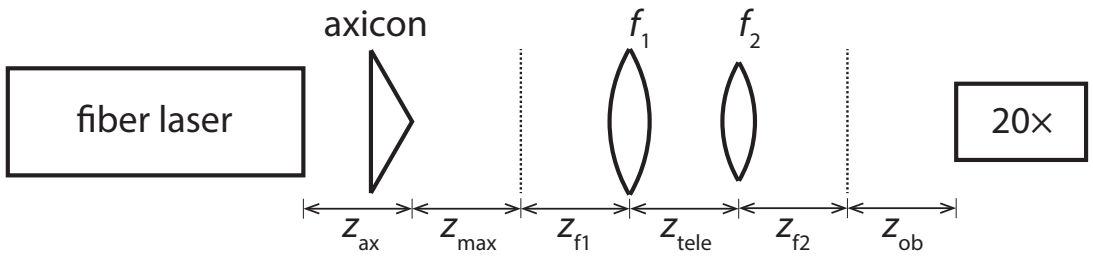

Figure 3.6: Measured distances between the optical elements in our experiment to determine the peak irradiance position and the central maximum radius in the region between lens f_2 and the sample chamber (not shown): $z_{\rm ax} \approx 1430\,\text{mm}$, $z_{\rm max} = 113\,\text{mm}$, $z_{\rm f1} = 37\,\text{mm}$, $z_{\rm tele} = 290\,\text{mm}$, $z_{\rm f2} = 28\,\text{mm}$, $z_{\rm ob} = 0.00$–$0.52\,\text{mm}$ + depth of focus of $20\times$ objective. The specifications for the fiber laser, the axicon, and lenses f_1 and f_2 are identical to those outlined in Fig. 3.1.

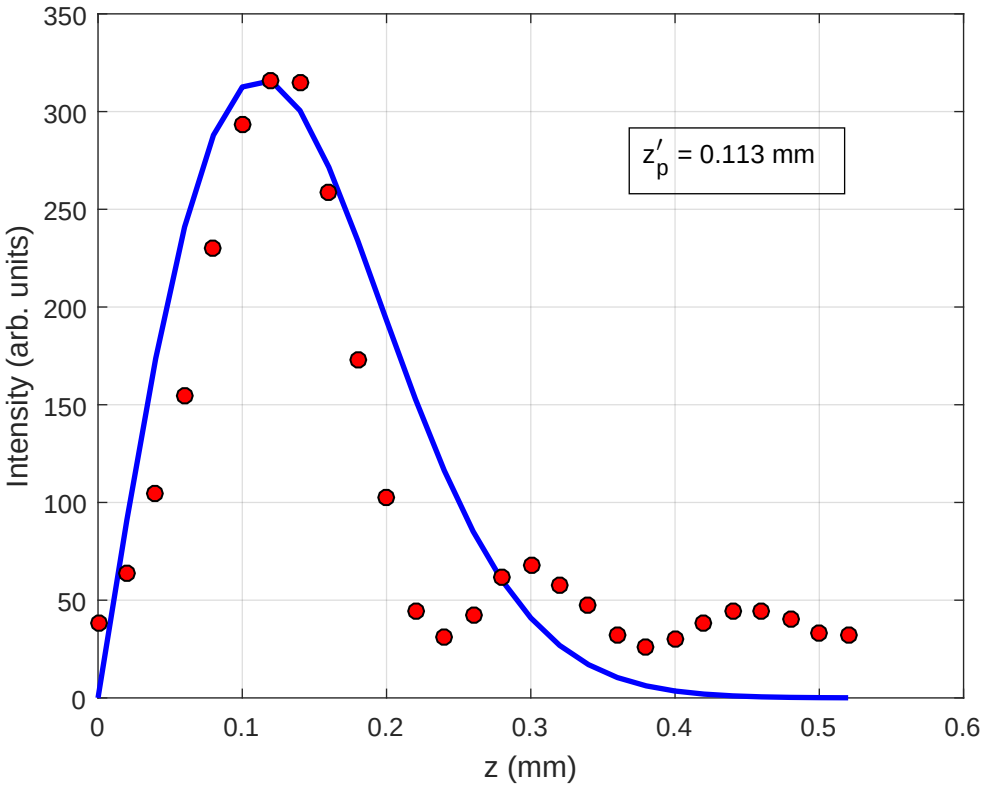

Figure 3.7: Fit of the experimental data points of the on-axis irradiance to the theoretical curve $I^0(r=0,z)$ in the region between lens f_2 and the sample chamber. As depicted, the experimental value of the peak irradiance position is $z'_{\rm p} = 0.113\,\text{mm}$.

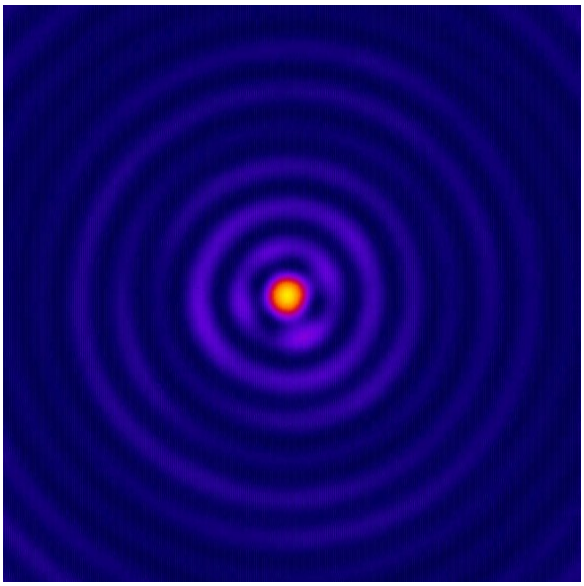

Figure 3.8: Cross-sectional image of the Bessel beam near the peak irradiance position in Region 2. To obtain this image, we used the 20× objective and the Sumix CCD camera. The frame size is 585×585 pixels where 1 pixel $= 335$ nm.

unexpected.

Even though there is some discrepancy in the numerical value for the location of the peak irradiance in Region 2, the characteristic shape of our beam does closely match the theoretical shape given by $I^0(r=0,z)$. Additionally, the small peaks in the right half of the graph may have arisen from the interference of the Bessel beam with the diffracted light from the curved axicon tip. Brzobohaty et al. [46] showed that for an axicon with an oblate tip, the on-axis beam irradiance experiences periodic modulations which have a spatial period X given by

$$\mathrm{X} \;=\; \frac{\lambda}{1-\cos(\theta)} \;\simeq\; \frac{\lambda}{1-\cos[(n_{\mathrm{ax}}-1)\gamma]}, \tag{3.9}$$

where λ is the laser wavelength, θ is the half angle of the conical surface of the Bessel beam, n_{ax} is the refractive index of the axicon, and γ is the opening angle of the axicon. Inserting our experimental values for the axicon and the laser into Eq. (3.9), we found

Table 3.1: Comparison of the experimental and theoretical values for the peak irradiance location $z_{\rm p}$ and the central maximum radius $\omega_{\rm B}$ in two distinct regions of the laser path: (1) between the axicon and lens f_1 and (2) after lens f_2.

Region	$z_{\rm p}$(exp) (mm)	$z_{\rm p}$(theo) (mm)	$\omega_{\rm B}$(exp) (μm)	$\omega_{\rm B}$(theo) (μm)
1	70.4	56.5	34.0	45.9
2	0.113	0.565	3.80	4.59

that the period of the irradiance modulations predicted by [46] was X = 271 μm. In Fig. 3.7, the smaller peaks on the right side of the graph have a periodicity of $\sim$150 μm, which agrees fairly well with the value calculated using Eq. (3.9). Therefore, this result suggests that the small peaks in our data could have arisen from the interference of our Bessel beam with the diffracted light from the curved tip of our axicon. Finally, we captured an image (see Fig. 3.8) of the Bessel beam near the peak irradiance position and fit the data points of its cross-section to Eq. (3.8). We got an experimental value of $\omega_{\rm B}(\text{exp}) = 3.80\,\mu$m for the central maximum radius, which is moderately close to the theoretical value[15] of $\omega_{\rm B}(\text{theo}) = 4.59\,\mu$m. The measured results and theoretical values for the peak irradiance position and the central maximum radius in the two different regions of the optical path are summarized in Table 3.1.

In Chapter 4, we first discuss the imaging data we collected to demonstrate simultaneous, multi-level particle confinement in our Bessel beam standing wave trap. Next, we use our particle tracking data to calculate the mean-square displacement $\rho(\tau)$ for finite trajectories of the microspheres in the Bessel beam standing wave, then fit the resulting points of $\rho(\tau)$ to Eqs. (2.44) and (2.45) to extract[16] experimental values for $D_{\rm msd}$ and $D'_{\rm msd}$. Finally, we compare our results with the expected values $D_{\rm theo}$ given by the Stokes-Einstein-Sutherland equation.

[15] Since the beam passed through a 10$\times$ demagnifying telescope, the predicted value for $\omega_{\rm B}$ in Region 2 is equal to one-tenth the value of $\omega_{\rm B}$ in Region 1, i.e. $\frac{45.9}{10} = 4.59$.

[16] As discussed in Section 2.5, we get $D'_{\rm msd}$ by correcting $D'_{\rm m}$ for the exposure time of the camera.

Chapter 4: Results

4.1 Multi-level Particle Confinement

We observed simultaneous particle confinement at multiple vertical heights in the Bessel beam standing wave trap. In our experiments, we successfully trapped fluorescent, polystyrene spheres with diameters 100, 200, and 300 nm in the standing wave trapping planes of the Bessel beam central maximum. The heights of the trapping planes ranged from 5 to 56 μm from the reflective surface of the sample chamber (see Tables 4.2–4.4). This range of heights corresponds to antinode levels 13–140. Thus, the requirement of Eq. (2.33) was easily satisfied[1]. Therefore, surface forces acting on the trapped particles can be ignored for our diffusion analysis in Section 4.2.

In Section 2.1, we determined that a particle with radius $r_{\text{ob}} = 150\,\text{nm}$, or diameter 300 nm, confined at the center of a trapping plane in our Bessel beam standing wave trap casts a shadow of length[2] $l_s = 1.68\,\mu$m downstream from its position. If the beam is immersed in water ($n = 1.33$), then the next available trapping plane occurs at the 5^{th} antinode from the particle, or $2.0\,\mu$m downstream. This result served as a good approximation for a diffusing microparticle in our Bessel beam standing wave trap. For example, the smallest separation of simultaneously trapped 300 nm particles that we observed was $3.0\,\mu$m, which agrees well with this result.

The theoretical lattice period of our Bessel beam standing wave trap was $d_{\text{theo}} = 0.4\,\mu$m. To determine the experimental lattice period d_{exp}, we adhered several fluo-

[1] Equation (2.33) states that, for a spherical particle with diameter $D = 300\,\text{nm}$ trapped in a Bessel beam standing wave with wavelength $\lambda = 1064\,\text{nm}$, the m^{th} antinode from the surface must have a value of $m \geq 4$ in order for surface effects to be neglible, where the value of $m = 4$ corresponds to the 5^{th} antinode from the reflective surface. Since the 300 nm particle was the largest sphere we tested, the condition $m \geq 4$ satisfies the requirement from [52] for all three particle sizes.

[2] See Eq. (2.17).

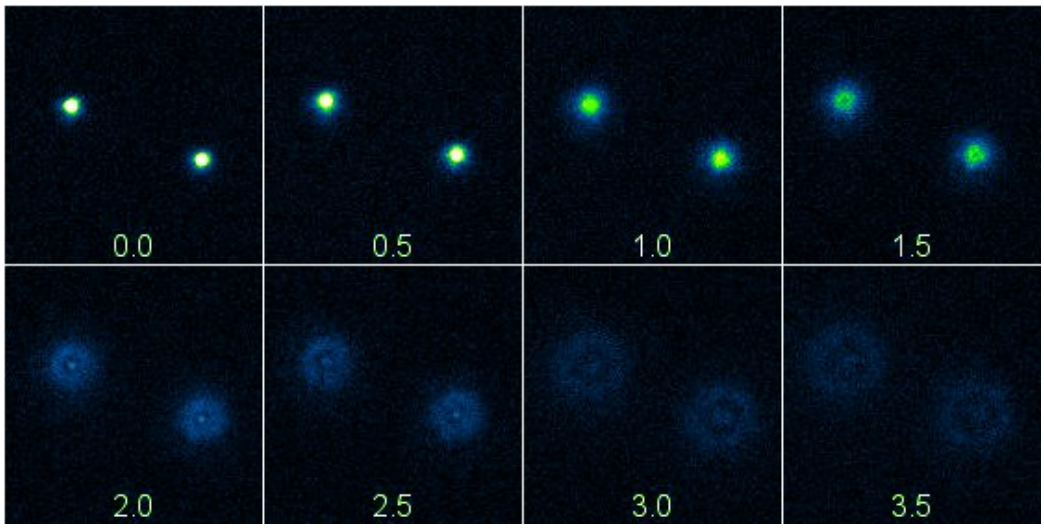

Figure 4.1: Image montage of two 300 nm diameter fluorescent spheres adhered to a glass surface. In the top left image, the 60× imaging objective was focused on the sample surface. Then, going right and down across the montage, the objective moved away from the sample surface in 0.5 μm increments per frame. The vertical heights h_m (measured in microns) of the imaging objective from the static surface are indicated in each frame, starting at $h = 0.0\,\mu$m. Each frame is 140×140 pixels where 1 pixel = 123 nm.

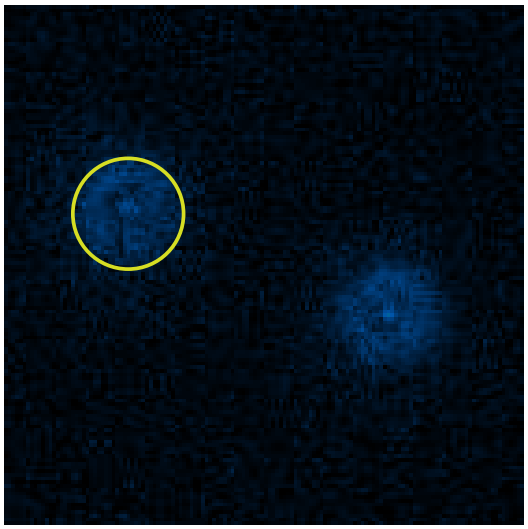

Figure 4.2: Depiction of the technique we used to measure the static diffraction diameters D_N. To find the diameter of a diffraction pattern, we opened the image file in ImageJ and drew a circle near the outer edge of the diffraction pattern. We then used a function in ImageJ to calculate the diameter of the circle. The frame in this figure is 140×140 pixels where 1 pixel = 123 nm.

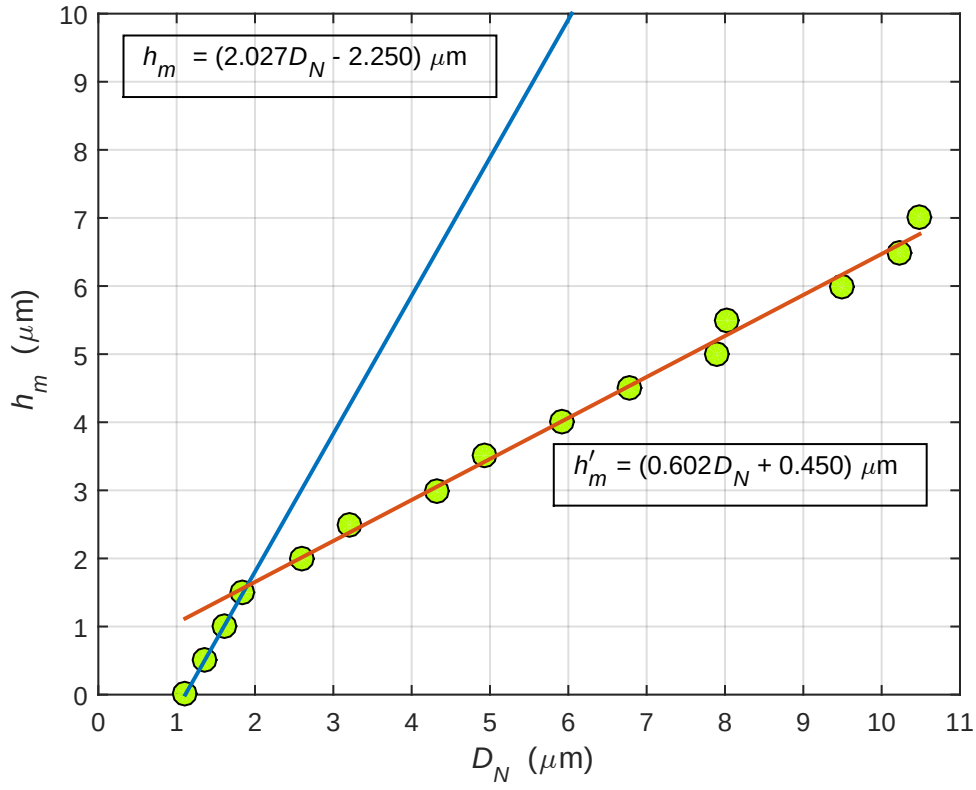

Figure 4.3: Plot of the vertical heights h_m of the 60× imaging objective from the reflective surface as a function of the static diffraction diameters $D_{\rm N}$ described in Figs. 4.1 and 4.2. The two fits for each distinct region of the plot were used to deduce the vertical heights h_m of a 300 nm particle jumping down successive trapping levels in the Bessel beam standing wave. Specifically, we used the linear fit, $h_m = (2.027D_N - 2.250)\,\mu$m, of the first four points to determine the h_m values of the dynamic particle for the first four levels of its motion. Next, we used the linear fit, $h'_m = (0.602D_N + 0.450)\,\mu$m, of points 4–15 to find the heights h_m of the last four levels of its trajectory. See Fig. 4.4 and Table 4.1 for further discussion of the dynamic particle.

rescent 300 nm diameter particles to the surface of a glass coverslip and then imaged the static beads with a 60× oil immersion microscope objective at 0.5 μm incremental displacements of the objective, as shown in Fig. 4.1. As the objective lens moved away from the stationary sample surface, the light emitted from the fluorescent microspheres produced diffraction patterns as it entered the objective. To measure the diameters $D_{\rm N}$ of the static diffraction patterns, we drew a circle near the outermost ring of the diffraction pattern using ImageJ, as depicted in Fig. 4.2. After we drew the circle, we

Table 4.1: Measurements of the diameters D_{N} of the dynamic diffraction patterns of a 300 nm diameter sphere trapped in the Bessel beam standing wave (see Fig. 4.4), the extrapolated vertical heights h_m of the trapped particle, the corresponding experimental lattice period values d_{exp}, and the comparative ratios $d_{\mathrm{exp}}/d_{\mathrm{theo}}$. To measure D_{N}, we used the technique described in Fig. 4.2. The vertical heights h_m for levels 1–4 were deduced using the first fit from Fig. 4.3, $h_m = (2.027 D_{\mathrm{N}} - 2.250)\,\mu$m, and the h_m values for levels 5–8 were determined using the second fit, $h'_m = (0.602 D_{\mathrm{N}} + 0.450)\,\mu$m. The experimental lattice period values d_{exp} were then calculated by finding the difference between the vertical heights of two successive levels. Our average experimental lattice period was 0.526 μm, which is 32% greater than the theoretical lattice period, $d_{\mathrm{theo}} = 0.4\,\mu$m. The small difference could be due to measurement error.

Level	D_{N} (μm)	h_m (μm)	d_{exp} (μm)	$d_{\mathrm{exp}}/d_{\mathrm{theo}}$
1	1.24	0.26	N/A	N/A
2	1.63	1.05	0.791	1.98
3	1.74	1.27	0.223	0.55
4	2.01	1.82	0.547	1.37
5	2.95	2.22	0.402	1.01
6	4.08	2.90	0.680	1.70
7	4.95	3.43	0.524	1.31
8	5.81	3.94	0.518	1.29
$\bar{\mathbf{x}}$	N/A	N/A	**0.526**	**1.32**
σ	N/A	N/A	**0.183**	**0.46**

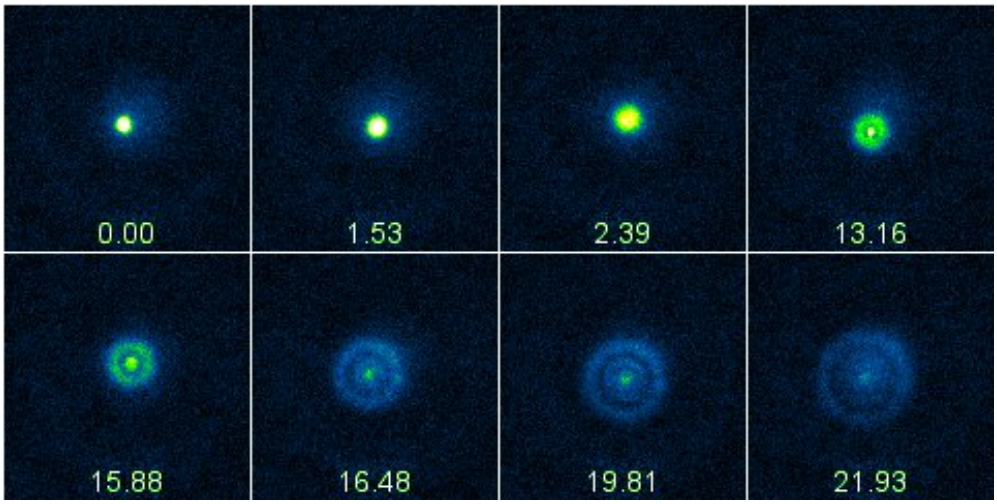

Figure 4.4: Image montage of a dynamic 300 nm diameter microsphere at 8 distinct vertical heights in the Bessel beam standing wave. Starting from the top left image and moving right, the particle drops vertically toward the reflective surface while the imaging objective remains fixed. At each antinode level, the particle moves according to confined Brownian diffusion. The time (in seconds) when each image was captured is indicated in each frame, starting at $t = 0.00$ s. Each frame is 120×120 pixels where 1 pixel = 123 nm. See Table 4.1 for further analysis of the particle's motion.

utilized an algorithm in ImageJ to calculate the diameter of the circle. This data was then used to create a plot of the vertical heights h_m of the imaging objective from the reflective surface as a function of the static diffraction diameters D_{N}, as shown in Fig. 4.3. Noticing a clear difference in slope starting at the fourth point, we made two linear fits of the points for each distinct region of the plot.

The two linear fits shown in Fig. 4.3 were used to deduce the experimental periodic spacing d_{exp} of the vertical jumps of a dynamic microsphere trapped in the Bessel beam standing wave. Specifically, we used ImageJ to measure the diffraction diameters of a 300 nm particle at 8 distinct heights in the standing wave, including the starting position, and then used the fitted lines from Fig. 4.3 to extrapolate the vertical heights h_m of the moving particle. A montage of the images captured at each vertical height is provided in Fig. 4.4. For our height measurments, we kept the observation focal plane constant so that the dynamic sphere moved out of focus as it dropped toward the sample surface. From there, we deduced the vertical displacements, or lattice period d_{exp}, of each jump. As shown in Table 4.1, we calculated an average experimental lattice period of $0.526\,\mu$m, which is 32% greater than the theoretical lattice period, $d_{\mathrm{theo}} = 0.4\,\mu$m. The minor discrepancy could be accounted for by the error inherent in our technique for measuring the diameters D_{N} in ImageJ. That is, since the exact location of the outer edge of a diffraction pattern was diffucult to determine with the analytical tools available in ImageJ, some noticeable inaccuracies and inconsistencies were anticipated. To improve our measurements of the diameters D_{N}, we could (1) use a camera with higher pixel count and (2) implement a more rigorous mathematical technique for determining the precise location of the outer edge of each diffraction pattern.

Finally, in the Bessel beam standing wave trap, we observed preferential movement of the particles toward the reflective surface. This observation is expected because the

scattering force $\mathbf{F}_{\text{scat}}$ in our setup[3] is non-zero at all points along the propagation axis of the standing wave and points toward the reflective surface at all times. Therefore, the scattering force overpowers the upward axial gradient force $\mathbf{F}_{\text{X}}$ whenever the particles are pushed by Brownian forces to the nodes residing below the trapping planes. At the nodes, the axial gradient force goes to zero but the scattering force remains non-zero. Thus, the unbalanced net downward force at the standing wave nodes causes the particles to favor jumps downward over jumps upward.

4.2 Diffusion Analysis

We used Video Spot Tracker to collect tracking data of the transverse particle diffusion of individual fluorescent microparticles in the Bessel beam standing wave trap. In our experiments, we tested spheres with diameters of 100, 200, and 300 nm. In Figs. 4.5, 4.7, and 4.9, we display a montage of images of one of the trials from each data set. Specifically, in Fig. 4.5, we show a series of images of the 100 nm diameter particle corresponding to Trial 9 in Table 4.2; in Fig. 4.7, we display images for the 200 nm diameter particle corresponding to Trial 7 in Table 4.3; and, in Fig. 4.9, we show images for the 300 nm diameter particle coinciding with Trial 6 in Table 4.4. Each montage displays every 10^{th} frame from a selection of 100 images from the video, where the video frame rate was 14.8–15 fps. A plot of the superposition of locations for the complete video sets of each of these three particles is shown in Figs. 4.6, 4.8, and 4.10. To center the plots on the origin, we subtracted the mean value of the x and y data from each individual data point.

In Tables 4.2–4.4, we list values for the total laser power P_T emitted from the fiber laser, the power P_{CM} present in the Bessel beam central maximum, the vertical heights h_m from the reflective surface, the horizontal displacement $\Delta x_{.95}$, the vertical

[3] In our experimental setup, the reflection coefficient of the reflective surface was R = 0.89. Therefore, the incident beam retained a net downward scattering force.

displacement $\Delta y_{.95}$, and the total video frame count for each of the trials we performed for each of the particle sizes. To calculate $\Delta x_{.95}$, we took the absolute value of the horizontal displacements from the origin, and then found the displacement that contained 95% of the points. We performed a similar calculation to find $\Delta y_{.95}$. We then used our results for $\Delta x_{.95}$ and $\Delta y_{.95}$ to sketch diffusion domains for each of the experimental trials corresponding to each particle size. These drawings are shown in Figs. 4.11–4.13.

Next, we sought to verify the results of Mu et al. [22], which are summarized in Eqs. (1.1) and (1.2). In Section 2.3, we used Eq. (1.1) to determine that the axial gradient force $\mathbf{F}_{\mathrm{X}}$ reaches a theoretical maximum value for $D_{\max} = 286\,\mathrm{nm}$; then, we used Eq. (1.2) to find that $\mathbf{F}_{\mathrm{X}}$ reaches a theoretical minimum value for $D_{\min} = 570\,\mathrm{nm}$. To test Eq. (1.1), we calculated the averages of the video frame counts for the 100, 200, 300 nm diameter spheres in order to determine which trapped particle was the most stable. We found that the averages were approximately the same. Upon close inspection of Fig. 3 in [22], we found that the axial gradient force $\mathbf{F}_{\mathrm{X}}$ should actually be about the same for all three particle sizes. Thus, our experimental data seems to agree with Eq. (1.1). Next, to test Eq. (1.2), we attempted to trap fluorescent, polystyrene spheres with diameters of $D = 500\,\mathrm{nm}$. In every trial, the particles accelerated from their positions in the sample toward the reflective surface once they entered the central spot of the Bessel beam standing wave. Since Mu et al. predicted that the axial gradient force $\mathbf{F}_{\mathrm{X}}$ should be nearly zero for a particle with diameter $D \approx 500\,\mathrm{nm}$, then our observations are expected. That is, if the upward axial gradient force is zero, then the downward axial scattering force $\mathbf{F}_{\mathrm{scat}}$ becomes the dominant force. Therefore, the unbalanced downward force in the Bessel beam standing wave should accelerate the microspheres to the bottom surface, as we observed.

We now present our results for the confined diffusion coefficients D'_{msd} for each of the

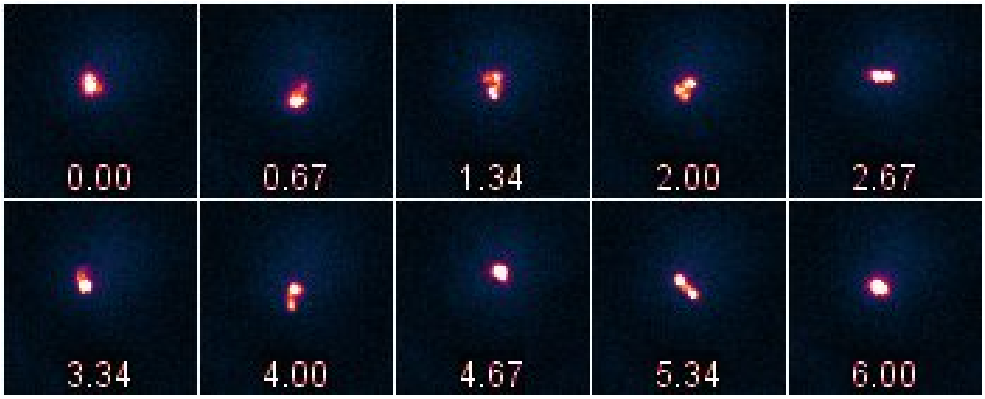

Figure 4.5: A series of images depicting the Brownian motion of a 100 nm diameter sphere moving along a trapping plane of the Bessel beam standing wave containing 175 mW of power and positioned at a height of 28 μm from the reflective surface (see Trial 9 in Table 4.2). The series displays every 10^{th} frame from a selection of 100 frames in the data set. The time (in seconds) when each image was captured is indicated in each frame, starting at $t = 0.00$ s (top left image). Note: The dimensions of each frame are 70×70 pixels where 1 pixel = 123 nm.

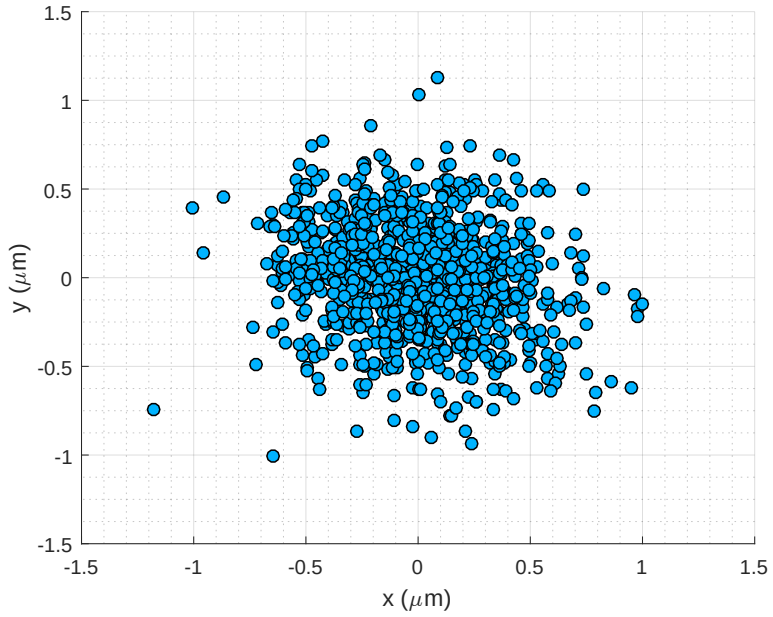

Figure 4.6: Superposition of tracked positions for a 100 nm diameter sphere moving along a trapping plane of the Bessel beam standing wave that contains 175 mW of beam power and is located at a height of 28 μm from the reflective surface. In this graph, we display every frame in the data set, which comprises 1100 data points. See Trial 9 in Table 4.2.

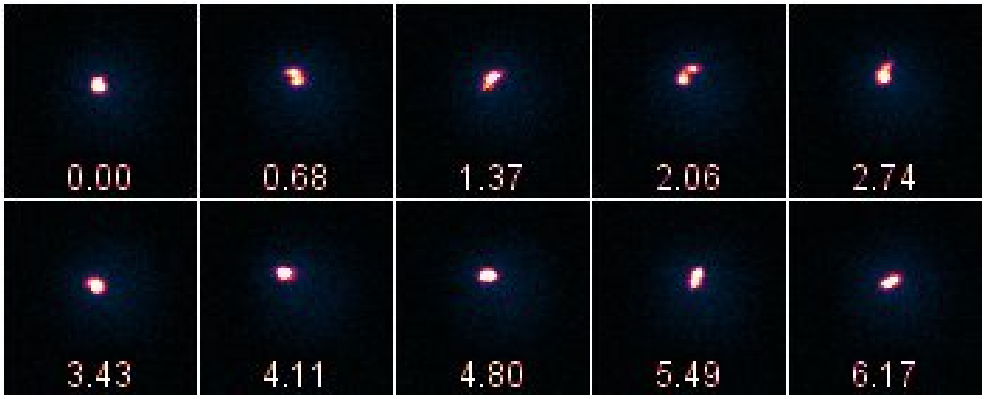

Figure 4.7: A series of images depicting the Brownian motion of a 200 nm diameter sphere moving along a trapping plane of the Bessel beam standing wave containing 92 mW of power and positioned at a height of 11 μm from the reflective surface (see Trial 7 in Table 4.3). The series displays every 10^{th} frame from a selection of 100 frames in the data set. The time (in seconds) when each image was captured is indicated in each frame, starting at $t = 0.00$ s (top left image). Note: The dimensions of each frame are 70×70 pixels where 1 pixel = 123 nm.

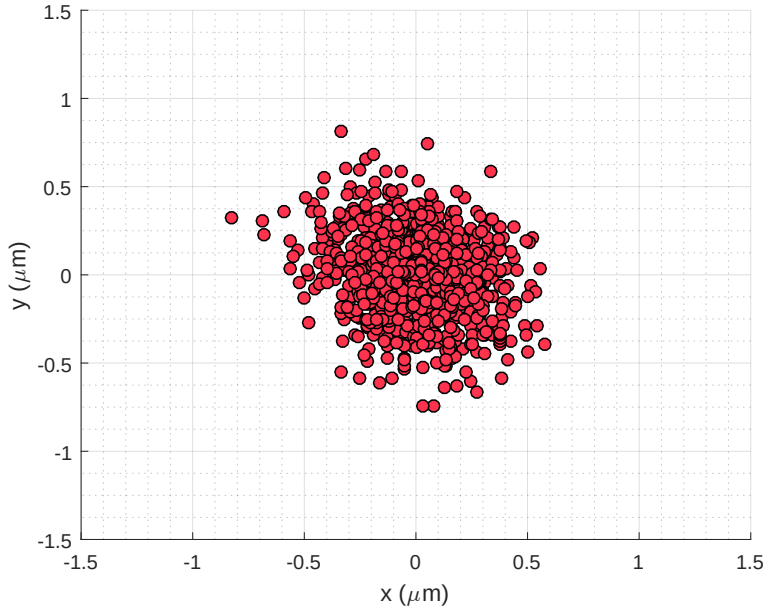

Figure 4.8: Superposition of tracked positions for a 200 nm diameter sphere moving along a trapping plane of the Bessel beam standing wave that contains 92 mW of beam power and is located at a height of 11 μm from the reflective surface. In this graph, we display every frame in the data set, which consists of 995 data points. See Trial 7 in Table 4.3.

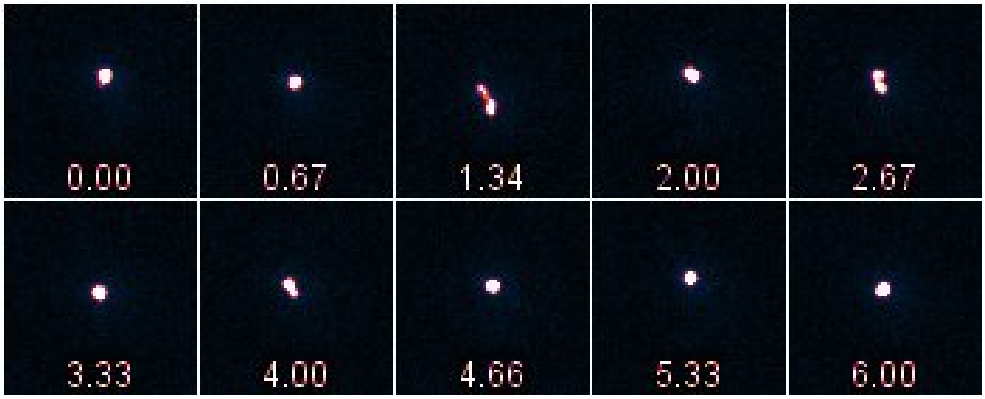

Figure 4.9: A series of images depicting the Brownian motion of a 300 nm diameter sphere moving along a trapping plane of the Bessel beam standing wave containing 69 mW of power and positioned at a height of 8 μm from the reflective surface (see Trial 6 in Table 4.4). The series displays every 10^{th} frame from a selection of 100 frames in the data set. The time (in seconds) when each image was captured is indicated in each frame, starting at $t = 0.00$ s (top left image). Each frame is 70×70 pixels where 1 pixel = 123 nm.

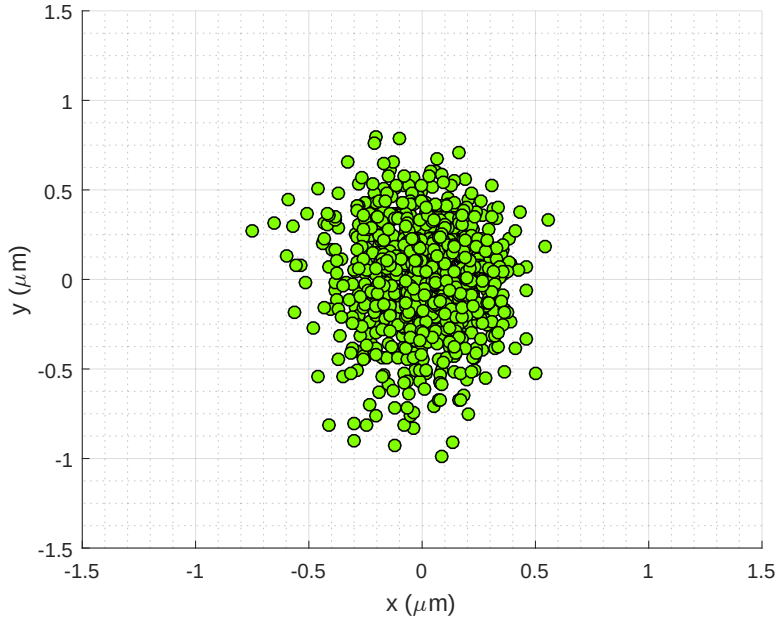

Figure 4.10: Superposition of tracked positions for a 300 nm diameter sphere moving along a trapping plane of the Bessel beam standing wave that contains 69 mW of beam power and is located at a height of 8 μm from the reflective surface. In this graph, we display every frame in the data set, which comprises 1009 data points. See Trial 6 in Table 4.4.

Table 4.2: Tracking data for 100 nm diameter particles.

Trial	P_T (W)	P_{CM} (mW)	h_m (μm)	$\Delta x_{.95}$ (μm)	$\Delta y_{.95}$ (μm)	Frame Count
1	5	57	9	0.50	0.48	473
2	6	69	9	0.43	0.52	2310
3	6	69	13	0.85	2.04	118
4	6	69	23	1.38	1.76	98
5	8	92	27	0.89	1.04	764
6	12	140	19	0.56	0.61	1690
7	12	140	20	0.73	0.71	639
8	12	140	26	0.59	0.60	1290
9	15	175	28	0.60	0.59	1100

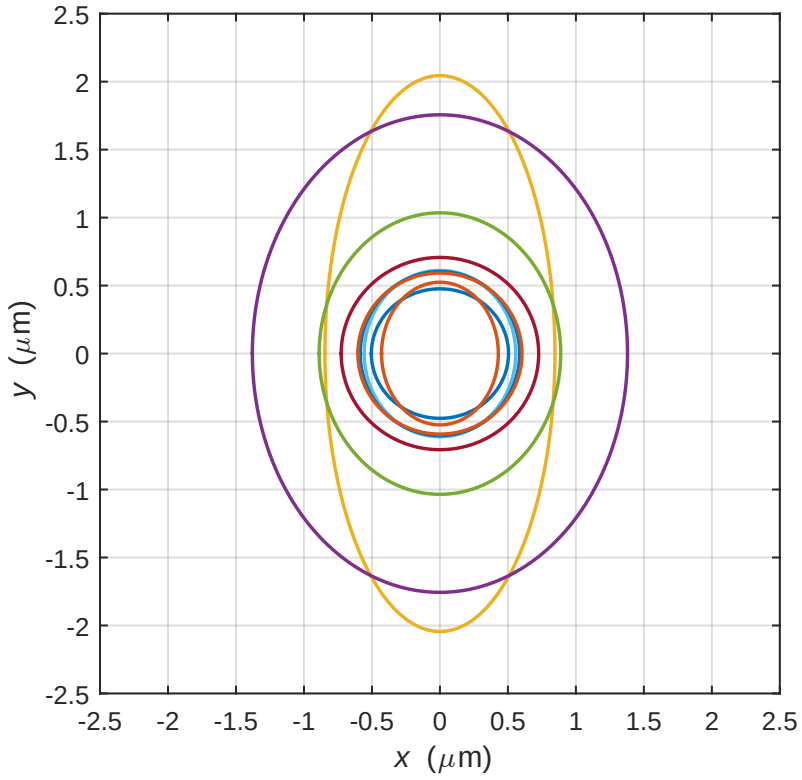

Figure 4.11: Graph of the diffusion domains of the 100 nm diameter trapped spheres corresponding to each trial shown in Table 4.2. The horizontal and vertical arms of each ellipse are given by $\Delta x_{.95}$ and $\Delta y_{.95}$, respectively.

Table 4.3: Tracking data for the 200 nm diameter particles.

Trial	P_T (W)	P_{CM} (mW)	h_m (μm)	$\Delta x_{.95}$ (μm)	$\Delta y_{.95}$ (μm)	Frame Count
1	5	57	5	0.33	0.60	185
2	5	57	6	0.62	0.81	1853
3	5	57	7	1.13	1.33	130
4	6	69	6	0.60	0.70	370
5	6	69	6	1.31	1.48	162
6	7	80	35	0.58	0.73	192
7	8	92	11	0.41	0.46	995
8	8	92	15	0.65	0.71	382
9	8	92	15	1.54	1.17	278
10	12	140	9	0.84	0.75	94
11	12	140	12	0.54	0.46	92
12	15	175	20	0.61	0.34	128
13	15	175	20	0.98	0.50	811

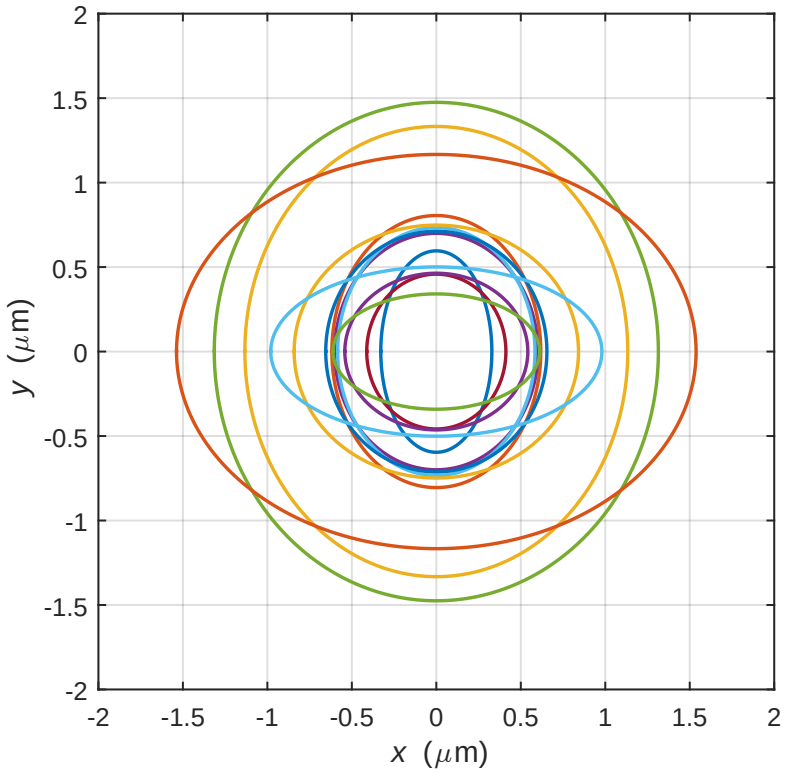

Figure 4.12: Graph of the diffusion domains of the 200 nm diameter trapped spheres corresponding to each trial shown in Table 4.3. The horizontal and vertical arms of each ellipse are given by $\Delta x_{.95}$ and $\Delta y_{.95}$, respectively.

Table 4.4: Tracking data for the 300 nm diameter particles.

Trial	P_T (W)	P_{CM} (mW)	h_m (μm)	$\Delta x_{.95}$ (μm)	$\Delta y_{.95}$ (μm)	Frame Count
1	3	33	6	1.47	1.08	266
2	5	57	6	0.87	0.71	365
3	5	57	8	0.51	0.40	835
4	6	69	6	0.63	0.62	332
5	6	69	6	0.72	0.57	843
6	6	69	8	0.37	0.57	1009
7	6	69	20	0.69	0.59	588
8	6	69	28	0.65	0.67	751
9	6	69	56	0.73	0.70	148
10	8	92	8	0.32	0.40	950
11	8	92	8	0.54	0.50	1517
12	8	92	8	0.53	0.61	995
13	8	92	27	0.62	0.57	1005

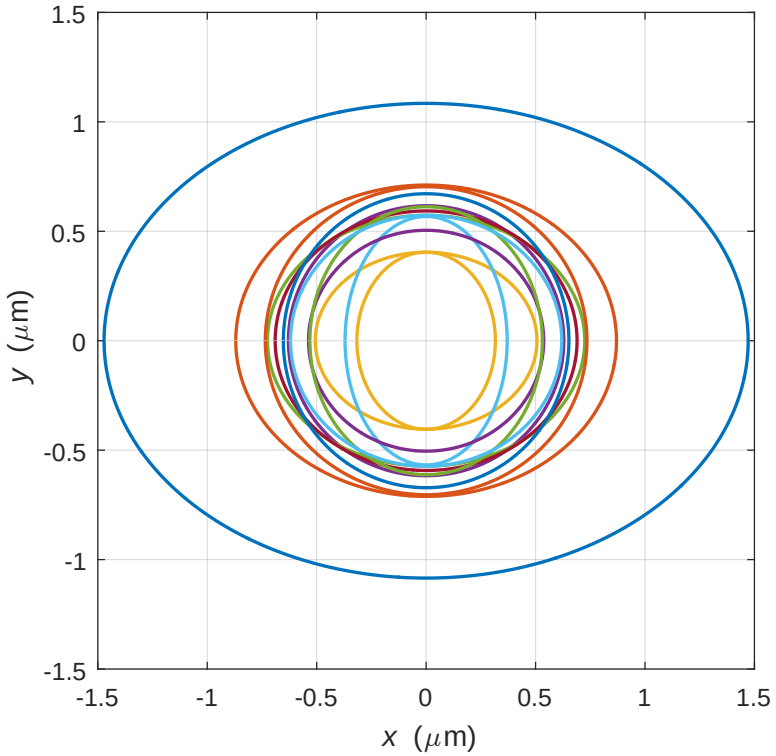

Figure 4.13: Graph of the diffusion domains of the 300 nm diameter trapped spheres corresponding to each trial shown in Table 4.4. The horizontal and vertical arms of each ellipse are given by $\Delta x_{.95}$ and $\Delta y_{.95}$, respectively.

microparticle sizes we studied in our Bessel beam standing wave trap. For comparison, we found the theoretical diffusion coefficients D_{theo}, the experimental unconfined diffusion coefficients D_{msd}, and the confinement factor values u corresponding to the inferred diffusion coefficients D_{inf} of Turkcan et al. [54]. To calculate D_{theo}, we evaluated Eq. (2.41) for each particle size in water ($n = 1.33$). The dynamic (shear) viscosity η of water is determined by [57]

$$\eta(T) = 2.414 \times 10^{-5} \times 10^{247.8/(T-140)}, \tag{4.1}$$

where T is the temperature of water in Kelvin (K) and η has units of Pa·s. Equation (4.1) is accurate to within 2.5% in the temperature range 273.15–643.15 K. To simplify our calculations, we chose the standard value for the viscosity of water ($\eta = 0.890\,\text{mPa·s}$) held at room temperature ($T = 297\,\text{K}$). However, since our trapping laser imparted some additional heat, we acknowledge that our results for D_{theo} will be under-approximations of the actual values. Our results for D_{theo} for each particle size are displayed in Table 4.5. Next, to find D_{msd} and D'_{msd}, we calculated the two-dimensional mean-square displacement $\rho(\tau)$ for the finite trajectories of each particle using [54]

$$\begin{aligned}\rho(\tau) = \rho(n\Delta t) \;&=\; \frac{1}{N-n+1} \sum_{j=1}^{N-n+1} [x(j\Delta t + n\Delta t) - x(j\Delta t)]^2 \\ &\quad + [y(j\Delta t + n\Delta t) - y(j\Delta t)]^2,\end{aligned} \tag{4.2}$$

where N is the total number of points in each trial's data set and $\tau = n\Delta t$ is the time interval between tracking steps. Since the frame rate of our camera was $\sim$15 fps, the time interval between tracking steps was $\tau = \frac{1}{15\,s^{-1}} = 66.7\,\text{ms}$. To improve the accuracy of the measurements of D_{msd} and D'_{msd}, we subtracted the static positioning

Table 4.5: Theoretical diffusion coefficients for each particle size calculated using the Stokes-Einstein-Sutherland equation (See Section 2.5).

Particle Diameter (nm)	D_{theo} ($\mu\text{m}^2/s$)
100	4.89
200	2.44
300	1.63

Table 4.6: Average static noise values for the 200 and 300 nm diameter spheres. For the 100 nm diameter spheres, we used the value we obtained for the 200 nm particles.

Particle Diameter (nm)	$4B^2$ (μm^2)
100	0.0076
200	0.0076
300	0.0180

noise term $4B^2$ from $\rho(\tau)$ for each fitting algorithm[4] [54]:

$$\rho(\tau) - 4B^2 \;=\; 4D\tau, \tag{4.3}$$

$$\rho(\tau) - 4B^2 \;=\; \frac{L_m^2}{3}\left(1 - e^{-\frac{\tau}{\tau_m}}\right). \tag{4.4}$$

To deduce the value of $4B^2$ for each particle size, we collected the tracking data of particles that were adhered to the sample surface and then calculated their mean-square displacement $\rho_{\text{noise}}(\tau)$. Next, we fit the constant $4B^2$ to $\rho_{\text{noise}}(\tau)$ to extrapolate a value. Our results for the average static positioning noise term $4B^2$ for the 200 and 300 nm particles are displayed in Table 4.6. For the 100 nm sphere, we used the value we deduced for the 200 nm particle. A complete list of the values we measured for each experimental trial is provided in Appendix A.4.

To find the noise-corrected, unconfined diffusion coefficients D_{msd} for each particle, we fit[5] the first three points of $[\rho(\tau) - 4B^2]$ to $[4D_{\text{msd}}\tau + C]$, where C is a constant term.

[4]Equations (4.3) and (4.4) are the noise-corrected versions of Eqs. (2.44) and (2.45), respectively.

[5]In Appendix A.3, we provide the MATLAB code we used to (1) graph $[\rho(\tau) - 4B^2]$ and (2) fit the first three points of $[\rho(\tau) - 4B^2]$ to $[4D_{\text{msd}}\tau + C]$ and the first 50–100 points of $[\rho(\tau) - 4B^2]$ to the right-hand side of Eq. (4.4).

The results of our unconfined diffusion fits for the three particles discussed in Figs. 4.5–4.10 are displayed in Figs 4.14, 4.16, and 4.18. Next, to find the noise-corrected, confined diffusion coefficients D'_{msd}, we fit the first[6] 50–100 points of $[\rho(\tau) - 4B^2]$ to the right-hand side of Eq. (4.4). The results of our confined diffusion fits for the three particles discussed in Figs. 4.5–4.10 are displayed in Figs 4.15, 4.17, and 4.19. These fits gave us values for τ_{m} and L_{m}, which we inserted into Eqs. (2.47) and (2.48) to obtain the detector-corrected values τ_{msd} and L_{msd}. Finally, we plugged τ_{msd} and L_{msd} into Eq. (2.49) to find experimental values for D'_{msd}.

We then performed a statistical analysis of the results we obtained for D_{msd} and D'_{msd}. The values for D_{msd}, D'_{msd}, L_{msd}, and $D'_{\mathrm{msd}}/D_{\mathrm{theo}}$ for all the trials corresponding to each particle size are recorded in Tables 4.7–4.9. The averages and standard deviations of these data sets depended on what trials we chose to include in the analysis. In order to eliminate outliers, we removed any trial whose value for $D'_{\mathrm{msd}}/D_{\mathrm{theo}}$ was less than 0.10. The trials in this category are highlighted in red in the tables. The highlighted diffusion values that are marked with an asterisk (*) in Table 4.8 could not be corrected[7] for detector exposure time using Eqs. (2.47) and (2.48) given that $\frac{\tau_{\mathrm{msd}}}{T}$ was less than 10 for those trials. Next, we found the mean $\bar{x}$ and standard deviation σ of the remaining values in each data set. The results for $\bar{x}$ and σ for each data set are listed in bold at the bottom of Tables 4.7–4.9, and the values for $\bar{x}$ are summarized in Table 4.10. The results in Table 4.10 reveal that (1) compared to the results for D_{msd}, the values for D'_{msd} more closely approximate D_{theo} for each particle size; (2) the mean values of D'_{msd} follow the expected trend of decreasing diffusion coefficient magnitude with increasing particle diameter; and (3) the agreement between D'_{msd} with D_{theo} is better for the larger (slower moving) particles.

[6]For trials with fewer than 200 tracked points in the original data set, we used either 50 or 70 points of $[\rho(\tau) - 4B^2]$ for our fits.

[7]See Section 2.5.

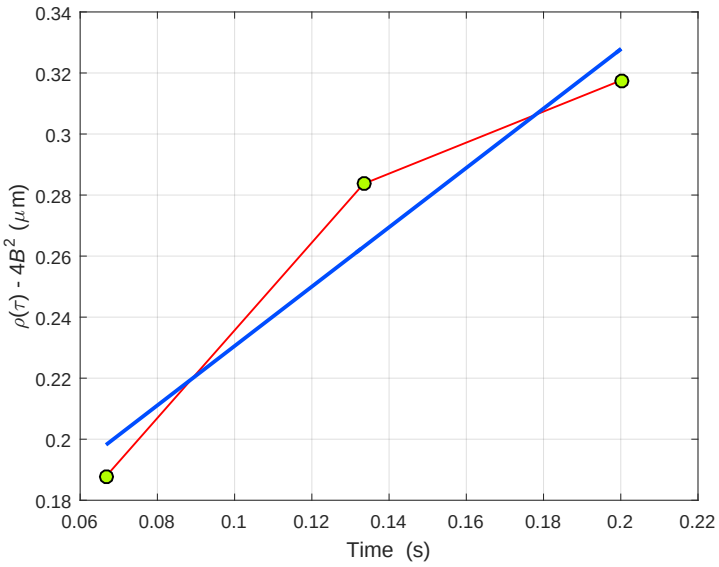

Figure 4.14: Fit of $[4D\tau + \mathrm{C}]$ to the first three points of $[\rho(\tau) - 4B^2]$, where $[\rho(\tau) - 4B^2]$ was calculated using the data for the 100 nm diameter sphere from Trial 9 in Table 4.2.

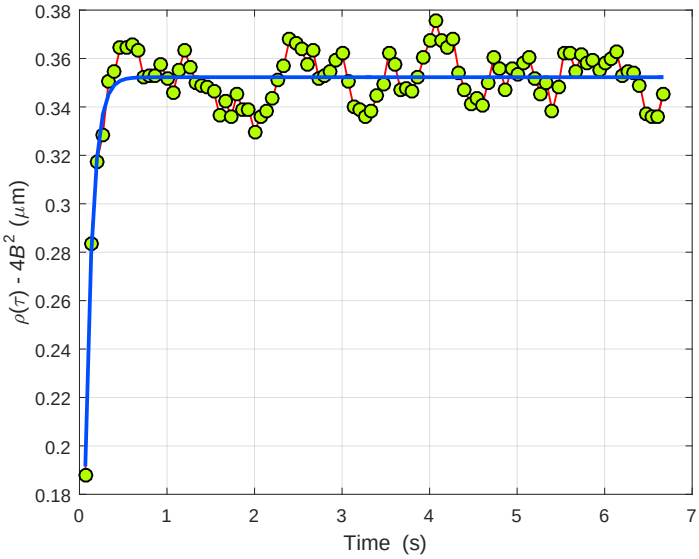

Figure 4.15: Fit of the right-hand side of Eq. (4.4) to the first 100 points of $[\rho(\tau) - 4B^2]$, where $[\rho(\tau) - 4B^2]$ was calculated using data for the 100 nm diameter sphere from Trial 9 in Table 4.2.

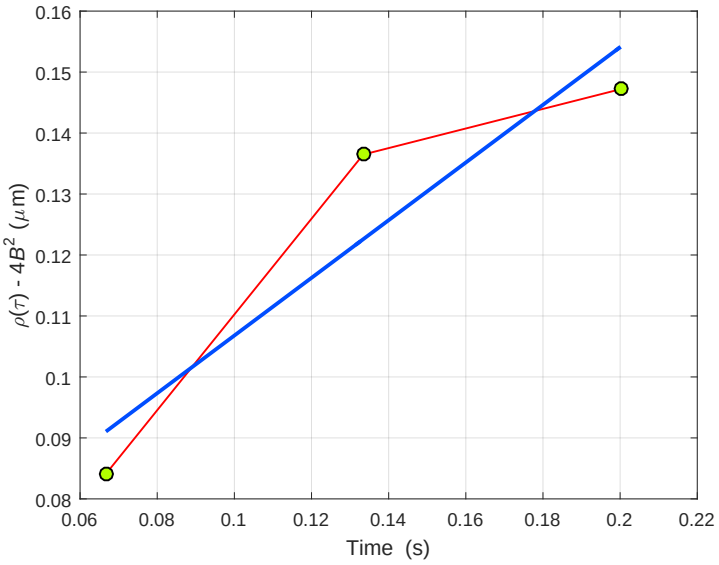

Figure 4.16: Fit of $[4D\tau + \mathrm{C}]$ to the first three points of $[\rho(\tau) - 4B^2]$, where $[\rho(\tau) - 4B^2]$ was calculated using the data for the 200 nm diameter sphere from Trial 7 in Table 4.3.

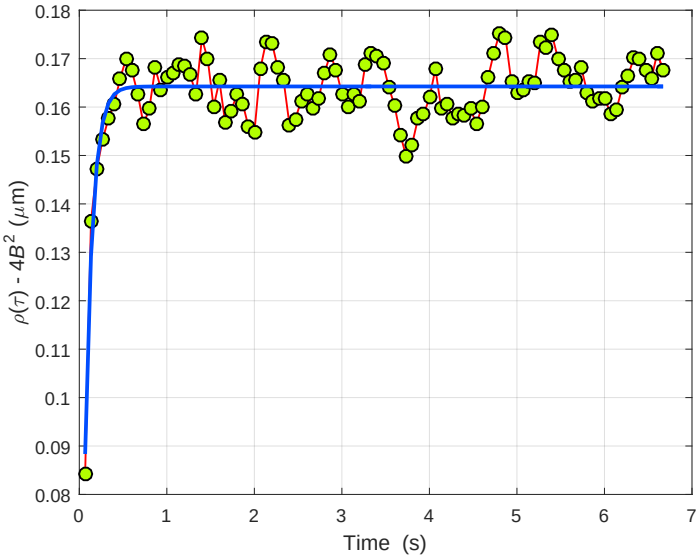

Figure 4.17: Fit of the right-hand side of Eq. (4.4) to the first 100 points of $[\rho(\tau) - 4B^2]$, where $[\rho(\tau) - 4B^2]$ was calculated using data for the 200 nm diameter sphere from Trial 7 in Table 4.3.

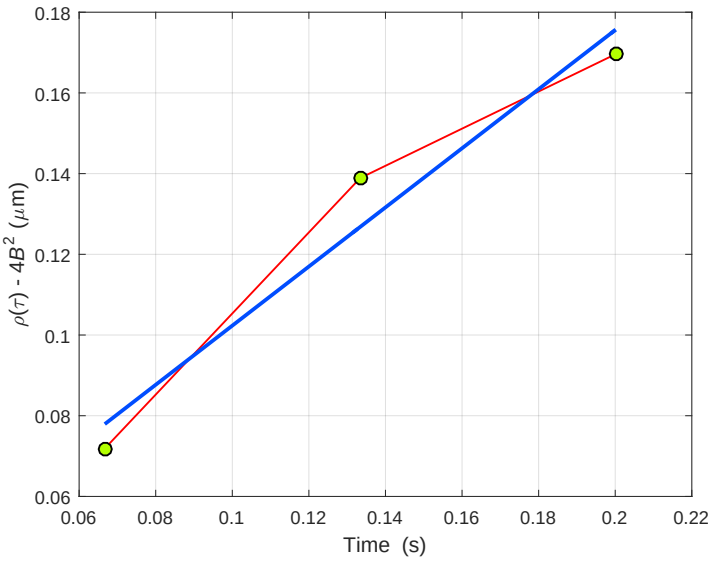

Figure 4.18: Fit of $[4D\tau + \mathrm{C}]$ to the first three points of $[\rho(\tau) - 4B^2]$, where $[\rho(\tau) - 4B^2]$ was calculated using the data for the 300 nm diameter sphere from Trial 6 in Table 4.4.

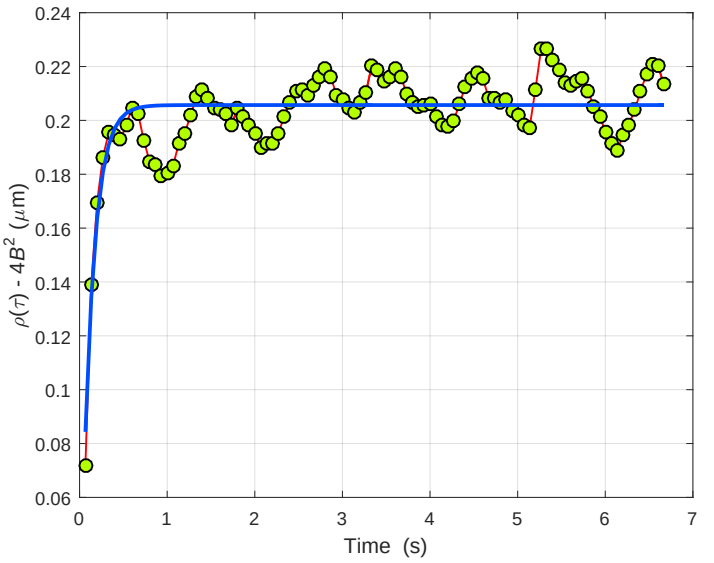

Figure 4.19: Fit of the right-hand side of Eq. (4.4) to the first 100 points of $[\rho(\tau) - 4B^2]$, where $[\rho(\tau) - 4B^2]$ was calculated using data for the 300 nm diameter sphere from Trial 6 in Table 4.4.

Table 4.7: Experimental diffusion values for the 100 nm diameter particles. We removed trials (red) in the data set if $D'_{\text{msd}}/D_{\text{theo}} < 0.10$. The means $\bar{x}$ and standard deviations σ do not include the values in red.

Trial	D_{msd} $(\frac{\mu m^2}{s})$	D'_{msd} $(\frac{\mu m^2}{s})$	L_{msd} (μm)	$D'_{\text{msd}}/D_{\text{theo}}$	$R_{.95}$ (μm)	u
1	0.16	0.32	0.88	0.07	0.68	0.015
2	0.11	0.26	0.81	0.05	0.63	0.014
3	0.80	1.60	2.47	0.33	2.05	0.008
4	1.01	1.24	2.64	0.25	2.00	0.007
5	0.65	0.75	1.98	0.15	1.28	0.010
6	0.24	2.65	1.21	0.54	0.78	0.092
7	0.41	2.01	1.39	0.41	0.88	0.055
8	0.26	1.37	1.18	0.28	0.76	0.051
9	0.24	2.08	1.23	0.43	0.75	0.078
$\bar{\mathbf{x}}$	**0.52**	**1.67**	**1.73**	**0.34**	**1.22**	**0.043**
σ	**0.31**	**0.63**	**0.63**	**0.13**	**0.58**	**0.016**

Table 4.8: Experimental diffusion values for the 200 nm diameter particles. We removed trials (red) in the data set if $D'_{\text{msd}}/D_{\text{theo}} < 0.10$. The means $\bar{x}$ and standard deviations σ do not include the values in red. Note: The diffusion values marked with an asterisk (*) could not be corrected for correlated motion. We used the uncorrected diffusion coeffecients D'_{m} and microdomains L_{m} for these trials.

Trial	D_{msd} $(\frac{\mu m^2}{s})$	D'_{msd} $(\frac{\mu m^2}{s})$	L_{msd} (μm)	$D'_{\text{msd}}/D_{\text{theo}}$	$R_{.95}$ (μm)	u
1	0.19	0.18	0.85	0.07	0.64	0.009
2	0.09	0.04*	1.14*	0.02*	0.93*	0.001*
3	1.00	0.75	2.21	0.31	1.46	0.007
4	0.12	0.06*	1.24*	0.03*	0.84*	0.001*
5	0.75	1.14	2.22	0.47	1.89	0.007
6	0.36	0.87	1.24	0.36	0.86	0.025
7	0.12	1.02	0.86	0.42	0.55	0.073
8	0.35	0.90	1.33	0.37	0.84	0.027
9	1.26	2.47	2.35	1.01	1.93	0.014
10	0.59	3.10	1.67	1.27	1.10	0.055
11	0.07	2.65	1.04	1.09	0.62	0.145
12	0.23	1.20	0.93	0.49	0.65	0.060
13	0.10	0.03*	2.33*	0.02*	1.02*	0.001*
$\bar{\mathbf{x}}$	**0.53**	**1.57**	**1.54**	**0.64**	**1.10**	**0.046**
σ	**0.41**	**0.90**	**0.59**	**0.37**	**0.54**	**0.044**

Table 4.9: Experimental diffusion values for the 300 nm diameter particles. We did not remove any trials in the data set because no trial satisfied the condition $D'_{\text{msd}}/D_{\text{theo}} < 0.10$. Therefore, the means $\bar{x}$ and standard deviations σ include all values from the data set.

Trial	D_{msd} $(\frac{\mu\text{m}^2}{s})$	D'_{msd} $(\frac{\mu\text{m}^2}{s})$	L_{msd} (μm)	$D'_{\text{msd}}/D_{\text{theo}}$	$R_{.95}$ (μm)	u
1	0.89	1.19	2.21	0.73	1.58	0.010
2	0.50	1.07	1.41	0.66	1.00	0.023
3	0.18	0.73	0.86	0.45	0.57	0.047
4	0.32	1.28	1.13	0.79	0.75	0.048
5	0.33	0.95	1.17	0.58	0.84	0.028
6	0.18	0.60	0.87	0.37	0.61	0.034
7	0.33	1.18	1.20	0.72	0.82	0.038
8	0.36	1.39	1.25	0.85	0.83	0.043
9	0.38	1.09	1.25	0.67	0.98	0.024
10	0.06	0.25	0.53	0.15	0.46	0.025
11	0.16	0.46	0.89	0.28	0.65	0.023
12	0.25	1.28	1.06	0.78	0.71	0.053
13	0.29	1.83	1.18	1.12	0.74	0.070
$\bar{\mathbf{x}}$	**0.33**	**1.02**	**1.15**	**0.63**	**0.84**	**0.036**
σ	**0.20**	**0.42**	**0.39**	**0.26**	**0.27**	**0.016**

Next, we completed a one-tailed, independent-samples t-test to determine if the mean $\bar{x}$ of each data set of confined diffusion coefficients D'_{msd} was statistically unique. We wanted to reject the null hypothesis that the means of the D'_{msd} values for each particle size are the same. In order to reject this hypothesis, we had to obtain a p-value of less than 0.05 for each comparison in our t-test calculations. According to the results of our analysis (see Table 4.11), the mean of the D'_{msd} values for the 300 nm diameter spheres was statistically lower than the mean of the D'_{msd} values for the 100 nm diameter particles. In the future, we propose to collect more tracking data in order to confirm that the mean of the D'_{msd} values for the 200 nm diameter spheres was statistically lower than the mean of the 100 nm particles and statistically higher than the mean of the 300 nm particles.

Within a certain range of laser powers, our results for D'_{msd} agree fairly well with the results of a more sophisticated Bayesian inference scheme developed by Turkcan

Table 4.10: Average experimental diffusion coefficients D_{msd} and D'_{msd} for each particle diameter D compared to the theoretical values D_{theo}. The number (#) of trials included from each data set is indicated on the left.

D (nm)	# of Trials	D_{msd} $(\frac{\mu\text{m}^2}{s})$	D'_{msd} $(\frac{\mu\text{m}^2}{s})$	D_{theo} $(\frac{\mu\text{m}^2}{s})$	$D'_{\text{msd}}/D_{\text{theo}}$
100	7	0.52	1.67	4.89	0.34
200	9	0.53	1.57	2.44	0.64
300	13	0.33	1.02	1.63	0.63

Table 4.11: Calculated p-values from a one-tailed, independent-samples t-test of the data sets corresponding to each particle diameter D.

D (nm)	100 (p-value)	200 (p-value)	300 (p-value)
100	–	0.3930	0.0182
200	0.3930	–	0.0606
300	0.0182	0.0606	–

et al. [54]. In this technique, the inferred diffusion coefficients D_{inf} were extracted based on the transition probabilities of the particles' motion. As reported in Fig. 5 of [54], the confined diffusion coefficients D'_{msd} that they measured using mean-square displacement fits to the right-hand side of Eq. (4.4) matched their D_{inf} values within the range of $0.00 \leq u \leq 0.020$, where u is the confinement factor of the diffusing particles. The confinement factor is defined to be

$$u \;=\; \frac{D\tau}{\pi(R_{.95})^2}, \tag{4.5}$$

where $R_{.95}$ is the radius of a circle that contains 95% of the tracking points. Our results for $R_{.95}$ and u based on our tracking data are listed in Tables 4.7–4.9. As shown in the plots of $R_{.95}$ and u as functions of P_T in Figs. 4.20–4.25, our experimental values of u for each particle size fall within the range specified in Fig. 5 of [54] as long as $P_T \leq 8.7\,\text{W}$ for the 100 nm sphere, $P_T \leq 6.7\,\text{W}$ for the 200 nm sphere, and $P_T \leq 3.6\,\text{W}$ for the 300 nm sphere[8]. Thus, our results for D'_{msd} appear to agree

[8]One interesting obervation here is that the boundary on the power decreases with increasing particle size. By collecting more data, we could confirm the statistical significance of this trend between D_{inf} and D'_{msd}.

with the results for D_{inf} within these ranges of laser powers. It's important to clarify, however, that Turkcan et al. applied a Gaussian potential to arrive at their values for D_{inf}. Therefore, since a Gaussian potential is a rough estimate of the actual Bessel beam standing wave potential inherent in our setup, we don't necessarily anticipate that the values for D'_{msd} within the power ranges specified above would more closely agree with D_{theo} compared to values from other power ranges.

Lastly, the plots of $R_{.95}$ and u as functions of P_T suggest notable trends. It appears that $R_{.95}$ decreases with increasing trapping power and u increases with increasing power. Both of these results are expected because the power is inversely proportional to $R_{.95}$ and directly proportional to u. To confirm this relationship, more data might be needed in order to obtain results that are more statistically rigorous.

In the final part of our analysis, we address the following issues apparent from our results:

1. The mean values of D'_{msd} are systematically low compared to D_{theo}.
2. The most stable motion in each data set corresponds to the lowest diffusion coefficient.
3. Some images of the microspheres appear to show two particles in the trap.
4. Compared to theory, there is little difference between the diffusion coefficients of the three different-sized particles.

First, the mean values of D'_{msd} are systematically low compared to D_{theo}. That is, for each particle size, the mean value of the D'_{msd} values is smaller than the corresponding theoretical prediction D_{theo}. To understand this result, we must recall what D_{theo} represents. The value of D_{theo} corresponds to a freely moving Brownian microsphere situated far away from any surfaces or other external potentials. On the

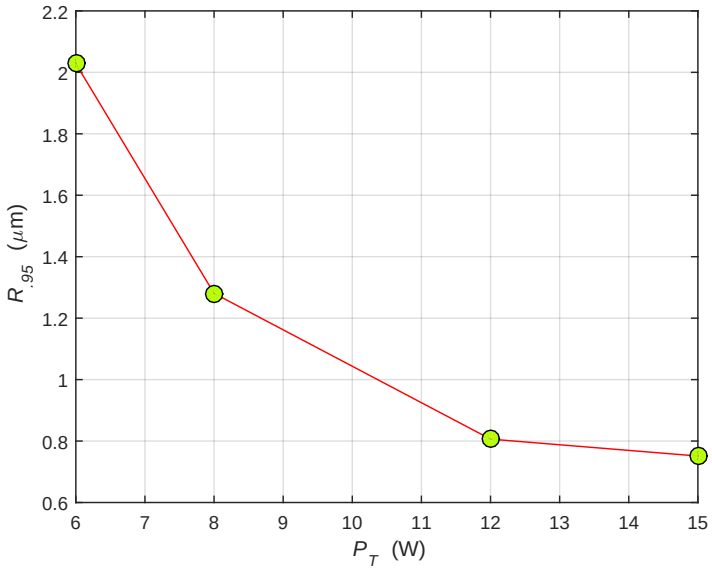

Figure 4.20: Plot of the average diffusing radius $R_{.95}$ of the 100 nm diameter sphere as a function of the total power P_T of the fiber laser. The graph indicates a general downward trend in radial diffusion with increasing trapping power.

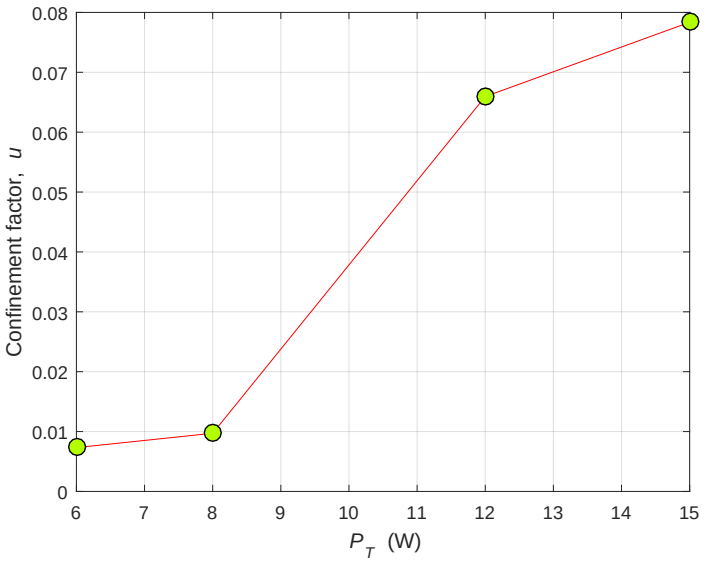

Figure 4.21: Plot of the average confinement factor u of the 100 nm diameter sphere as a function of the total power P_T of the fiber laser. The graph suggests a general upward trend in the confinement factor with increasing trapping power.

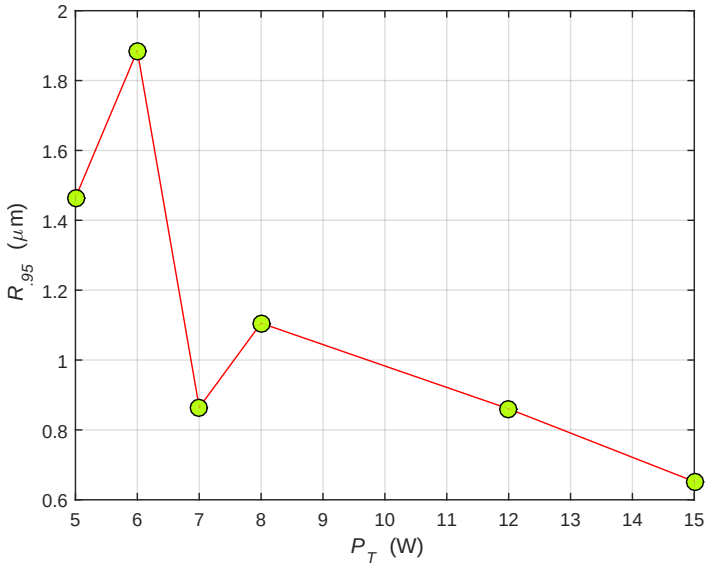

Figure 4.22: Plot of the average diffusing radius $R_{.95}$ of the 200 nm diameter sphere as a function of the total power P_T of the fiber laser. The graph indicates a general downward trend in radial diffusion with increasing trapping power.

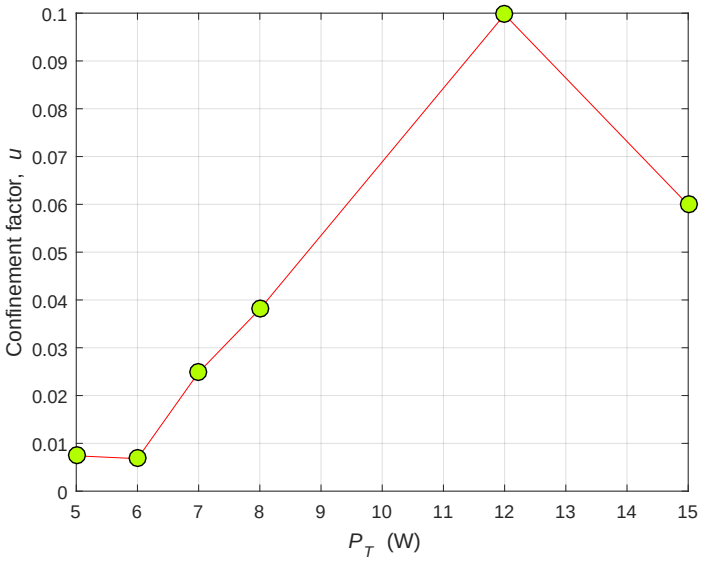

Figure 4.23: Plot of the average confinement factor u of the 200 nm diameter sphere as a function of the total power P_T of the fiber laser. The graph suggests a general upward trend in the confinement factor with increasing trapping power.

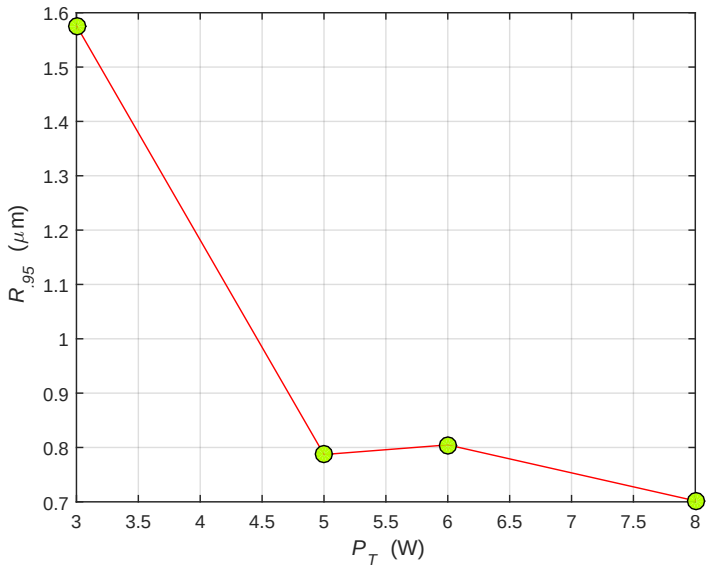

Figure 4.24: Plot of the average diffusing radius $R_{.95}$ of the 300 nm diameter sphere as a function of the total power P_T of the fiber laser. The graph indicates a general downward trend in radial diffusion with increasing trapping power.

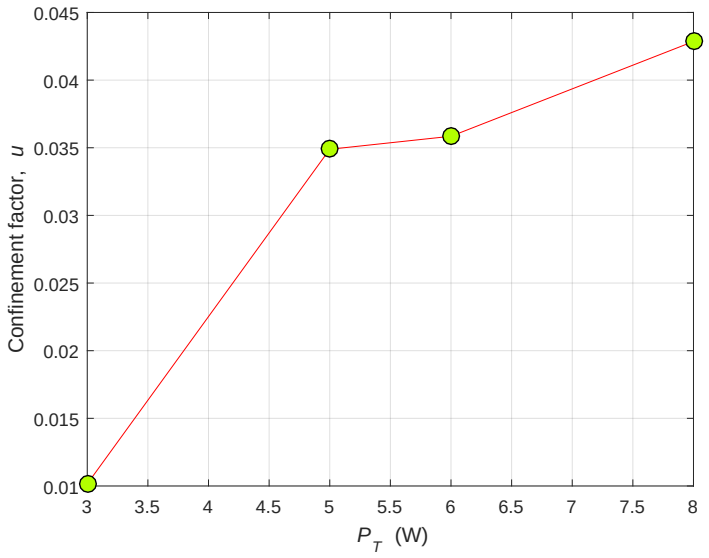

Figure 4.25: Plot of the average confinement factor u of the 300 nm diameter sphere as a function of the total power P_T of the fiber laser. The graph suggests a general upward trend in the confinement factor with increasing trapping power.

other hand, the motion of a microsphere in our trap is optically-perturbed by the high irradiance gradients of the Bessel beam standing wave. Thus, we would expect the particle's diffusion to be hindered and, therefore, the diffusion coefficient of the particle to be lowered. Moreover, the generic formula for confined diffusion, although more accurate than Einstein's unconfined diffusion model, does not incorporate the full optical potential[9] $V(\mathbf{r})$ of the Bessel beam standing wave. Therefore, we suspect that Eq. (4.4) does not fully describe the motion of a confined particle in our trap. To better account for the confined diffusion of each particle, we could perform a Bayesian inference analysis [54] that includes the potential $V(\mathbf{r})$ from our trap.

Second, the most stable motion in each data set corresponds to the lowest diffusion coefficient. Stability in this case is determined by the total frame count. The higher the frame count, the more stable the motion. In other words, if we were able to track a particle for more overall time, then by extension the particle was less likely the leave the trap. Therefore, the trials of the most stable motion for each data set are the 100 nm particle trapped at 9 μm from the surface with 69 mW of power (Trial 2 from Table 4.2), the 200 nm particle trapped at 6 μm from the surface with 57 mW of power (Trial 2 from Table 4.3), and the 300 nm particle trapped at 8 μm from the surface with 92 mW of total power (Trial 11 from Table 4.4). To explain this behavior, we hypothesize that these particles were somehow interacting with the surface to maintain their trapping stability. It is conceivable, for example, that the image location of the oil immersion objective lens could have drifted toward the reflective surface if the oil or one of the optical components was accidentally moved. Since each particle was relatively close to the surface to begin with, subtle movements could have a significant effect.

Third, some images of the microspheres appear to show two particles in the trap. In

[9]See Eq. (2.37).

Figs. 4.5, 4.7, and 4.9, two distinct spots occur in some of the frames. It is possible that instead of two particles, these images show high relative movement of a single particle in the slow time interval of a frame, which for our experiments was $\tau \simeq \frac{1}{15s^{-1}} = 0.066\,\mathrm{s}$. To find out if blurs and streaks in the image may be due to the diffraction of the fluorescent light from the particle, we calculate the expected displacement R_{rms} of the particle during a frame,

$$R_{\mathrm{rms}} \;=\; 2\sqrt{D_{\mathrm{theo}}\tau}, \tag{4.6}$$

and compare it to the diffraction limited spot of ∼2 pixels, which is required by the Nyquist sampling rate of our camera and objective lens. For the 100 nm particle, we have $D_{\mathrm{theo}} = 4.89\,\mu\mathrm{m}^2/s$. Therefore, we get $R_{\mathrm{rms}} = 1.14\,\mu\mathrm{m}$, or ∼9.3 camera pixels for our optical setup. This size is significant compared to the diffraction limited spot. Therefore, it is possible that the double images in the frames are actually blurs and streaks caused by the high relative motion of the particles. An obvious way to eliminate these streaks is to lower the time interval τ, or raise the frame rate. To accomplish this, we could maximize the frame rate of the camera (PointGrey, Flea2) at 60 fps and crop in half the region of interest (ROI) of the imaging field using the video recording software (NorPix StreamPix 5.0). These changes would increase the overall frame rate by a factor of 8, and, consequently, improve the clarity of the captured images.

Lastly, there is little difference between the diffusion coefficients of the three different-sized particles. The anticipated pattern of increasing D'_{msd} with decreasing particle size is confirmed by the mean values of D'_{msd} for the 100, 200, and 300 nm particles. However, based on our independent-samples t-test, the mean values of D'_{msd} for the 200 nm diameter particles were not different enough from the other data sets to be statistically significant. That is, the values between the 100 and 200 nm beads

and the values between the 200 and 300 nm beads were too close to confirm the expected pattern of increasing D'_{msd} with decreasing particle size. The convergence of the mean values of D'_{msd} could be caused by either the low frame rate of the camera or by the interaction dynamics of the optical potential. A low frame rate is unable to capture the faster movement of the smaller particles, thus decreasing the differences in the means of D'_{msd}. It is also possible that the 100 nm diameter particles formed undetected particle clusters comprising two or more spheres in a bound aggregate. Since these clusters would be larger in size, their diffusion coefficients would be smaller. Additionally, the faster motion of the 100 nm particle could account for the higher deviance of D'_{msd} from D_{theo}. As for the interaction dynamics, the tight confinement of the particles along the axial axis could be coupled into the confinement along the transverse axes. By using the Bayesian inference technique to incorporate our potential $V(\mathbf{r})$ into the analysis, we may be able to learn if the interaction dynamics are hindering the particles' lateral diffusion.

In conclusion, the mean values we obtained for the confined diffusion coefficient D'_{msd} of each sphere diameter follow the expected pattern of increasing D'_{msd} with decreasing particle size. We showed using a one-tailed, independent-samples t-test that the differing results for the 100 and 300 nm particles are statistically significant. Moreover, the mean values D'_{msd} for each particle size appear to be better approximations to the theoretical diffusion coefficients D_{theo} than are the mean values of the unconfined diffusion coefficient D_{msd}. Lastly, to increase the magnitudes and spread of the mean values of D'_{msd} and to improve the clarity of our images, we propose to experiment with a higher video frame rate for capturing images and to analyze our data using the Bayesian inference technique developed by Turkcan et al. [54].

Chapter 5: Conclusion

5.1 Summary

The interactions of light with matter inspire an abundance of fascinating questions and opportunities in scientific research. Beginning with the invention of the laser, light has become useful for trapping and manipulating microscopic particles in several interesting and productive ways. However, the limitations of previous optical trapping models presented complications for analyzing Brownian particle diffusion. Specifically, we were not able to find in the literature a trap that both created stable trapping planes for tracking transverse particle motion and eliminated the need to account for surface effects.

In this thesis, we reported the first realization of two-dimensional, transverse tracking of Brownian particles in multiple, surface-isolated traps. To achieve this, we constructed a Bessel beam standing wave lattice whose parameters were adjusted to allow tight, one-dimensional axial confinement and loose, two-dimensional transverse confinement of microscopic-sized particles in the central spot of the beam. We chose to use a Bessel beam to build our trap because its unique non-diffracting and self-healing properties provided distinct advantanges over the use of a Gaussian beam. In particular, a Bessel beam standing wave was shown to produce optical potential wells that are more abundant, uniform, and stable than those of a Gaussian standing wave.

In our analysis, we showed that the Bessel beam standing wave trap may act as a unique probe into the characteristics of viscous media. We collected tracking data of 100, 200, and 300 nm diameter particles submerged in water and then quantified their motion using mathematical relationships for the mean-square displacement of the particles. Since the particles moved inside the confined region of an optical potential

well, a diffusion theory that described confined motion was necessary for accurately modeling the dynamics of the particles. We opted to use the general equation for confined diffusion to extract diffusion coefficients for each of the particles we studied. Specifically, we fit the mean-square displacement points to the right-hand side of Eq. (4.4), thereby revealing experimental values for the confined diffusion coefficients D'_{msd}. Compared to the expected diffusion coefficients D_{theo} given by Eq. (2.41), our results for D'_{msd} follow the expected pattern but are systematically low. However, because the generic expression for confined diffusion does not fully describe the motion of Brownian microparticles in our Bessel beam standing wave trap[1], some discrepancy is expected. Furthermore, we also compared our results for D'_{msd} with the diffusion coefficients D produced by Einstein's theory of unconfined diffusion and the diffusion coefficients D_{inf} deduced from the Bayesian inference scheme of Turkcan et al. [54]. Based on our results, the generic expression for confined diffusion proved to be more accurate than the unconfined diffusion model and equivalent to the Bayesian inference technique for particular ranges of the laser power.

5.2 Experimental Design Improvements

In the future, we propose to make the following revisions of our experimental methodology so as to better align our experimental results of transverse Brownian diffusion in a Bessel beam standing wave with the theoretical predictions of this unique type of motion:

1. Increase the reflectivity of the bottom surface of the sample chamber in order to decrease the downward scattering force.

2. Adjust the parameters of the axicon and the refracting telescope in order to

[1]See Section 2.5.

create a larger Bessel beam trapping radius.

3. Increase the frame rate of the camera to improve the temporal resolution of our imaging.

4. Reduce the camera gain in order to enhance the spatial resolution of our images.

5. Apply a Bayesian statistical model that incorporates the full potential of our Bessel beam standing wave.

By implementing these improvements, we hope to collect tracking data that is more realistic and to explain the data more accurately. In doing so, we anticipate to gain (1) an increase in both the magnitude and spread of the mean experimental diffusion coefficients for each particle size, (2) an increase in the statistical significance of our data (i.e. lower p-values), (3) more convincing evidence that only one particle is confined in each standing wave trapping plane at a time, (4) a clearer understanding of the possible interaction dynamics of the Bessel beam standing wave optical potential, and (5) better confirmation of the downward trend in trapping radius with increased trapping power and the upward trend in the confinement factor with increased power.

5.3 Research Applications

The Bessel beam standing wave trap may have beneficial applications in microrheology and microfluidics research. First, our confinment and tracking techniques may be useful for approximating the viscosity of semi-dilute polymer solutions. According to de Gennes's theory of semi-dilute polymer solutions, the solution viscosity η is given by [58]

$$\eta \simeq ET_{\mathrm{R}}, \tag{5.1}$$

where E is the shear elastic modulus of the polymer and T_{R} is the longest relaxation time for a particular polymer subchain. In de Gennes's theory, semi-dilute polymer chains comprise a series of discrete subchains whose thermal motion, or reptation, is modeled by the movement of an imaginary tube surrounding each subchain. For each subchain, the tube is defined by all of the other subchains positioned around it. The relaxation time T_{R} can be thought of as the time required for a subchain to move the entire length L of the tube, and is determined by

$$T_{\mathrm{R}} \simeq \frac{L^2}{D_{\mathrm{r}}}, \tag{5.2}$$

where D_{r} is the diffusion coefficient of the subchain along its tube. In Eq. (5.2), the subchain is a Rouse chain modeled after a string of Brownian particles connected by springs. By extension, the confined diffusion coefficient D'_{msd} can be thought of as a Rouse chain consisting of just one Brownian particle. Thus, if we meausure the confined diffusion coefficient D'_{msd} of a microsphere corralled by our Bessel beam standing wave trap and submerged in a semi-dilute polymer solution, we can then use Eqs. (5.1) and (5.2) to find an experimental approximation for the viscosity η of the solution.

The Bessel beam standing wave trap may also prove to be a useful tool for measuring fluid drag forces near surfaces. According to Eq. (2.33), surface forces in our experiments were negligible in the m^{th} antinode of the Bessel beam standing wave as long as $m \geq 4$. Therefore, our optical setup contained two distinct force regimes, one where surface drag forces were negligible and one where they were substantial. In future experiments, if we compare the measured diffusion coefficients of particles trapped far away from the surface with the measured diffusion coefficients of particles trapped nearby, we may be able to extrapolate information about the fluid drag forces from the discrepancy in the two results.

In addition to experimental microrheology and microfluidics, our work may have practical applications in basic optics research. For example, the motion of Brownian particles in the Bessel beam standing wave may reveal information about the beam that could be useful for better understanding Bessel beam standing waves in general. Apart from the tracking data we already collected, we could experiment with different types of laser polarizations, particle shapes (e.g. spheres vs. rods), and particle materials in order to more fully characterize the beam. Moreover, it may be advantageous to model our Bessel beam standing wave trap using computer simulations in order to develop a more rigorous theoretical model of the particles' motion. By adjusting the parameters of our algorithms in a computational environment, we could study the beam under a variety of conditions. Furthermore, we could use the model to anticipate the possible challenges of a given experiment. As with all research, there may be other potential, even unforeseeble, applications of the work presented here. Considering the popular appeal of current research in optical physics and microfluidics, and the interdisciplinary nature of our project, we hope that the future directions of our research will be promising.

Bibliography

[1] Kepler, J., *De cometis libelli tres* (1619).

[2] Maxwell, J.C., *A treatise on electricity and magnetism*, 1st Ed., Oxford, 2, 391 (1873).

[3] Nichols, E. F., and Hull, G. F., "A preliminary communication on the pressure of heat and light radiation," Phys. Rev., 13, 307 (1901).

[4] Nichols, E. F., and Hull, G. F., "The pressure due to radiation," Phys. Rev., 17, 26 (1903).

[5] Schawlow, A.L., Townes, C.H., "Infrared and optical masers," Phys. Rev., 112, 1940-1949 (1958).

[6] Maiman, T.H., "Stimulated optical radiation in ruby," Nature, 187, 494 (1960).

[7] Gould, R. G., "The LASER, Light Amplification by Stimulated Emission of Radiation". In Franken, P.A. and Sands, R.H. (Eds.). The Ann Arbor Conference on Optical Pumping, the University of Michigan, 15, 128 (1959).

[8] Ashkin, A., "Acceleration and trapping of particles by radiation pressure," Phys. Rev. Lett., 24, 156-159 (1970).

[9] Ashkin, A., "Optical trapping and manipulation of neutral particles using lasers," Proc. Natl. Acad. Sci., 94, 4853-4860 (1997).

[10] Ashkin, A., Dziedzic, J.M., Bjorkholm, J.E., and Chu, S., "Observation of a single-beam gradient force optical trap for dielectric particles," Opt. Lett., 11, 288-290 (1986).

[11] Chu, S., Bjorkholm, J.E., Cable, A., Ashkin, A.,"Experimental observation of optically trapped atoms," Phys. Rev. Lett., 57, 314-317 (1986).

[12] Ashkin, A., Dziedzic, J.M.,"Optical levitation by radiation pressure," Appl. Phys. Lett., 19, 283-285 (1971).

[13] Ashkin, A., Dziedzic, J.M., "Stability of optical levitation by radiation pressure," Appl. Phys. Lett., 24, 586-588 (1974).

[14] Ashkin, A., Dziedzic, J.M., "Optical levitation in high vacuum," Appl. Phys. Lett., 28, 333-335 (1976).

[15] Ashkin, A., Dziedzic, J.M., "Feedback stabilization of optically levitated particles," Appl. Phys. Lett., 30, 202-204 (1977).

[16] Ashkin, A., Dziedzic, J.M., "Observation of light scattering from nonspherical particles using optical levitation," Appl. Opt., 19, 660-668 (1980).

[17] Constable, A., Kim, J., Mervis, J., Zarinetchi, F., Prentiss, M., "Demonstration of a fiber-optical light-force trap," Opt. Lett., 18, 1867-1869 (1993).

[18] Lyons, E., Sonek, G., "Confinement and bistability in a tapered hemispherically lensed optical fiber trap," Appl. Phys. Lett., 66, 1584-1586 (1995).

[19] Zemánek, P., Jonáš, A., Šrámek, L., Liška, M., "Optical trapping of Rayleigh particles using a Gaussian standing wave," Opt. Commun., 151, 273-285 (1998).

[20] Zemánek, P., Jonáš, A., Šrámek, L., Liška, M., "Optical trapping of nanoparticles and microparticles by a Gaussian standing wave," Opt. Lett., 24, 1448-1450 (1999).

[21] Zemánek, P., Jonáš, A., Jákl, P., Ježek, J., Serý, M., Liška, M., "Theoretical comparison of optical traps created by standing wave and single beam," Opt. Commun., 220, 401-412 (2003).

[22] Mu, W., Li, Z., Luan, L., Spalding, G.C., Wang, G., Ketterson, J.B., "Force measurement on microspheres in an optical standing wave," J. Opt. Soc. Am. B, 25, 763-767 (2008).

[23] Čižmár, T., Garcéz-Chávez, V., Dholakia, K., Zemánek, P., "Optical trapping in counter-propagating Bessel beams," Optical Trapping and Optical Manipulation, Published in Proceedings of SPIE, 5514, 643-651 (2004).

[24] Rohner, J., Fournier, J., Jacquot, P., Merenda, F., Salathé, R., "Multiple optical trapping in high gradient interference fringes," Optical Trapping and Optical Micromanipulation III, San Diego, CA, USA. Published in Proceedings of SPIE, 6326, 632606 (2006).

[25] Sasaki, K., Koshioka, M., Misawa, H., Kitamura, N., Masuhara, H., "Pattern-formation and flow-control of fine particles by laser-scanning micromanipulation," Opt. Lett., 16, 1463-1465 (1991).

[26] Reicherter, M., Haist, T., Wagemann, E., Tiziani, H., "Optical particle trapping with computer-generated holograms written on a liquid-crystal display," Opt. Lett., 24, 608-610 (1999).

[27] Čižmár, T., Šiler, M., Šerý, M., Zemánek, P., "Optical sorting and detection of submicrometer objects in a motional standing wave," Phys. Rev. B, 74, 035105, (2006).

[28] Ricárdez-Vargas, I., Rodríguez-Montero, P., Ramos-García, R., Volke-Sepúlveda, K., "Modulated optical sieve for sorting of polydisperse microparticles," Appl.

Phys. Lett., 88, 121116, (2006).

[29] Mennerat-Robilliard, C., Boiron, D., Fournier, J.M., Aradian, A., Horak, P., Grynberg, G., "Cooling cesium atoms in a Talbot lattice," Europhys. Lett., 44, 442-448, (1998).

[30] Chávez-Cerda, S., Padgett, M. J., Allison, I., New, G. H. C., Gutiérrez-Vega, J. C., O'Neil, A. T., MacVicar, I., Courtial, J., "Holographic generation and orbital angular momentum of high-order Mathieu beams," J. Opt. B, 4, S52-S57 (2002).

[31] Durnin, J., "Exact solutions for nondiffracting beams. I. The scalar theory," J. Opt. Soc. Am. A, 4, 651-654 (1987).

[32] Durnin, J., Miceli, J.J., Eberly, J.H., "Diffraction-Free Beams," Phys. Rev. Lett., 58, 1499-1501, (1987).

[33] Durnin, J., Miceli, J.J., Eberly, J.H., "Comparison of Bessel and Gaussian beams," Opt. Lett., 13, 79-80 (1988).

[34] Bouchal, Z., Wagner, J., Chlup, M., "Self-reconstruction of a distorted nondiffracting beam," Opt. Commun., 151, 207-211 (1998).

[35] Wagner, J., Bouchal, Z., "Experimental realization of self-reconstruction of the 2d aperiodic objects," Opt. Commun., 176, 309-311 (2000).

[36] Bouchal, Z., "Resistance of nondiffracting vortex beam against amplitude and phase perturbations," Opt. Commun., 210, 155-164 (2002).

[37] Garcés-Chávez, V., McGloin, D., Melville, H., Sibbett, W., Dholakia, K., "Simultaneous micromanipulation in multiple planes using a self-reconstructing light beam," Nature, 419, 145-147 (2002).

[38] Čižmár, T., Garcés-Chávez, V., Dholakia, K., Zemánek, P., "Optical conveyor belt for delivery of submicron objects," Appl. Phys. Lett., 86, 174101, (2005).

[39] Badalyan, A., Hovsepyan, R., Mekhitaryan, V., Mantashyan, P., Drampyan, R., "New holographic method for formation of 2D gratings in photorefractive materials by Bessel standing wave," Fundamentals of Laser-Assisted Micro- and Nanotechnologies, Published in Proceedings of SPIE, 7996, 799611, (2010).

[40] Milne, G., Dholakia, K., McGloin, D., Volke-Sepulveda, K., Zemánek, P., "Transverse particle dynamics in a Bessel beam," Optics Express, 15, 13972-13987 (2007).

[41] Garcés-Chávez, V., Summers, M. D., Melville, H., McGloin, D., Wright, E. M., Dholakia, K., "Optical levitation in a Bessel light beam," Appl. Phys. Lett., 85, 4001-4003 (2004).

[42] Lapointe, M.R., "Review of non-diffracting Bessel beam experiments," Opt. Laser Technol., 24, 315-321 (1992).

[43] McDonald, K., *Bessel beams*, (2000).

[44] McQueen, C.A., Arlt, J., and Dholakia, K., "An experiment to study a non-diffracting light beam," Am. J. Phys., 67, 912-915 (1999).

[45] Zapata-Rodríguez, C.J., Sánchez-Losa, A.,"Three-dimensional field distribution in the focal region of low-Fresnel-number axicons," J. Opt. Soc. Am. A, 23, 3016-3026 (2006).

[46] Brzobohatý, O., Čižmár, T., Zemánek, P.,"Quasi-Bessel beam generated by oblate-tip axicon," Proc. of SPIE, 7141, 714126 (2008).

[47] Arlt, J., Garcés-Chavez, V., Sibbett, W., Dholakia, K., "Optical micromanipulation using a Bessel light beam," Opt. Commun., 197, 239-245 (2001).

[48] Arlt, J., Dholakia, K., Soneson, J., Wright, E. M., "Optical dipole traps and atomic waveguides based on Bessel light beams," Phys. Rev. A, 63, 063602/1-063602/8 (2001).

[49] Aiello, A., Agarwal, G., "Self-healing of Gaussian and Bessel beams: a critical comparison," arXiv:1501.05722v1 [physics.optics], 1-23 (2015).

[50] Anderson, C.N., "Numerical Study of Bessel Beam Propagation," Masters Thesis, Optical Science Center, The Graduate College of The University of Arizona, (2005).

[51] Siegman, A.E., *Lasers*, University Science Books (1986).

[52] Schäffer, E., Nørrelykke, S.F., Howard, J., "Surface Forces and Drag Coefficients of Microspheres near a Plane Surface Measured with Optical Tweezers," Langmuir, 23, 3654-3665 (2007).

[53] Gillespie, D.T., Seitaridou, E., *Simple Brownian Diffusion: An Introduction to the Standard Theoretical Models*, Oxford University Press (2012).

[54] Türkcan, S., Alexandrou, A., Masson, J., "A Bayesian Inference Scheme to Extract Diffusivity and Potential Fields from Confined Single-Molecule Trajectories," Biophys. J., 102, 2288-2298 (2012).

[55] Despósito, M., A., Viñales, A.,D., "Subdiffusive behavior in a trapping potential: Mean square displacement and velocity autocorrelation function," Phys. Rev. E, 80, 021111 (2009).

[56] Destainville, N., Salomé, L., "Quantification and correction of systematic errors due to detector time-averaging in single molecule tracking experiments," Biophys. J., 90, L17-L19 (2006).

[57] Al-Shemmeri, T., *Engineering Fluid Mechanics*, Al-Shemmeri & Ventus Publishing ApS (2012).

[58] Adam, M., Delsanti, M.,"Viscosity of semi-dilute polymer solutions," Journal de Physique, 43, 549-557 (1982).

Appendix A: Supplementary Material

A.1 Derivation of Field Irradiance

In this section, we present the mathematical expressions we used to obtain a formula for the total field irradiance $I^{\ell}_{\mathrm{sw}}(r,z)$ of a Bessel beam standing wave. First, we consider the general case of a single Bessel beam, then we address the more specialized case of a Bessel beam standing wave. For a linearly polarized, monochromatic light beam propagating along the positive z-axis, the electric and magnetic field solutions to Maxwell's free space wave equation are

$$\mathbf{E}(\mathbf{r},t) \;=\; \frac{\hat{x}}{2}[E(r,z)e^{i(kz-\omega t)} + \text{c.c.}], \tag{A.1}$$

$$\mathbf{H}(\mathbf{r},t) \;=\; \frac{\hat{y}\varepsilon_0 c_0}{2}[H(r,z)e^{i\left(kz-\omega t\right)} + \text{c.c.}], \tag{A.2}$$

where $\hat{x}$ is the direction of the electric field polarization, $\hat{y}$ is the direction of the magnetic field polarization, k is the wave vector, ω is the angular frequency of the wave, ε_0 is the electric permittivity of free space, c_0 is the speed of light in vacuum, and c.c. stands for complex conjugate. The general expression for the time-averaged irradiance $\langle I\rangle$ of a propagating electromagnetic wave is

$$\langle I\rangle \;=\; \frac{1}{2}\mathrm{Re}(\mathbf{E}(\mathbf{r})\times\mathbf{H}^{*}(\mathbf{r})), \tag{A.3}$$

where the factor of $\frac{1}{2}$ arises from the time-averaging over a single period of the light wave. Substituting the electric and magnetic field solutions from Eqs. (A.1) and (A.2)

into Eq. (A.3), we obtain the following simplified result for the irradiance of the light beam in terms of the electric field:

$$I(r,z) \;=\; \frac{\varepsilon_0 c_0}{2}|\mathbf{E}(r,z)|^2. \tag{A.4}$$

It has been shown [50] that by applying the stationary phase approximation to the Fresnel integral, we get the following general formula for the electric field $\mathbf{E}(r,z)$ of an ℓ^{th}-order Bessel beam wave:

$$\mathbf{E}(r,z) \;=\; \hat{x}E_0\sqrt{\frac{2\pi k_r^2 z}{ik}}e^{-\left(\frac{z}{z_{\max}}\right)^2}e^{\frac{ikr^2}{2z}}e^{\frac{-ik_r^2 z}{2k}}J_\ell(k_r r). \tag{A.5}$$

For an axicon-generated beam, E_0 is the electric field amplitude related to the average irradiance I_{avg} of the beam incident on the axicon, where I_{avg} is given by

$$I_{\text{avg}} \;=\; \frac{1}{2}\varepsilon_0 c_0 E_0^2 \;=\; \frac{P_0}{(\pi\omega_0^2/2)}. \tag{A.6}$$

Here, P_0 is the total power incident on the axicon and ω_0 is the beam radius of the input Gaussian beam measured at the front of the axicon. Equation (A.6) is the defining relationship between the power P_0 and beam waist ω_0 of a Gaussian beam at the front plane of the axicon and the resulting electric field amplitude E_0 of the Bessel beam.

We now consider the case of a Bessel beam standing wave. In our experimental setup (see Fig. 3.1 in Section 3.1), an axicon-generated Bessel beam propagating along the positive z direction passed through a demagnifying telescope and then struck a reflective film normal to its surface, with the film situated at the location of the peak beam irradiance after the telescope, i.e. at $z = z'_{\text{p}}$. The superposition of the incident and reflected beams produced a Bessel beam standing wave above the film,

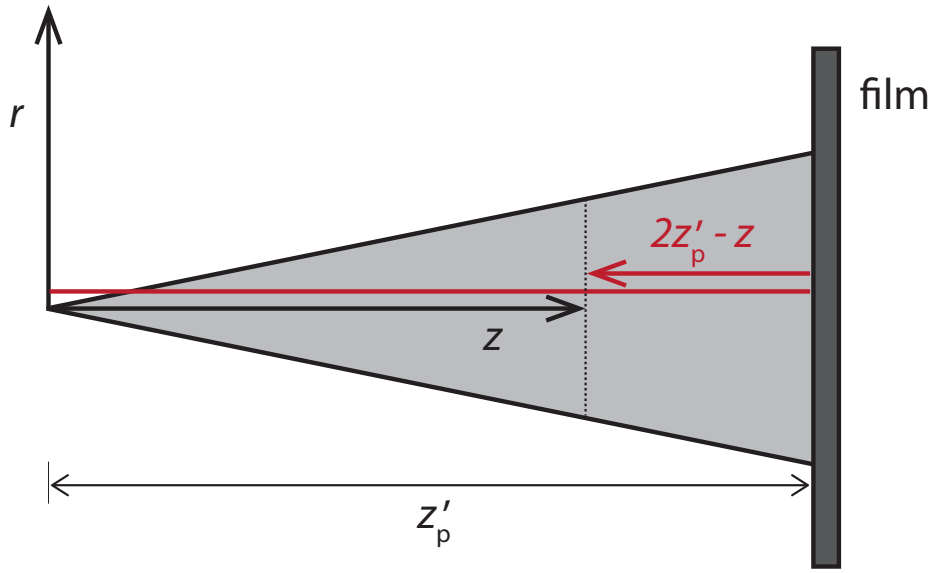

Figure A.1: Coordinate geometry of our axicon-generated Bessel beam standing wave. The incident Bessel beam, defined by electric field amplitude $E(r, z_{\text{inc}})$, originated at the $z = 0$ position and then bounced off of a reflective film placed at the location $z = z'_{\text{p}}$. Therefore, the reflected Bessel beam, defined by electric field amplitude $E(r, z_{\text{ref}})$, started at the $z = z'_{\text{p}}$ location. Together, these counter-propagating beams formed a Bessel beam standing wave above the film. For a given position along the z-axis (dotted line), the z-coordinate (black line) of the incident beam is defined to be $z_{\text{inc}} = z$ and the z-coordinate (red line) of the reflected beam is designated to be $z_{\text{ref}} = 2z'_{\text{p}} - z$. Note: The shaded region in the diagram defines the area where the central spot of the Bessel beam standing wave is considered to be non-diffracting.

incident electric field $\mathbf{E}_{\text{inc}}(\mathbf{r}, t)$ and reflected electric field $\mathbf{E}_{\text{ref}}(\mathbf{r}, t)$. For any position along the z-axis, we can calculate the combined electric field $\mathbf{E}_{\text{sw}}(\mathbf{r}, t) = \mathbf{E}_{\text{inc}}(\mathbf{r}, t) + \mathbf{E}_{\text{ref}}(\mathbf{r}, t)$ using Eq. (A.1) to describe the electric field of each beam and implementing the proper z-coordinate to specify the position of each beam along the z-axis. In Fig. A.1, we provide a graphical representation of the appropriate z-coordinates of each beam for a given location along the propagation axis. Since the incident beam started at $z = 0$ and propagated along the positive z direction, we defined its variable incident position z_{inc} to be $z_{\text{inc}} = z$. Then, because the reflected beam originated at the location $z = z'_{\text{p}}$, we designated its variable reflected position z_{ref} along the propagation axis to be $z_{\text{ref}} = 2z'_{\text{p}} - z$.

Applying our conventions for the z-coordinates, we used Eq. (A.1) to get the following expression for the combined electric field $\mathbf{E}_{\rm sw}(\mathbf{r},t)$ of an $\ell^{\rm th}$-order Bessel beam standing wave:

$$\begin{aligned}\mathbf{E}_{\rm sw}(\mathbf{r},t) &= \frac{\hat{x}}{2}[E(r,z_{\rm inc})e^{i(kz_{\rm inc}-\omega t)}+\text{c.c.}]+\frac{\hat{x}}{2}[E(r,z_{\rm ref})e^{i(kz_{\rm ref}-\omega t)}+\text{c.c.}]\\ &= \frac{\hat{x}}{2}[E(r,z)e^{i(kz-\omega t)}+\text{c.c.}]+\frac{\hat{x}}{2}[E(r,[2z'_{\rm p}-z])e^{i(k[2z'_{\rm p}-z]-\omega t)}+\text{c.c.}],\end{aligned} \tag{A.7}$$

where $E(r,z)$ and $E(r,[2z'_{\rm p}-z])$ are given by Eq. (A.5) to be

$$E(r,z) \;=\; E_0\sqrt{\frac{2\pi z k_r^2}{ik}}e^{-\left(\frac{z}{z_{\rm max}}\right)^2}e^{\frac{ikr^2}{2z}}e^{\frac{-ik_r^2 z}{2k}}J_\ell(k_r r), \tag{A.8}$$

$$E(r,[2z'_{\rm p}-z]) \;=\; E_0\sqrt{\frac{2\pi(2z'_{\rm p}-z)k_r^2}{ik}}e^{-\left(\frac{2z'_{\rm p}-z}{z_{\rm max}}\right)^2}e^{\frac{ikr^2}{2[2z'_{\rm p}-z]}}e^{\frac{-ik_r^2(2z'_{\rm p}-z)}{2k}}J_\ell(k_r r). \tag{A.9}$$

By defining the following terms

$$E_+ \;\equiv\; E(r,z), \tag{A.10}$$

$$E_- \;\equiv\; E(r,[2z'_{\rm p}-z]), \tag{A.11}$$

$$\phi_+ \;\equiv\; kz-\omega t, \tag{A.12}$$

$$\phi_- \;\equiv\; k[2z'_{\rm p}-z]-\omega t, \tag{A.13}$$

we can rewrite Eq. (A.7) as

$$\mathbf{E}_{\rm sw}(\mathbf{r},t) \;=\; \frac{\hat{x}}{2}[E_+e^{i\phi_+}+\text{c.c.}]+\frac{\hat{x}}{2}[E_-e^{i\phi_-}+\text{c.c.}]. \tag{A.14}$$

Finally, substituting Eqs. (A.14) and (A.2) into Eq. (A.3), we get the following expression for the field irradiance $I^{\ell}_{\rm sw}(r,z)$ of an $\ell^{\rm th}$-order Bessel beam standing wave:

$$\begin{aligned} I^{\ell}_{\rm sw}(r,z) &= \frac{\varepsilon_0 c_0}{4}[|E_+|^2+|E_-|^2+E_+E_-^*e^{i(\phi_- -\phi_+)}+\text{c.c.}] \\ &= \frac{\varepsilon_0 c_0}{4}[|E_+|^2+|E_-|^2+E_+E_-^*e^{-i2k(z-z_{\rm p})}+\text{c.c.}]. \end{aligned} \tag{A.15}$$

To obtain an expression for the total field irradiance $I^{\ell}_{\rm sw}(r,z)$ in terms of physical quantities, we evaluate the squared terms in Eq. (A.15) to get

$$|E_+|^2 \;=\; E_0^2\left(\frac{2\pi k_r^2}{k}\right)ze^{-2\left(\frac{z}{z_{\rm max}}\right)^2}J_\ell^2(k_r r), \tag{A.16}$$

$$|E_-|^2 \;=\; E_0^2\left(\frac{2\pi k_r^2}{k}\right)(2z'_{\rm p}-z)e^{-2\left(\frac{2z'_{\rm p}-z}{z_{\rm max}}\right)^2}J_\ell^2(k_r r), \tag{A.17}$$

then we substitute Eqs. (A.8), (A.9), (A.16), and (A.17) into Eq. (A.15). With some additional algebraic simplications, we find

$$\begin{aligned} I^{\ell}_{\rm sw}(r,z) \;=\; &\frac{\varepsilon_0 c_0}{4}E_0^2\left(\frac{2\pi k_r^2}{k}\right)J_\ell^2(k_r r)\Bigg[ze^{-2\left(\frac{z}{z_{\rm max}}\right)^2}+(2z'_{\rm p}-z)e^{-2\left(\frac{2z'_{\rm p}-z}{z_{\rm max}}\right)^2}+ \\ &2\sqrt{z(2z'_{\rm p}-z)}e^{-\left(\frac{z}{z_{\rm max}}\right)^2}e^{-\left(\frac{2z'_{\rm p}-z}{z_{\rm max}}\right)^2}\cos\left(k(z'_{\rm p}-z)\left[\frac{r^2}{z(2z'_{\rm p}-z)}+\frac{k_r^2}{k^2}-2\right]\right)\Bigg]. \end{aligned} \tag{A.18}$$

In Section 2.1, we displayed computer-generated images in MATLAB of the total field irradiance $I^{\ell}_{\rm sw}(r,z)$ given by Eq. (A.18) for order $\ell=0$. We used these plots of the irradiance to illustrate the relative magnitudes of the axial gradient force $\mathbf{F}_{\rm X}$ and the transverse gradient force $\mathbf{F}_{\rm grad}$ in our Bessel beam standing wave trap.

A.2 MATLAB Code: Irradiance Plots

Below is the MATLAB code we used to produce the plots of the field irradiance $I_{\mathrm{sw}}^{\ell}(r, z)$ in Figs. 2.9–2.12.

```
%% Define preliminary values

% Gaussian beam parameters
w0 = 1*10^-3; % radius of beam entering the axicon (meters)
lambda = 1.064*10^-6; % laser wavelength (meters)

% Bessel beam generation and demagnification
gamma = 1*pi/180; % axicon opening angle (radians)
n_ax = 1.508; % index of refraction of axicon material (crown glass)
k_a = 2*pi/lambda; % total wave number of beam in air
k_ra = k_a*(n_ax - 1)*gamma; % lateral wave number in air
M = 10; % angular magnification of telescope
wB_a = 2.405/(k_ra*M); % central maximum after telescope (meters)
zmax = k_a*w0/(k_ra*M^2); % propagation dist. after telescope (meters)
l = 0; % Bessel function order
zp = (sqrt(2*l + 1)/2)*zmax; % peak beam intensity position (meters)
N = 1; % normalization constant (Anderson, 2005)
p = 1; % the order of the Super Gaussian (Anderson, 2005)
P0 = 1;

% Bessel beam in sample
n_w = 1.33; % index of refraction of water
lambda_n = lambda/n_w; % laser wavelength in water (meters)
k = 2*pi/lambda_n; % total wave number of beam in water
k_r = k*(n_ax - 1)*gamma*10; % lateral wave number in sample
wB = 2.405/(k_r*M); % central maximum in sample (meters)

%% Plot of Axial Field Intensity

x = -500:500; % lateral vector values
x = x*(8*10^-6)/500; % x values scaled to match graph dims.
n = 1001; % variable defining vector and matrix dimensions below
A = 5; % desired number of antinodes contained in graph
a = zp - A*lambda/(2*n_w); % starting left position on graph
z_inc = linspace(a,zp,n); % incident beam vector.
z_ref = 2*zp - z_inc; % reflected beam vector.
E = zeros(n,n); % n x n null electric field matrix
```

```
for j = 1:n;
    for m = 1:n; % Eqn (26) in (Anderson, 2005)
    phase_inc = (k*x(j)*x(j)/(2*z_inc(m))) ...
                - (k_r*k_r*z_inc(m)/(2*k))+k*z_inc(m);
    phase_ref = (k*x(j)*x(j)/(2*z_ref(m))) ...
                - (k_r*k_r*z_ref(m)/(2*k))+k*z_ref(m);
    E(j,m) = sqrt(2*pi*z_inc(m)*(k_r*k_r)/(k*N)) ... % incident beam
        *exp(-(z_inc(m)/zmax).^(2*p)) ...
        *complex(cos(phase_inc),sin(phase_inc)) ...
        *besselj(1,k_r*x(j)) ...
        + sqrt(2*pi*z_ref(m)*(k_r*k_r)/(k*N)) ...    % reflected beam
        *exp(-(z_ref(m)/zmax).^(2*p)) ...
        *complex(cos(phase_ref),sin(phase_ref)) ...
        *besselj(1,k_r*x(j));
    end
end

I = E.*conj(E); % irradiance matrix
Imax = max(max(I)); % maximum value of irradiance matrix
normI = I/Imax; % normalized irradiance matrix

figure(1)
imshow(normI, 'InitialMagnification','fit')
axis on
ax = gca;
ax.FontSize = 18;
ax.TickLength = [0.02 0.02];
xlabel('z - z_{p} (\mum)');
set(gca,'XTick',0:500:1000)
set(gca,'XTickLabel',[0 -1])
ylabel('x (\mum)');
set(gca,'YTick',0:250:1000)
set(gca,'YTickLabel',[-8 4 0 -4 -8])

figure(2) % contour plot (to zoom in, adjust range of x)
contourf(normI)
axis on
axis square
ax = gca;
ax.FontSize = 18;
ax.TickLength = [0.02 0.02];
xlabel('z + z_{p}(\mum)');
```

```
set(gca,'XTick',0:500/4:500)
set(gca,'XTickLabel',[0 -3 -2 -1])
ylabel('x (\mum)');
set(gca,'YTick',0:500/4:500)
set(gca,'YTickLabel',[0 -3 -2 -1])

%% Plot of the Transverse Field Intensity

x = -500:500; % horizontal vector values
x = x*(8*10^-6)/500; % x values scaled to match graph dims.
y = -500:500; % vertical vector values
y = y*(8*10^-6)/500; % y values scaled to match graph dims.
n = 1001; % variable defining vector and matrix dimensions below
A = 5; % desired number of antinodes in the graph
z_inc = zp - A*lambda/(2*n_w); % incident beam position
z_ref = 2*zp - z_inc; % reflected beam position
E = zeros(n,n); % n x n null electric field matrix

for j = 1:n;
    for m = 1:n; % Eqn (26) in (Anderson, 2005)
    phase_inc = (k*(x(j)*x(j)+y(m)*y(m))/(2*z_inc)) ...
                - (k_r*k_r*z_inc/(2*k))+k*z_inc;
    phase_ref = (k*(x(j)*x(j)+y(m)*y(m))/(2*z_ref)) ...
                - (k_r*k_r*z_ref/(2*k))+k*z_ref;
    E(j,m) = sqrt(2*pi*z_inc*(k_r*k_r)/(k*N)) ... % incident beam
        *exp(-(z_inc/zmax).^(2*p)) ...
        *complex(cos(phase_inc),sin(phase_inc)) ...
        *besselj(1,k_r*sqrt(x(j)*x(j)+y(m)*y(m))) ...
        + sqrt(2*pi*z_ref*(k_r*k_r)/(k*N)) ...    % reflected beam
        *exp(-(z_ref/zmax).^(2*p)) ...
        *complex(cos(phase_ref),sin(phase_ref)) ...
        *besselj(1,k_r*sqrt(x(j)*x(j)+y(m)*y(m)));
    end
end

I = E.*conj(E); % irradiance matrix
Imax = max(max(I)); % maximum value of irradiance matrix
normI = I/Imax; % normalized irradiance matrix

figure(3)
imshow(normI, 'InitialMagnification','fit')
% contourf(normI)
```

```
axis on
axis square
ax = gca;
ax.FontSize = 18;
ax.TickLength = [0.02 0.02];
xlabel('x (\mum)');
set(gca,'XTick',0:250:1000)
set(gca,'XTickLabel',[8 -4 0 4])
ylabel('y (\mum)');
set(gca,'YTick',0:250:1000)
set(gca,'YTickLabel',[-8 4 0 -4])

figure(4) % contour plot
contourf(normI)
axis on
axis square
ax = gca;
ax.FontSize = 18;
ax.TickLength = [0.02 0.02];
xlabel('x (\mum)');
set(gca,'XTick',0:250:1000)
set(gca,'XTickLabel',[8 -4 0 4])
ylabel('y (\mum)');
set(gca,'YTick',0:250:1000)
set(gca,'YTickLabel',[8 -4 0 4])
```

A.3 MATLAB Code: MSD Graphs

Below is the MATLAB code we used to make the MSD graphs in Figs. 4.14–4.19.

```
%% Calculate and Plot MSD, i.e. rho(tau)
% modified from:
% http://people.brandeis.edu/~gelles/qbve/tscsr/msd.m

D=[data(:,1)*7.4/60,data(:,2)*7.4/60]; % accounts for camera and obj.
tau = 0.0667; % time between trajectory points (sec)
nData = length(data(:,1)); % number of data points
numberOfDeltaT = 100;

sqdisp = zeros(numberOfDeltaT, 1);
```

```
sem = zeros(numberOfDeltaT, 1);
deltat = zeros(numberOfDeltaT, 1);
msdpts = zeros(numberOfDeltaT, 1);
format long

% calculate msd for all deltat
for dt = 1:numberOfDeltaT;
   sqdisp = (D(1+dt:end,1) - D(1:end-dt,1)).^2 + (D(1+dt:end,2)...
   - D(1:end-dt,2)).^2;
   deltat(dt) = dt * tau;
   sem(dt) = std(sqdisp) / sqrt(length(msdpts) / dt);
   msdpts(dt) = mean(sqdisp) - 0.00758;
end

figure(1)
plot(deltat,msdpts,'-ro','MarkerEdgeColor','k','MarkerFaceColor', ...
[.49 1 .63],'MarkerSize',4)
xlabel ('Time  (s)'); ylabel ('MSD')
title('MSD vs Time: 100nm-27um-above')
grid on

%% Fit MSD noise data to 4B^2 (Masson, 2012)

modelFun=@(u,t) 0*t + u(1); % horizontal line
startingVals= 1;
coefEsts=nlinfit (deltat(1:end),msdpts(1:end),modelFun,startingVals);

figure(2)
plot(deltat,msdpts,'-ro','MarkerEdgeColor','k','MarkerFaceColor', ...
[.49 1 .63],'MarkerSize',4)
hold on
u1=coefEsts (1);
noise = u1
xgrid3=linspace (min (deltat),max (deltat), 100);
y3 = 0*xgrid3 + u1; % 4B^2 with fitted parameters

figure(2)
plot (xgrid3,y3)
xlabel ('Time  (s)'); ylabel ('MSD')
title('MSD vs Time: 100nm-27um-above')
grid on
```

```
%% Fit MSD data to Eqn. 1 (Masson, 2012)

modelFun=@(p,t) 4*p(1).*t + p(2); % Eqn. 1
startingVals=  [1  1];
coefEsts=nlinfit (deltat(1:end),msdpts(1:end),modelFun,startingVals);

figure(3)
plot(deltat,msdpts,'-ro','MarkerEdgeColor','k','MarkerFaceColor', ...
[.49 1 .63],'MarkerSize',4)
hold on
p1=coefEsts (1);
p2=coefEsts (2);
D = p1 % Diffusion coefficient
xgrid=linspace (min (deltat),max (deltat), 100);
y= 4*p1.*xgrid + p2; % Eqn. 1 with fitted parameters

plot (xgrid,y)
xlabel ('Time  (s)'); ylabel ('MSD')
title('MSD vs Time: 100nm-27um-above')
grid on

%% Fit MSD data to Eqn. 2 (Masson, 2012)

modelFun=@(q,t) (1/3)*(q(1).^2) .* (1 - exp (-t./q(2))); % Eqn. 2
startingVals= [1  1];
coefEsts=nlinfit (deltat(1:end),msdpts(1:end),modelFun,startingVals);

figure(4)
plot(deltat,msdpts,'-ro','MarkerEdgeColor','k','MarkerFaceColor', ...
[.49 1 .63],'MarkerSize',4)
hold on
q1=coefEsts (1);
q2=coefEsts (2);
Dprime = q1.^2/(12.*q2) % Diffusion coefficient
L = q1
xgrid2=linspace (min (deltat),max (deltat), 100);
y2 = (1/3)*(q1.^2).*(1 - exp (-xgrid./q2)); % Eq. 2 with fitted param

plot (xgrid2,y2)
xlabel ('Time  (s)'); ylabel ('MSD')
title('MSD vs Time: 300nm-8um-above')
grid on
```

A.4 Static Noise Data

Below are tables with the values we measured for the experimental static noise terms $4B^2$ for the 200 and 300 nm diameter particles. For the 100 nm static spheres, we substituted the values we measured for the 200 nm particles.

Table A.1: Static noise values for the 200 nm particle. We used the average value of 0.0076 for both the 100 and 200 nm particles to obtain noise-corrected MSD points.

Trial	$4B^2$ (μm^2)
1	0.0112
2	0.0075
3	0.0040
$\bar{\mathbf{x}}$	**0.0076**

Table A.2: Static noise values for the 300 nm particle. We used the average value of 0.018 to obtain noise-corrected MSD points.

Trial	$4B^2$ (μm^2)
1	0.0160
2	0.0110
3	0.0229
4	0.0134
5	0.0196
6	0.0252
$\bar{\mathbf{x}}$	**0.0180**

Curriculum Vitae :

Contact	Email: cmckell@neovest.com Phone: (801) 375-6850 Address: 1145 South 800 East, Suite 310, Orem, UT 84097 USA
Research	Optical trapping, atomic force microscopy, algorithmic composition
Education	MS, Physics, 2015, Wake Forest University, Winston-Salem, NC BS, Biophysics, 2009, Brigham Young University, Provo, UT
Publications	McKell, C., Conley, H., Busath, D., "AFM Study of Structural Changes in Supported Planar DPPC Bilayers Containing General Anesthetic Isofluorane," BYU ScholarsArchive (2010).
Academic	Adjunct Instructor, UNC School of the Arts, Liberal Arts, Sep–Dec 2012 Teaching Assistant, Wake Forest University, Physics, 2009–2011 Tutorial Lab Assistant, Brigham Young University, Physics, 2008–2009 Research Assistant, Brigham Young University, Philosophy, 2007–2009
Professional	Software Engineer, J.P. Morgan (Neovest, Inc.), Orem, UT, 2014–present Sales Representative, Wireless Advocates, Orem, UT, Feb–Dec 2014
Computer	Java, MATLAB, Mathematica, Maple, LaTeX, ImageJ, Illustrator, Cubase, Ableton Live, FXML
Lab Training	Physics: optical trapping, AFM, SEM, TEM, basic electronics Chemistry: organic synthesis, NMR, calorimetry, titrations Biology: PCR, ELISA, chromatography, SDS gel electrophoresis
Languages	Fluent in English and Spanish. Some knowledge of French and Mandarin.
Awards	Eagle Scout, West Los Angeles County Council, Boy Scouts of America Junior and Senior Honor Scholar, William S. Hart High School
Personal	I am originally from Valencia, CA. In my free time, I like to write music and spend time with my wife, Katherine.